

The realization of atomic resolution with the electron microscope

This article has been downloaded from IOPscience. Please scroll down to see the full text article.

1997 Rep. Prog. Phys. 60 1513

(<http://iopscience.iop.org/0034-4885/60/12/002>)

View [the table of contents for this issue](#), or go to the [journal homepage](#) for more

Download details:

IP Address: 68.3.77.237

The article was downloaded on 24/11/2010 at 03:17

Please note that [terms and conditions apply](#).

The realization of atomic resolution with the electron microscope

David J Smith[†]

Institut für Festkörperforschung, Forschungszentrum Jülich, D-52425 Jülich, Germany

Received 2 June 1997

Dedicated to the memory of the late W Michael Stobbs

Abstract

The high-resolution electron microscope has evolved into a sophisticated instrument that is capable of routinely providing quantitative structural information on the atomic scale. Applications of atomic-resolution imaging can now be found in many scientific fields, and its impact on the knowledge and understanding of atomistic processes has been profound. Better control over instrumental parameters, enhanced reliability of signal recording, and novel methods for imaging and data processing are areas of highly active, ongoing research. Agreement over reliability factors, serious discrepancies in absolute contrast levels, and inversion of crystal scattering are identified as unresolved issues requiring further attention.

[†] On sabbatical leave from: Department of Physics and Astronomy and Center for Solid State Science, Arizona State University, Tempe, AZ 85287-1504, USA.

Contents

	Page
1. Introduction	1515
2. Basic fundamentals	1515
2.1. Image formation and transfer function theory	1515
2.2. Limits and definitions of resolution	1518
2.3. Instrumental parameters	1521
3. Progress towards atomic resolution	1522
3.1. Improvements in instrumentation	1523
3.2. Important milestones	1524
4. Survey of applications	1526
4.1. Semiconductors	1526
4.2. Metals	1529
4.3. Oxides and ceramics	1532
4.4. Surfaces	1538
4.5. Dynamic events	1540
5. Current and future trends	1542
5.1. Image viewing, recording and processing	1542
5.2. On-line microscope control—‘autotuning’	1545
5.3. Third-order aberrations—detection and correction	1548
5.4. Progress towards quantitative structure analysis	1550
5.5. Restoration of the complex exit-surface wavefunction	1553
5.6. Chemical imaging	1558
5.7. Incoherent STEM imaging	1560
5.8. Structural information beyond the conventional resolution limits	1562
6. Problems	1568
6.1. Noise	1568
6.2. Radiation damage	1569
6.3. Inversion of crystal scattering	1570
7. Concluding remarks	1571
Acknowledgments	1571
References	1572

1. Introduction

The era of atomic resolution with the electron microscope has well and truly arrived. Steady improvements in design and careful attention to environmental factors have brought about a substantial realization of the potential offered by the sub-angstrom wavelength of the energetic electron beam. Many instruments worldwide can now routinely provide images that are directly interpretable in terms of atomic structure. The successes of many recent structural studies have established that the high-resolution electron microscope (HREM) has a valuable role to play in determining atomic configurations in complex materials, especially at structural irregularities or defects, thereby providing information on a local scale that is inaccessible to bulk diffraction methods. Moreover, improvements in quantification from evolving processing and recording schemes are likely to be forthcoming. Further large gains in resolution cannot be expected because of the inescapable spherical aberration of the objective lens which represents a fundamental limit on attainable resolution. However, there continues to be hope for an imminent breakthrough leading to its correction (Rose 1994, Haider and Zach 1995).

The HREM has had a major impact in many scientific areas which include the fields of mineralogy, solid-state chemistry and physics, and materials science. Direct chemical identification of specific atomic columns is not usually available but, given prior information about bulk crystal structures and some knowledge of structural principles, the (re-)arrangements associated with ordered intergrowths and novel phases can often be deduced directly. On the other hand, isolated structural defects such as interfaces and dislocations, are intrinsically more difficult to characterize because such a priori details are generally unavailable. During the process of structure refinement, the electron microscopist is likely to resort to comparisons, sometimes lengthy and time consuming, between experimental micrographs and computer-simulated images based upon structural models.

The purpose of this review article is to describe the attainment of atomic resolution with the electron microscope, to summarize some of its accomplishments and to forecast some likely future trends. The basic principles of image formation are first briefly introduced in section 2 to provide a rationale for the various definitions of resolution that are in common usage. Key developments in instrumentation and important milestones are then summarized in section 3. In section 4, examples of atomic-resolution imaging are very briefly discussed, primarily to underline the breadth of the fields being impacted by the technique. Active areas of ongoing research and development are briefly described in section 5. In particular, progress towards quantitative structure refinement is reviewed and the retrieval of information beyond the conventional resolution limits is also considered. Finally, some problem areas are briefly identified in section 6.

2. Basic fundamentals

2.1. Image formation and transfer function theory

Image formation in the electron microscope consists of two consecutive processes. First, elastic (and inelastic) scattering of electrons occurs as the electron beam traverses through

the specimen, resulting in the formation of the exit-surface wavefunction, or what is often called the exit-surface image (ESI). This wavefunction is then propagated through the imaging lenses of the microscope and eventually forms an image on the final viewing screen or recording medium, such as the photographic negative or the slow-scan charge-coupled-device (CCD) camera. The role of the inelastically scattered electrons in image formation will, to a large extent, be ignored in this review, primarily because high-resolution imaging is restricted to thin specimen regions where their effect is usually regarded as marginal. However, in addition to smearing out higher resolution detail in thicker regions, the inelastically scattered electrons cause overall image contrast to be reduced. As a means to circumvent these problems, and also to assist quantitative image comparisons, it was proposed that the possibility for energy-filtered imaging should be explored on future HREMs (Stobbs and Saxton 1988). The very recent development of a post-column imaging filter allows these options to be investigated (Gubbens and Krivanek 1993).

A major problem in high-resolution electron microscopy, one that is not shared with traditional diffraction techniques, is that the electrons which are scattered by the specimen can suffer further phase reversals which are primarily dependent upon the defocus, Δf , and the spherical aberration coefficient, C_S of the objective lens. These phase changes, which are angle dependent, are given by $\exp[i\chi(u)]$, where

$$\chi(u) = \pi \Delta f \lambda u^2 + \pi C_S \lambda^3 u^4 / 2 \quad (1)$$

where λ is the electron wavelength and u is the two-dimensional reciprocal space coordinate with magnitude given by $|u| = (2 \sin \theta / \lambda)$. The presence of these phase changes must be understood, and properly accounted for, in order to avoid erroneous interpretation of high-resolution (phase-contrast) images. Moreover, it should be further appreciated that it may still not be straightforward to invert the imaging process and retrieve the projected microstructure of the specimen because of the occurrence of inelastic scattering and multiple elastic scattering within the sample. Problems associated with the inversion of crystal scattering are discussed in section 6.3.

A convenient and helpful way to visualize the phase modulations caused by the objective lens is to utilize the transfer function (TF) theory (Hanszen 1971). Under the assumptions that the specimen is an ideal weak phase object, and that the incident electron beam is fully coherent, then the effect of the objective lens can be represented by the phase contrast transfer function (PCTF), given by

$$\begin{aligned} T(k) &= 2 \sin \chi(k) \\ &= 2 \sin \pi k^2 (k^2/2 - D) \end{aligned} \quad (2)$$

where the defocus D (which equals $\Delta f / (C_S \lambda)^{1/2}$) and spatial frequency k (which equals $|u| \lambda (C_S \lambda^3)^{1/4}$) are expressed for convenience in generalized units. A single set of universal curves can then be used to summarize the transfer behaviour of all objective lenses, irrespective of voltage, microscope and specimen.

As an example, figure 1 shows three TF curves for the values: (a) $D = 1$, commonly known as the Scherzer focus (Scherzer 1949); (b) $D = 1.5^{1/2}$, sometimes called extended Scherzer; and (c) $D = 3.5^{1/2}$, which could be called the extended second broadband because of the broad band of constant phase present at higher spatial frequencies. Of particular note in these figures are the phase oscillations at higher spatial frequencies, which cause uninterpretable artefacts for any corresponding higher-resolution detail present in the image, and the reversal in phase of (c) relative to (a) and (b) over a broad range of spatial frequency, which could result in reversals in contrast to major image features. The importance of

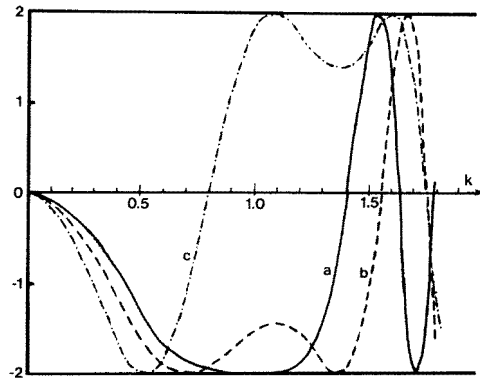


Figure 1. Universal curves independent of electron microscope, objective lens and accelerating voltage which show the behaviour of the generalized lens transfer function versus the scattering angle at several defocus values: (a) $D = 1$; (b) $D = 1.5^{1/2}$; (c) $D = 3.5^{1/2}$.

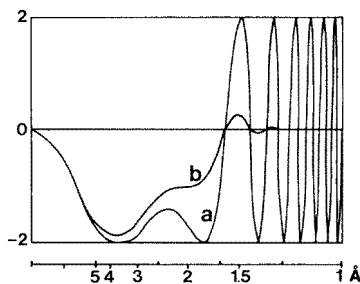


Figure 2. Comparison of TF curves for a 400 keV HREM, axial illumination, $C_s = 1.0$ mm. (a) coherent illumination, no damping functions; (b) effect of damping functions for a focal spread of 8 nm and an incident illumination semi-angle of 0.5 mrad.

establishing calibrations for the objective lens focus, and the defocus steps, cannot be over emphasized (Smith 1989a), and will be discussed in more detail in the following section.

The coherence of the incident electron beam will be affected in practice by focal spread (temporal coherence) and finite beam divergence (spatial coherence): this loss of coherence is usually described in terms of envelope functions (Frank 1973a). As illustrated by the example in figure 2, which is for a 400 keV HREM equipped with a lanthanum hexaboride electron source, these functions combine to dampen out the higher spatial frequencies of the ideal PCTF: higher resolution detail is therefore normally absent from the final image. However, imaging with a field emission gun, which has high electron-optical brightness and lower intrinsic electron energy spread, offers the prospect of greatly reduced damping (Humphreys and Spence 1978). When the imaging conditions are well known, retrieval of the higher spatial frequency detail becomes possible (Otten and Coene 1993). Overall, it can be concluded that the effects of the PCTF on image formation are well understood, even for partially coherent illumination, and they can thus be easily incorporated into computer simulations although care is still needed during image interpretation.

Electron scattering, unlike x-ray or neutron scattering, is a heavily dynamical process which involves large phase changes and multiple scattering events in addition to inelastic scattering. The height distribution of atoms within the sample becomes important and the intuitive interpretation of image contrast features in terms of projected structure becomes

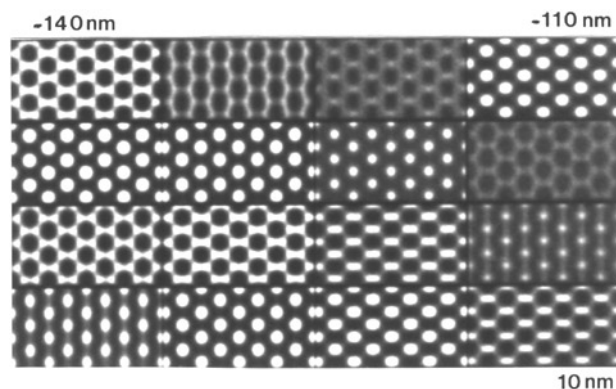


Figure 3. Through-focal series of image simulations for crystal of tin dioxide in [100] projection: 500 kV, $C_S = 3.5$ mm, crystal thickness = 2.8 nm. Focus extends in 10 nm steps from -140 nm (top left) to $+10$ nm (bottom right) (from Smith *et al* 1983a).

rapidly more unreliable as the sample thickness is increased. Image simulations become essential for quantitative interpretation. Several methods exist. The most widespread is based upon the multislice algorithm (Cowley and Moodie 1957a, Goodman and Moodie 1974), and well documented, user-friendly packages are nowadays readily available (O'Keefe 1984, Stadelmann 1987, Self and O'Keefe 1988). As an example, figure 3 shows a through-focal series of simulated images for a thin crystal of [100] tin dioxide (Smith *et al* 1983a). Note the recurrence of similar image appearance as the focus is changed, and contrast reversals also occur for prominent image features. This multiple occurrence of very similar images, which are known as Fourier- or self-images (Cowley and Moodie 1957b, Iijima and O'Keefe 1979), for small-unit-cell materials, exacerbates the difficulty of selecting the optimum defocus for direct image interpretation in these materials.

In practice, computer image simulations fulfil several useful purposes. Initially, a through-thickness, through-focal (TTTF) tableau of simulated images provides a convenient starting point for the likely image appearance, as well as acting as a practical guide to imaging conditions (Hetherington *et al* 1990). More importantly, as shown later, computer simulations can be used during the refinement process as a means of testing and/or confirming proposed structural models. Finally, detailed comparisons of intensity and appearance between experimental micrographs and simulated images are nowadays considered as obligatory before a defect structural model can be regarded as acceptable (Penisson *et al* 1988, Hoche *et al* 1993, Smith *et al* 1993).

2.2. Limits and definitions of resolution

In the broadest sense, the resolution of a microscope is simply defined in terms of its ability to discriminate between two discrete objects. Using the Rayleigh criterion for overlapping Airy diffraction disks in the absence of lens aberrations, the minimum separation of two self-luminous point sources is given by the expression

$$d_{\text{DIFF}} = \lambda/2 \sin \alpha \quad (3)$$

where α is the half-angle subtended at the object (Sarikaya 1992). Thus, the resolution could be improved by simply increasing the aperture angle. In practice, electron lenses have unavoidable spherical aberration (Scherzer 1936). Since the disk of least confusion

Table 1. Interpretable resolution as a function of electron energy and C_s value.

Energy (keV)	λ (Å)	C_s (mm)	δ (Å)
100	0.0370	0.7	3.0
200	0.0251	0.8	2.2
300	0.197	0.9	1.8
400	0.164	1.0	1.7
600	0.126	1.5	1.55
1000	0.0087	1.7	1.17
2000	0.0050	4.0	0.99

due to spherical aberration increases with the third power of the aperture half-angle, namely:

$$d_s = kC_s\alpha^3 \quad (4)$$

where k is a constant, then it is necessary to make a compromise between the limits for diffraction and spherical aberration. Depending upon certain assumptions about the imaging conditions, such as whether the incident electron illumination is coherent or incoherent, these two expressions may be combined in slightly different ways. The end result is, however, similar. The ultimate resolution of the electron microscope will always be given by an expression of the form

$$d = AC_s^{1/4}\lambda^{3/4} \quad (5)$$

where A is a constant (either 0.43 or 0.56). Thus, instead of the sub-angstrom resolution implied by (3), typical resolution figures with realistic C_s values (which scale from about 0.3 mm at 100 keV to about 1.5 mm at 1.0 MeV due to saturation of the magnetic pole-piece material) are in the range of 0.25–0.12 nm.

This simple-minded approach ignores the effect of chromatic aberration as defined by the equation

$$d_c = C_c\alpha[\Delta E/E + 2\Delta I/I] \quad (6)$$

where C_c is the chromatic aberration coefficient of the objective lens, ΔE is the energy spread of the electron beam of energy E , and ΔI is the instability of the objective lens current I . This omission is nowadays justified for TEMs operating at energies of 100 keV or more, due to the high stability of the lens-current (<1 part per million (ppm)) and high-voltage (<2 ppm) power supplies.

Contemporary treatments define TEM resolution in terms of TF theory for weak phase objects (see, for example, Cowley 1981, O'Keefe 1992). The *interpretable* resolution, often known as the *structural* or *point* resolution, is directly related to the first zero crossover of the TF at the defocus giving the widest possible band of spatial frequencies without phase reversals. This situation closely corresponds to curve B in figure 1, and the corresponding resolution limit is given by

$$\delta \sim 0.66(C_s\lambda^3)^{1/4}. \quad (7)$$

Table 1 compares typical values of δ at different accelerating voltages. This resolution represents the upper limit to which intuitive image interpretation can be made directly in terms of the projected crystal structure, with the additional stipulation that the specimen must still be thin (i.e. no multiple scattering). Information may still be transferred by the objective lens at higher spatial frequencies but it will be uninterpretable because of the phase changes induced by the TF oscillations. Overall, it can be concluded from table 1 that the

inevitable increases in C_s due to magnetic saturation as the electron energy is increased, are far outweighed by the decrease in the electron wavelength.

The *instrumental* resolution, sometimes called the information limit, is defined in terms of the damping of higher spatial frequency information caused by the temporal and spatial coherence functions. The value of $\exp\{-2\}$ is taken as the cut-off since it is usually considered to be the minimum level of signal that can be retrieved by *a posteriori* image processing (O'Keefe 1992). In many 100 keV or 200 keV HREMs, this instrumental resolution limit can extend substantially beyond the interpretable resolution limit, especially at large underfocus values with defocused illumination (i.e. better spatial coherence). However, image processing is then usually required in order to interpret the finest detail in terms of specimen features. Recently, transmission electron microscopes have become available commercially that are equipped with reliable field emission gun (FEG) electron sources that provide highly coherent illumination (Murakoshi *et al* 1992, Otten and Coene 1993, Honda *et al* 1994). With these instruments, the operator is normally obliged to use a suitably sized objective aperture to prevent the higher-order beams from contributing to the image since it is otherwise covered with very fine uninterpretable detail. Alternatively, provided that the defocus and C_s values are well known, the effect of the TF can be deconvoluted to extend the resolution limit to which the image detail becomes interpretable (Humphreys and Spence 1978, Coene *et al* 1992). Finally, note that, unlike the interpretable resolution which is easily calculated, the instrumental resolution can only be determined experimentally, usually by reference to a power spectrum (Fourier transform) from the image of a thin amorphous material.

The *lattice-fringe* resolution corresponds to the finest spacing visible in the lattice-fringe images that occur as a result of interference between two or more diffracted beams originating from a crystalline material. These images are often recorded with tilted illumination to ensure freedom from chromatic effects. The fineness of the fringes is a direct reflection of the instrumental stability of the HREM, and its freedom from external influences such as acoustic noise, mechanical vibrations and stray magnetic fields. However, the fringes do not usually provide useful information about local atomic positions since the interfering diffracted beams typically originate from comparatively large specimen areas. Figure 4 shows lattice fringes with spacings of 0.62 Å and 0.72 Å from a thin Ni crystal. The image was recorded at 100 kV with a TEM having a structural resolution of approximately 0.30 nm (Matsuta *et al* 1978). For many years, the lattice-fringe resolution was widely regarded as the ultimate figure of merit for an HREM, although it should now be apparent that the interpretable and instrumental resolution limits represent far more useful benchmarks for comparison purposes.

In the most general framework, the ultimate resolution attained in the electron microscope not only depends on the overall stability and transfer characteristics of the instrument, but it must also be related to the object structure and to the final recording medium (van Dyck and de Jong 1992). Theories for electron scattering have been proposed (see, for example, Cowley 1981) and various image simulation programs have been successfully implemented (see, for example, Self *et al* 1983, van Dyck 1980), but significant discrepancies still exist between the absolute contrast of experimental and calculated images even for comparatively simple model systems (Hýtch and Stobbs 1994, Walther *et al* 1995). These problems will be discussed further in section 5.4. Moreover, a full description of resolution is incomplete without careful consideration of the overall signal-to-noise ratio of the entire system taking into account the characteristics of the source, scattering from the sample and the recording system. A detailed discussion of these issues can be found in de Jong and van Dyck (1993).

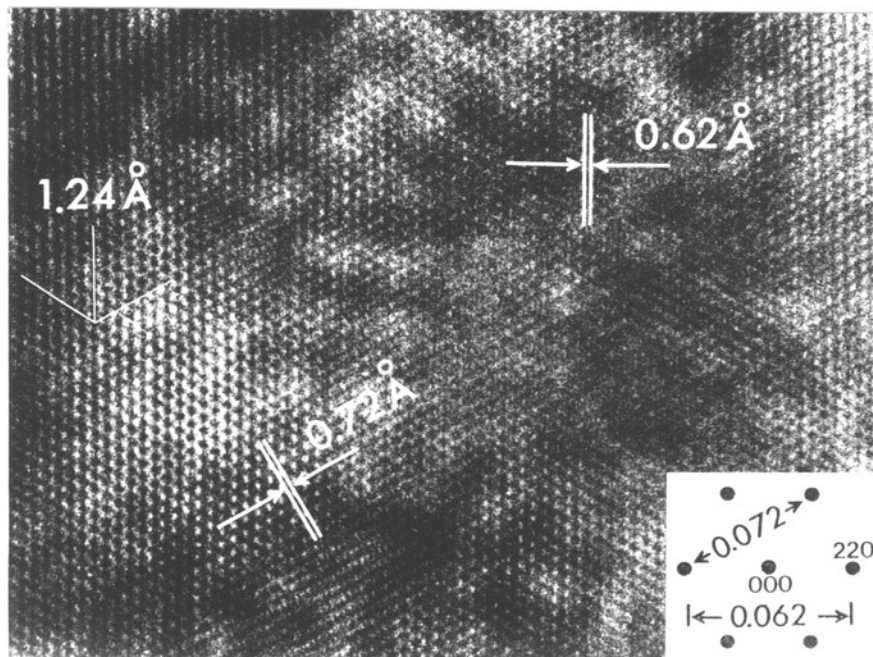


Figure 4. Lattice-fringe image from thin Ni foil displaying spacings of 0.62 Å, 0.72 Å and 1.24 Å due to mutual interference of various diffracted beams (from Matsuta *et al* 1978).

2.3. Instrumental parameters

Similar to any complicated piece of equipment, the high-resolution electron microscope has many adjustable operating parameters. In terms of obtaining maximal performance, only a subset of these needs to be known or controlled with any degree of accuracy. For example, crystalline materials usually have known lattice dimensions that provide an internal calibration of the image magnification. The camera length for a particular diffraction pattern may be important for analysing an unknown material but it is largely irrelevant for quantitative imaging purposes. The accelerating voltage obviously determines the electron energy and hence its wavelength. For atomic-resolution imaging, it is essential that the voltage is fixed and highly stable, preferably to within 1 ppm, but the exact value is relatively unimportant. The setting of the objective lens current will determine its focal length and several other imaging parameters, including C_s , the spherical aberration coefficient and C_c , the chromatic aberration coefficient. In practice, it is most important to operate at a fixed objective lens current, since several adjustable parameters such as beam tilt and image astigmatism depend sensitively on the value of the current. It is therefore customary for reference purposes to provide a lens current monitor with at least three-figure accuracy. In order to restore image focus, when the sample is tilted or another field of view is selected, the sample height is adjusted when possible rather than changing the objective lens current setting. Experimental determination of these instrumental parameters is well documented elsewhere (e.g. Smith 1989a) so these details will not be reproduced here.

Given the extraordinary sensitivity of the image appearance to the objective lens setting, as caused by the oscillations of the TF (see figures 1 and 2), knowledge of the objective lens *defocus* is critical to image interpretation. Consider the case for small-unit-cell materials

such as metals and semiconductors. The Fourier or 'self'-images of the crystal lattice (spacing d) recur periodically with a period given by $2d^2/\lambda$ (Cowley and Moodie 1957b, Iijima and O'Keefe 1979). For a lattice spacing of 0.20 nm at 400 keV, a complete reversal of the image contrast thus occurs with a defocus change of about 24 nm. In some cases, the very characteristic image pattern of more complicated structures at the optimum defocus can be recognized. In the more general case of an aperiodic unknown feature such as a dislocation or grain boundary, the operator must establish some other means for choosing defocus, even though the defocus step size may already have been calibrated, either by the microscope manufacturer or by the microscopist. One method of increasingly common usage is to generate the TTF tableau of images of the perfect crystal structure before commencing microscopy. For fine image detail, even this method may still be insensitive. Some microscopists resort to recording a focal series of images with precalibrated focal step size, thus reducing the subjective element of the matching process (Wilson *et al* 1982). Methods based on cross correlation (Thust and Urban 1992) and nonlinear least squares (King and Campbell 1993, 1994) have been developed for matching experimental and simulated images: these appear to provide a reliable determination of both defocus *and* specimen thickness on a local scale. These values can then be used in the subsequent evaluation of any closely neighbouring crystal defect.

In pushing to the extreme limits of resolution, several aberrations associated with the objective lens begin to play an increasingly influential role in determining the overall integrity of the final image. The well known two-fold astigmatism results in focal length differences in orthogonal image directions, with a corresponding effect on the image appearance. Its presence is usually detected by reference to the image of a thin amorphous film of carbon or germanium: Fourier transformation of the recorded intensity distribution reveals a set of concentric rings, reflecting the TF prevailing at the time of recording the image. These rings are more or less elliptical depending on the amount of astigmatism present (Krivanek 1976). A comparison of diffractograms for astigmatic and stigmated images is shown in figure 5. This type of astigmatism can be substantially, though not entirely, corrected using two sets of subsidiary quadrupole coils located below the lower pole-piece of the objective lens. The third-order aberrations of coma and three-fold astigmatism are more difficult to detect and quantify because their influence is only visible in images of amorphous materials recorded with tilted incident illumination (Zemlin *et al* 1978, Krivanek 1994). Strategies for minimizing their deleterious effects are discussed in section 5.3.

Finally, successful implementation of image reconstruction schemes involving either focal series (Coene *et al* 1992) or off-line electron holography (Orchowski *et al* 1995) necessitates that the spherical aberration coefficient should be determined within an error of no more than 1%. The traditional graphical method of optical diffractogram analysis (Krivanek 1976) is no longer sufficiently accurate, and it is necessary to resort to alternative methods to attain the desired accuracy. Statistical methods based, for example, on diffractograms from a through-focal series have been reported to enable standard deviations at the 1% level (Glanvill *et al* 1985, Coene and Denteneer 1991).

3. Progress towards atomic resolution

The atomic-resolution capability of the electron microscope, which was predicted by its inventor in the early 1930s (Ruska 1980), took several decades to be realized. Meanwhile, progressive improvements in instrumentation invariably opened up new areas for fruitful study. Some of the developments are identified in the following sections. As the resolution

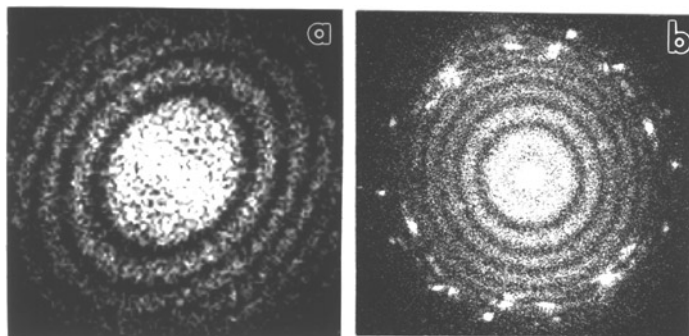


Figure 5. Diffraction patterns obtained by a Fourier transformation of electron micrographs provide information about prevailing imaging conditions. (a) Sample of amorphous carbon, the elliptical shape is due to an astigmatic image; (b) sample of amorphous carbon, decorated with small gold particles. Diffraction spots due to Au lattice fringes in the original image provide internal calibration of reciprocal length scale.

limits slowly improved, the requirements for beam and crystal tilt as well as focusing became more exacting. Better methods were required for determining the experimental parameters with higher precision.

3.1. Improvements in instrumentation

The reliability, complexity and resolving power of the electron microscope have steadily improved as technological developments have been progressively incorporated (Herrmann 1978, 1983). The first electron microscope to exceed the resolving power of the best available optical microscope was rather rudimentary in design. A single condenser lens focused the electron beam onto the sample, the imaging system consisted of only two lenses with a maximum magnification of $12\,000\times$, and the final image was usually obtained by photographing the fluorescent screen from outside the microscope vacuum. The addition of a second condenser lens enabled the focused spot size and the angle of illumination of the incident beam to be controlled independently, and some modern microscopes even incorporate a third lens for additional flexibility and fine probe studies. As the resolution improved, additional magnifying lenses were required in order for the finer image detail to be adequately resolved on the viewing and recording media: four imaging lenses in addition to the objective lens are nowadays typical, with magnifications of up to $2\,000\,000\times$ becoming possible. Much stronger excitations of the objective lens provide significant reductions in the spherical and chromatic aberration coefficients but the sample must be immersed within the magnetic field of the objective lens and the pole-piece material invariably becomes partially saturated making the calculation of the optical properties more difficult. Lanthanum hexaboride replaced tungsten as the material of choice for the electron source: its enhanced electron-optical brightness permits smaller incidence angles (better spatial coherence), and useful emitting lifetimes are at least an order of magnitude longer than those of tungsten (perhaps 1000 h or more). For many years, the FEG electron source was only found attached to scanning and scanning transmission electron microscopes (STEMs) but several microscope manufacturers have modified the design of their instruments, so that FEGs are nowadays offered as an option to the potential TEM buyer. They provide almost indefinite lifetimes (failure is most often due to operator error), lower intrinsic energy spread (0.25 eV compared with about 0.8 eV for LaB_6) and vastly superior electron-optical brightness (at

least two orders of magnitude greater than that of LaB_6). Because of the enhanced beam coherence, the FEG-TEM should have an instrumental resolution considerably in excess of its interpretable resolution: for example, an improvement of 0.24–0.15 nm has been demonstrated for a 200 keV instrument that uses a thermal-field-assisted FEG source (Otten and Coene 1993).

In order to achieve atomic resolution, other aspects of instrumentation must also be addressed. For example, high-voltage and lens-current instabilities should be about 1 ppm or less. The sample holder must permit accurate positioning of the specimen (to within several nanometres) and control of its orientation (to $\sim 10^{-3}$ rad or better), and yet the holder should be free of any significant drift during photographic exposures ($\sim 0.01 \text{ nm s}^{-1}$ or less). The microscope should be isolated from sources of acoustic noise, mechanical vibration and stray magnetic fields. Manufacturers will usually survey the prospective site(s) proposed by their customers to ensure that these environmental requirements are met, while some serious users even provide their own vibration isolation system. In our experience (Smith *et al* 1982), it is useful to have access to facilities for monitoring the more critical parameters, such as vibration levels, stray magnetic fields and high voltage stability: the causes of any sudden drop-off in performance can often be quickly determined. It can also be helpful for comparison purposes, when loss of resolution is suspected, to retain a test specimen of known appearance, such as small gold particles supported on a thin amorphous film.

3.2. Important milestones

Although the performance of the ‘high’ resolution electron microscope first exceeded that of the optical microscope in the mid 1930s (Ruska 1934), identifying in turn and then overcoming the various limitations on resolution proved to be a slow process. Major obstacles included poor mechanical and thermal stability, the electrical stability of the high voltage and lens current supplies, and the residual astigmatism of the objective lens. The observation of Fresnel fringes around small holes in carbon support films provided a sensitive, and highly practical, criterion for astigmatism correction (Haine and Mulvey 1954).

Phthalocyanine crystals provided the first example of lattice-fringe imaging on the nanometre scale (Menter 1956) and smaller sub-nanometre lattice spacings were subsequently achieved using tilted illumination to eliminate the effects of chromatic aberration (Dowell 1963). Crossed fringes from thin metal foils were observed by tilting the incident beam so that the directions of the transmitted beam and the several diffracted beams were all aligned at the same angle with respect to the optic axis (Komoda 1966a, Fukuhara *et al* 1966/1967). Careful theoretical analysis of the imaging conditions showed, however, that the positions of the intensity maxima were shifted sideways due to the effects of spherical aberrations and defocusing, with the important end-result that the intensity distribution in the lattice image could not be literally interpreted as a representation of the actual atomic column positions (Komoda 1966b).

Direct correspondence between lattice images and projected crystal structure was first achieved in observations of large-unit-cell block oxides using axial illumination (Allpress and Sanders 1969). The positions of individual atomic columns could be identified in later studies of similar block oxides (Iijima 1971, Hutchison and Anderson 1972) since the structure of these materials was well established from x-ray diffraction. The validity of image interpretation was also confirmed by image simulations (Allpress *et al* 1972), thus giving confidence to studies of related materials, especially those with structural defects.

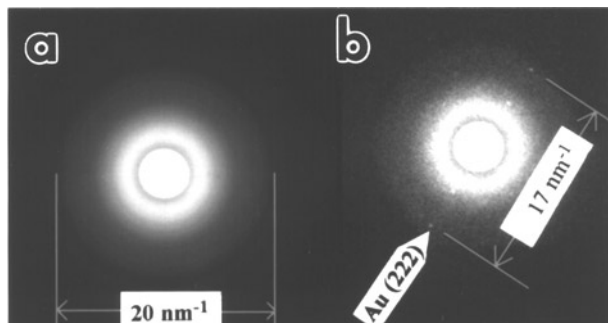


Figure 6. Diffractograms taken from images of thin amorphous films of germanium coated with small gold particles, obtained with the ARM-1250 HREM installed in Stuttgart. (a) Rotationally averaged; information transfer clearly extends beyond the 0.105 nm interpretable resolution limit; (b) {222} spots (spacing of 0.117 nm) visible within the pass-band (from Phillipp 1996).

It is only comparatively recently that instrumentation has improved to the extent that directly interpretable information about atomic arrangements could be recorded for metals, ceramics and semiconductors aligned in low-index zone-axis projections. For example, images of twin boundaries in germanium were obtained with a modified 500 keV HREM (Krivanek *et al* 1977), and individual atomic columns were resolved in a small gold particle (Cosslett *et al* 1979). Several high-voltage HREMs, designed specifically to take advantage of the predicted resolution improvement at shorter wavelength, first surpassed the 0.2 nm interpretable resolution limit on a routine basis in the early 1980s (Hirabayashi *et al* 1982, Smith *et al* 1982, Yagi *et al* 1983, Gronsky and Thomas 1983). Intermediate voltage TEMs soon became available commercially that could also attain this performance level regularly (Smith *et al* 1985a, Hutchison *et al* 1986, Bourret and Penisson 1987).

Further improvements have recently been reported. The highly coherent illumination available with 300 kV FEG TEMs has facilitated the achievement of instrumental resolutions approaching 0.1 nm (van Dyck *et al* 1997), with image interpretation to the same level being achieved either by through-focal series reconstruction (Coene *et al* 1993) or off-axis electron holography (Lichte *et al* 1993). The latest generation of high-voltage (1–1.5 MV) HREMs have even succeeded in closely approaching the long-sought-after goal of 0.1 nm without reversals in the contrast transfer function (Horiuchi *et al* 1991, Ichinose 1994, Phillipp *et al* 1994), thereby enabling direct image interpretation at the same level and, in principle at least, eliminating the necessity for any a posteriori image processing. Figure 6 shows the diffractogram from an image of amorphous germanium recorded at 1250 keV with the so-called atomic-resolution microscope (ARM-1250) in Stuttgart (Phillipp 1996): significant information transfer to the first zero crossover of 0.105 nm is clearly demonstrated.

The achievements of the high-resolution STEM, as developed by Crewe *et al* (1968), warrant special mention. The STEM utilizes an FEG to provide a finely focused spot of electrons which is scanned across the specimen synchronously with the modulated line scan of a display monitor. Its resolving power is closely related to the minimum size of the focused probe: as indicated by recent images from {110}-oriented Si crystals, a resolution of better than 0.136 nm has been achieved by a 300 kV instrument (von Harrach 1995). Isolated, individual atoms on thin support films were first resolved using STEM (Crewe *et al* 1970): later studies included quantitative measurements of atomic diffusion (Isaacson *et al* 1976). Further developments and applications of incoherent STEM imaging are considered in more detail in section 5.7.

4. Survey of applications

Electron microscopes intrinsically capable of atomic resolution are commonplace. Applications to diverse materials are nowadays reported at many conferences, and research articles featuring atomic-resolution images of structural defects appear regularly in scientific journals. To provide a complete and up-to-date review of atomic-resolution imaging is therefore an impossible task. The purpose of this section is instead to highlight some representative examples, particularly structural studies where image simulations and/or atomic modelling have also been involved. The primary motivation for many of these studies has been to understand the effect that structural discontinuities might have on chemical and physical processes such as crystal growth, epitaxy, catalysis and phase transformations. In addition to the proceedings of any recent international microscopy conference, the interested reader is referred to several review articles (Cowley and Smith 1987, Smith 1989b), conference proceedings (Krakow *et al* 1989, Sinclair *et al* 1990, Biegelsen *et al* 1993, Smith and Spence 1993, Rühle *et al* 1994, Sarikaya *et al* 1995) and research monographs (Spence 1988, Horiuchi 1994) for further sources of references.

With the improvement of interpretable and instrumental resolutions to 0.20 nm and beyond, individual atomic columns can be directly visualized in an increasing number of crystallographic projections (Bourret *et al* 1983). However, before the atomic-resolution performance of the electron microscope can be fully utilized in materials studies, several additional requirements must be satisfied by the specimen. Since the recorded image represents a two-dimensional projection of the crystal structure, image interpretation in terms of atomic locations will only be possible when the incident electron beam is closely aligned with a major zone axis of the crystal. The tolerances for crystal alignment to avoid overlap of projected atomic columns become more exacting for thicker crystals and finer column separations (Smith *et al* 1983b). The examination of crystalline defects must be primarily confined to linear defects, such as dislocations, and planar faults, such as twin boundaries, crystallographic shear defects and stacking faults, that are aligned with the electron beam direction and assumed to be periodic through the entire projected structure. Inclined faults and curved grain boundaries will not in general be amenable to fruitful study by atomic-resolution imaging. Finally, the sample must be sufficiently thin, typically of the order of 15 nm or less, so that multiple electron scattering does not become significant. Otherwise, the very fine features that are visible in the image may no longer be interpretable in terms of atomic arrangements, even with the assistance of image simulations.

4.1. Semiconductors

The characterization of semiconductor defects, especially interfaces, has undoubtedly been an area of great activity and much success for electron microscopy studies over the past 25 years. Because of the relatively large size of the unit cells of elemental and compound semiconductors, ranging from 0.35 nm (Si) to 0.65 nm (CdTe), high-resolution lattice-fringe images are comparatively easy to obtain in the $\langle 110 \rangle$ orientation (Smith and Lu 1991). Identification of the crystal polarity for compound semiconductors can usually be achieved in this projection by close scrutiny of the image appearance over a range of thickness and defocus values (Glaisher *et al* 1989a, Smith *et al* 1989a). However, individual atomic columns are not separately resolved in this projection unless the microscope resolution is sufficient to allow the 004-type reflections to contribute to the imaging process (Krivanek and Rez 1980, Glaisher *et al* 1989b, Orchowski *et al* 1995). True atomic imaging for elemental Si and Ge has been demonstrated as being possible in $\langle 100 \rangle$, $\langle 111 \rangle$ and $\langle 013 \rangle$

orientations under carefully chosen imaging conditions using a 400 keV HREM (Bourret *et al* 1988a). Discrimination between atomic species on the basis of image spots of different intensity can also be achieved under special conditions for compound semiconductors with sufficiently different atomic numbers using the $\langle 100 \rangle$ orientation (Ourmazd *et al* 1986) and the $\langle 013 \rangle$ orientation (Bourret *et al* 1988a). This possibility proves to be particularly useful in the three-dimensional analysis of interfaces between dissimilar materials.

4.1.1. Dislocations. In elemental and compound semiconductors, dislocations generally lie along $[110]$ directions, often being dissociated into partial dislocations separated by an intrinsic stacking fault. The partial dislocations can be identified by imaging in the $[110]$ projection (Olsen and Spence 1981) but, as might be expected from above, individual atomic columns have not been resolved in the structural studies reported so far, which has thus made detailed defect analysis more difficult to accomplish. Nevertheless, extensive comparisons with simulated images for various models of Lomer edge dislocation cores in Si and Ge enabled atomic columns to be located to within ~ 0.025 nm, even though the possibility of impurity segregation to the dislocation core could not be ruled out (Bourret *et al* 1982). Similarly, HREM analysis of dissociated 60° dislocations in CdTe showed that possible structural models (glide set and shuffle set) could be clearly differentiated, and that atomic positions could be identified with high accuracy (Lu and Smith 1990). By using quantitative image comparisons and the improved microscope resolutions that have recently become available, far better modelling of dislocation core structures in semiconductors should nowadays be possible, and this activity would again appear to be worth pursuing.

4.1.2. Interfaces. The ideal interface for examination by HREM should be flat and edge-on to the incident beam direction, it should only contain interfacial steps that project through the entire depth of the crystal, and the crystals on both sides of the boundary should preferably be orientated to a low-index zone axis. Many semiconductor grain boundaries (GBs) and heteroepitaxial interfaces meet these criteria. For example, high-resolution observations of several pure tilt GBs in elemental Ge and Si bi-crystals provided the basis for the development of plausible atomic models, which were then used for trial-and-error adjustments of atomic positions through comparisons with simulated images (d'Anterroches and Bourret 1984). The $(510)\Sigma = 13[001]$ pure tilt GB in Si was found to have an aperiodic core structure which could be described in terms of a mixture of dislocations (Kim *et al* 1992). The $(130)\Sigma = 5$ GB in Ge was studied in $[001]$ and $[013]$ projections, thus enabling a complete three-dimensional crystallographic analysis to be performed (Bourret *et al* 1988b). The $(112)\Sigma = 3$ GB in Ge was shown by observations in two projections to have a $c(2 \times 2)$ periodic supercell of the geometrical coincidence lattice of the boundary (Bourret and Bacmann 1985). Planar defects in compound semiconductors, such as twin boundaries and stacking faults, have generally received less attention than those in Ge and Si. Nevertheless, as demonstrated by the image of a $\Sigma = 3\{111\}$ GaP twin boundary shown in figure 7, the latest generation of atomic-resolution microscopes can clearly discriminate between closely spaced atomic columns in thin crystal regions, and in this particular example, the rotation-twin nature of the boundary could be unambiguously identified (Philipp 1996).

Heterojunctions are of immense practical importance, especially to the semiconductor industry, and it is thus not surprising that they have received much recent attention. Interface roughness can often be made apparent by choosing appropriate thickness and defocus values to emphasize contrast differences between the materials. Composition gradients can be assessed from the abruptness with which the two characteristic contrast

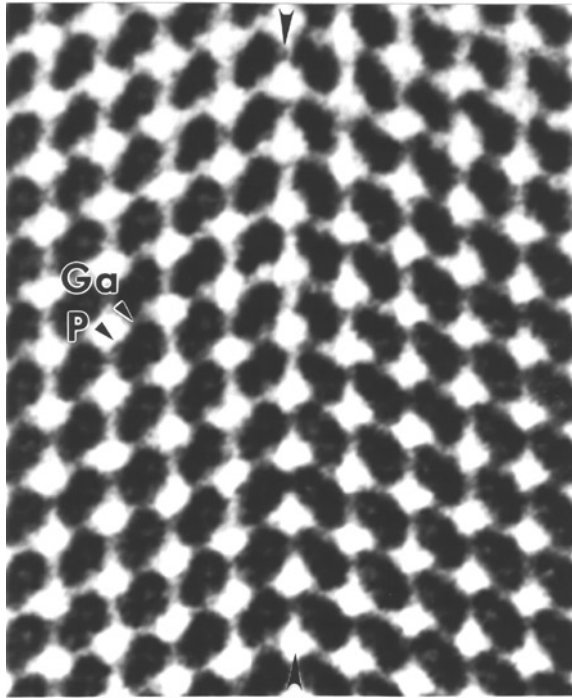


Figure 7. Atomic-resolution electron micrograph of $\Sigma = 3$ twin in GaP showing contrast differences between Ga and P atomic columns. Asymmetric contrast at boundary plane (arrowed) allows the structure of the rotation twin to be determined directly (from Philipp 1996).

motifs terminate at the interface. Chemical lattice imaging, described later in section 5.6, enables quantification of interfacial chemistry for some materials with closely matched lattice spacings, as demonstrated for example in InGaAs/InP interfaces (Ourmazd *et al* 1987) and GaAs/AlAs multilayers (de Jong *et al* 1987, Ourmazd *et al* 1990). For materials with large lattice mismatch, significant image features can usually be interpreted without resorting to special defocus/thickness combinations. Representative examples include GaAs/Si(111) and InP/Si(111) where the misfit was accommodated by hexagonal dislocation networks (Cerva *et al* 1995). Structure determination in terms of exact location and identification of individual atomic species still requires, however, that careful comparisons are made with image simulations. Recent examples of large misfit systems where the atomic structure of interfacial misfit dislocations have been successfully determined include the GaAs/Si(001) interface studied by Gerthsen (1993) and later by Vila *et al* (1995), the CdTe(001)/GaAs(001) interface examined by Angelo and Mills (1995) and McGibbon and Pennycook (1995), and the CdTe(111)/GaAs(001) interface studied by Bourret *et al* (1993). The atomic structure at epitaxial $\text{CaF}_2/\text{Si}(111)$ interfaces was determined to have a dramatic impact on electrical properties (Batstone *et al* 1988). The misfit observed at epitaxial Al-Si interfaces was successfully modelled (Legoues *et al* 1986).

Silicide-silicon interfaces have also been studied extensively by high-resolution electron microscopy, with particular emphasis being given to relating the interfacial structure with the electronic properties, especially the Schottky barrier height which is expected to depend critically upon the bonding configuration across the boundary. Early modelling studies included, for example, the cube/cube A-type ($\Sigma = 1$) and twin B-type ($\Sigma = 3$)

NiSi₂/Si(111) interfaces as formed by epitaxial silicide growth (Cherns *et al* 1982). The atomic facetting of asymmetrical twins and asymmetrical 'hetero'-twins has been investigated by careful matching of model simulations (Chen and Chen 1993). Later studies of the same materials system focused upon buried silicide layers as formed by high-dose implantation followed by rapid thermal annealing (Portier *et al* 1995). Similar structural studies have also been reported for various CoSi₂ (*A*, *B*)/Si(111) interfaces (Bulle-Lieuwma *et al* 1989, Hull *et al* 1990, Catana *et al* 1992), and for buried CoSi₂/Si(001) layers as grown by ion implantation/annealing (Hull *et al* 1990, Werner *et al* 1993). Detailed contrast analysis involving multiple structural models for the TiSi₂/Si(111) interface suggested that a terminating Ti plane directly abutted an Si plane with triple dangling bonds (Catana *et al* 1989).

4.2. Metals

Defects in metals, and metallic alloys generally, pose greater challenges for characterization by atomic-resolution electron microscopy than those associated with semiconductors. Because of their reduced unit-cell dimensions, atomic imaging in metallic systems is restricted to comparatively few low-index zone axes even with the latest generation of atomic-resolution instruments. Smaller lattice spacings result in shorter Fourier periods, and hence greater sensitivity of the image appearance to small changes in the objective lens focus settings. Moreover, successful high-resolution imaging requires very thin foils but substantial atomic rearrangements, especially relaxation in the vicinity of lattice defects and crystal surfaces, might be anticipated to alter the defect structure so that it is no longer typical of the bulk. It is therefore advisable where possible to ascertain whether any thin foil effects may have affected the image appearance (Mills and Daw 1990, Mills *et al* 1994). Conversely, atomistic calculations of grain boundary structure in metals using, for example, the embedded atom method (Daw and Baskes 1983) or pseudopotential theory, have received much attention over the years (Vitek and Srolovitz 1989). Since the results of these simulations are frequently used to predict important physical and mechanical properties, experimental observations are required for evaluation and validation purposes.

4.2.1. Grain boundaries and interfaces. Early high-resolution studies of edge and 60° dislocations at low-angle GBs in Al at 100 keV required tilted illumination (Penisson and Bourret 1979), and details of the atomic structure within about 0.5 nm of the dislocation core were unavailable. Studies of thin Au foils with a high-voltage HREM using axial illumination (Ichinose and Ishida 1981, Ishida *et al* 1983) demonstrated that the atomic configurations at [110] tilt GBs could be modelled directly from the image appearance. Figure 8 shows an example of a 6° [001] symmetric tilt GB in Al with prominent $\frac{1}{2}$ (110) edge dislocations that accommodate the tilt misalignment between the two grains (Shamsuzzoha *et al* 1990). In this atomic-resolution electron micrograph, each black spot corresponds to the location of a projected Al atomic column so that the defect structure along the boundary can be deduced unambiguously from the image. High-resolution observations of symmetrical (110) tilt GBs in Au established the presence of different recurring structural units (Ichinose *et al* 1985, Krakow 1990), and the atomic structure of several low-angle GBs in Au was determined (Krakow and Smith 1987). Structural characterization of a [100] 45° twist plus 17.5° tilt GB in Al was done directly from atomic-resolution images, and revealed that this particular asymmetrical GB was composed of a mixture of two basic structural units (Shamsuzzoha *et al* 1991). Atomic imaging of a $\Sigma = 41$ GB in bcc Mo enabled the direct identification of two different Burgers' vectors at the boundary (Penisson

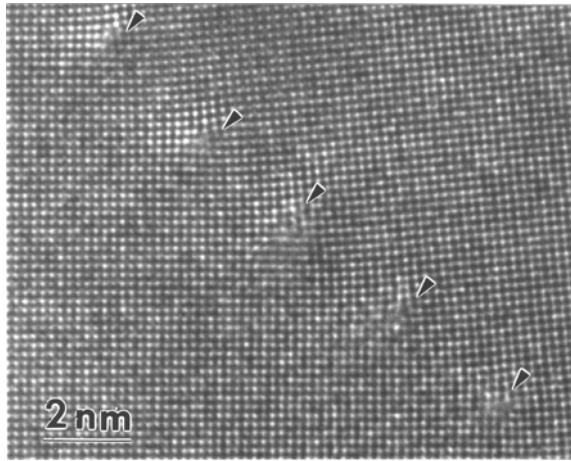


Figure 8. Atomic-resolution electron micrograph of a 6° [001] symmetric tilt grain boundary in Al with misfit accommodated by $\frac{1}{2}\langle 110 \rangle$ edge dislocations (arrowed). Each black spot in the image corresponds to the projection of each individual Al atomic column (from Shamsuzzoha *et al* 1990).

et al 1982). Further studies of a $\Sigma = 41$ GB in Mo, which also included a trial-and-error process of matching image simulations and experimental micrographs, confirmed that the boundary core had a capped triangular prism structure (Bourret *et al* 1988b). Observations of another Mo bicrystal revealed the presence of both $\Sigma = 25$ and $\Sigma = 41$ structural units along the GB (Penisson *et al* 1988), and the effect of carbide precipitates on the structure of a $\Sigma = 5$ Mo bicrystal has been investigated (Penisson *et al* 1994). Bi segregation was reported to modify the structure of grain boundaries in Cu (Luzzi 1991): GBs became faceted and an ordered Bi layer was observed at a $\Sigma = 3$ twin boundary (Luzzi *et al* 1991).

Structural modelling based upon atomistic simulations has accompanied many recent atomic-resolution studies of GBs in fcc and bcc metals. For example, the incoherent $\{112\}$ twin GB in fcc Al was observed with a high-voltage HREM (Penisson *et al* 1991a), and comparisons were made with structures calculated using the embedded atom method (EAM). Within the reported accuracy of ~ 0.02 nm, no rigid-body translation at the GB was observed. A subsequent study of the same boundary, in a bicrystal specifically prepared to avoid constraints due to other neighbouring structures, did, however, observe a rigid-body shift parallel to the boundary (Medlin *et al* 1993). In the case of the $\Sigma = 99\{557\}\langle 110 \rangle$ tilt GB in Al, structural models were deduced using both EAM and pair-potential approaches, but careful comparisons of experimental and simulated images did not permit the predictions of the two methods to be differentiated because of their very close similarity (Dahmen *et al* 1990). For the $\Sigma = 9(221)[110]$ GB in Al, glide-plane and mirror-plane symmetric structures were observed to alternate periodically along the boundary: the predictions of the various atomistic modelling approaches could only be distinguished for one of these two structures but not the other (Mills and Daw 1990, Mills *et al* 1992). For the (310) twin in bcc Nb, the atomic structure of the boundary was generated using interatomic potentials derived from several theoretical approaches but only one of these, the so-called model-generalized pseudopotential theory (MGPT), successfully predicted the mirror symmetry later observed in the experimental image (Campbell *et al* 1993a), reportedly because of its ability to incorporate angle-dependent interactions. For the $\Sigma = 25(710)/[001]$ twin in Nb, a multiplicity of stable, low-energy structures were predicted by EAM: four possibilities

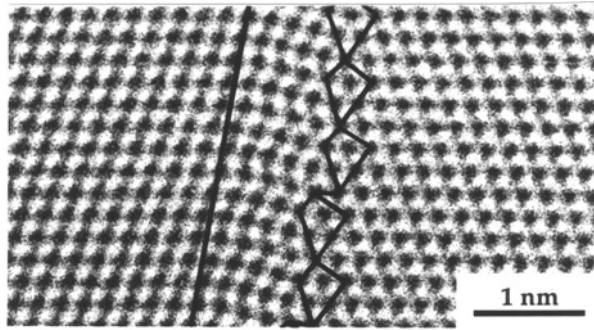


Figure 9. Atomic-resolution electron micrograph of the $\Sigma = 82^\circ$ grain boundary in Cu, recorded with the ARM-1250 HREM in Stuttgart, showing the presence of the predicted rhombohedral $9R$ phase located between the large-angle grain boundary at the right (structural units outlined) and the small-angle boundary at the left. Black spots represent positions of individual Cu atomic columns (from Hofmann and Ernst 1994a).

out of 13 remained after careful comparison with experimental micrographs (Campbell *et al* 1993b). Molecular dynamics simulations of the $\Sigma = 3\langle 110 \rangle (211)$ twin boundary in fcc Ag predicted a thin boundary phase having the rhombohedral $9R$ structure, and this prediction was confirmed by experimental atomic-resolution micrographs (Ernst *et al* 1992). Figure 9 is an experimental image showing the existence of the same rhombohedral phase at an incoherent $\Sigma = 3 (211)$ boundary in fcc Cu (Hofmann and Ernst 1994a). Predictions based on molecular dynamics simulations that the asymmetrical $84^\circ (211)$ tilt GB in Cu should contain a band of bcc structure in the GB region have also been verified (Schmidt *et al* 1995). High-resolution observations have confirmed recent atomistic simulations which implied that the width of the $9R$ phase depends on the shear loading parallel to the interface (Campbell *et al* 1996).

Atomic-level structural investigations of boundaries in intermetallic alloys and several metal/metal systems have been reported. For example, the $\Sigma = 5 [001](310)$ GB in NiAl was imaged by high-resolution electron microscopy and analysed with the assistance of image simulations (Fonda and Luzzi 1993): changes in local stoichiometry and a rigid-body translation along, but not normal to, the boundary were inferred. A more recent quantitative study of the $\Sigma = 3 (111)$ GB in NiAl, also using digital image processing, enabled atomic positions at the boundary core to be determined with an accuracy of ~ 0.015 nm (Nadarzinski and Ernst 1996). The atomic structure and elastic fields associated with precipitate/matrix interfaces in an (Ni, Co) superalloy have been investigated (Loubradou *et al* 1993). Deformation defects associated with structural twin plates in TiAl were characterized (Loubradou *et al* 1995) and translation-twin interfaces in TiAl were also investigated (Zheng *et al* 1994). Semicohherent Ag/Ni and Au/Ni heterophase interfaces have been studied, and the atomic structure of the misfit dislocations was confirmed using image simulations (Gao and Merkle 1990). The deformation and chemical profiles of strained Au/Ni multilayers have been analysed quantitatively using image processing (Bayle *et al* 1994).

4.2.2. Dislocations. Determination of the atomic structure of dislocation cores in elemental metals at least is simplified by the presence of only one atomic species. However, it is also complicated by the likelihood that the core may not be stable in foils thin enough for atomic-resolution viewing due to the possibility of core spreading or even defect motion in the form

of glide to the thin foil edge (Mills *et al* 1994). Moreover, structural rearrangements during high-resolution observations of thin metal foils have been observed by many workers (see, for example, Ichinose and Ishida 1989, Mills and Stadelmann 1989, Medlin *et al* 1997). Nevertheless, significant atomic-resolution studies of dislocations in metals and intermetallic alloys have been reported. In an early study, $\frac{1}{3}\langle 1120 \rangle \{1010\}$ edge dislocations in α -Ti were determined to have a planar elongated core structure (de Crecy *et al* 1983). The atomic structure of Lomer and 60° dislocations associated with small-angle asymmetric $[110]$ tilt GBs in Al were characterized on the basis of extensive image simulations of trial structures generated using the elasticity theory (Mills and Stadelmann 1989). The climb and glide of $a/3\langle 111 \rangle$ dislocations in Al due to the influence of electron irradiation has been analysed (Medlin *et al* 1997). Atomic modelling of the core structure of $a\langle 100 \rangle$ and $a\langle 110 \rangle$ dislocations in the intermetallic alloy NiAl revealed that the former had large elastic strain fields but were usually undissociated, whereas the latter either decomposed into other types of dislocations or climb-dissociated into two partial dislocations (Mills and Miracle 1993). An investigation of dislocation core structures in the ordered intermetallic alloy TiAl has also been reported (Hemker *et al* 1993).

4.2.3. Metallic alloys and quasicrystals. Binary and ternary metallic alloys form a rich variety of superlattice structures that are of much interest. In several important binary systems, the alloys are well ordered, at least along one projection axis, and selective imaging conditions can be established such that information about atomic structure and ordering at defects and boundaries can be directly inferred without requiring atomic resolution (for further details, see the reviews by Amelinckx *et al* 1985, 1993). In general, however, small interatomic separations and chemical identification of individual atomic columns represent severe challenges to the electron microscopist. Image simulations are essential before the often subtle changes in image features can be related to structural rearrangements. A notable example was the observation of tetragonal distortions and atomic structure in Nb_3X ($\text{X} = \text{Sn}, \text{Al}, \text{Ge}$) superconductors (Takeda *et al* 1985, 1988). The atomic structure of CuAu II was studied by high-resolution electron microscopy and the atomic arrangements of faulted domains were also discussed (Takeda and Hashimoto 1985). Quasicrystals lack periodic translational order, which generally preclude comparisons with atomistic models, while experimental images can be extraordinarily sensitive to thickness and defocus values thus making image interpretation in terms of atomic structure very difficult (Krakow *et al* 1993). Nevertheless, some limited successes have been reported. For example, a structural model for an Al–Ni–Co decagonal quasicrystal was determined (Hiraga *et al* 1991), and atomic arrangements associated with an Al–Pd–Mn quasicrystal with 1.2 nm periodicity were proposed (Hiraga and Sun 1993). Plate-like precipitates known as Guinier–Preston (GP) zones are found in many alloys following annealing treatments. Structure images have been recorded (Dorignac *et al* 1980), and computer simulations of structural models to match with experimental micrographs have also been reported (Ajika *et al* 1985). Monolayer and double-layer GP zones in Al–1.7%Cu have also been modelled (Jouffrey and Marlik 1993). An *in situ* study of precipitate dissolution in an Al–Cu–Mg–Ag alloy has been reported (Chang and Howe 1993).

4.3. Oxides and ceramics

Characterization of the atomic structure of defects and interfaces in oxides and ceramics can provide valuable insights into many of their physical properties, especially electrical and mechanical behaviour. For example, the presence of point defects or the build-up of space-

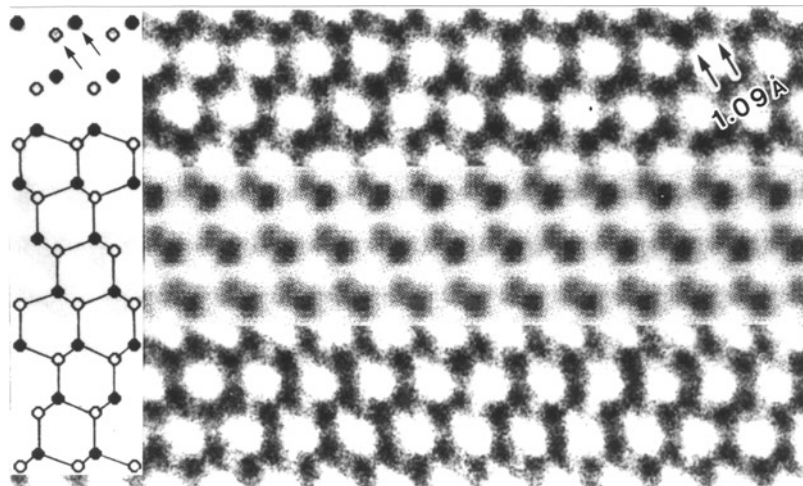


Figure 10. Atomic-resolution electron micrograph of $6H$ SiC polytype recorded with ARM-1250 HREM installed in Tokyo. The image simulation (inset) verifies the clear separation of the Si and C atomic columns (Ichinose 1994).

charge layers in the vicinity of a ceramic boundary will have serious implications for the utilization of the material in any proposed electronic devices. The nature of structural defects in oxide superconductors can have a serious deleterious influence on their current-carrying capacity. Most ceramic materials consist of two or more atomic species (the diamond form of carbon being a notable exception), and only rarely can all of the separate elements be discriminated in atomic-resolution images. The micrograph of the $6H$ polytype of SiC in the (1120) orientation shown in figure 10 is a particularly noteworthy example since the closest separation of the projected Si and C columns, which are clearly resolved, is only 0.108 nm (Ichinose 1994). It has been shown, for example by image simulations of SiC polytypes (Smith and O'Keefe 1983), that close examination of image appearance as a function of imaging conditions should enable the atomic structure of many ceramics to be determined even though not all of the atomic columns are fully resolved. Similarly, the contrast of oxide images is usually dominated by the cation sublattice with the oxygen sublattice being invisible. Still, as shown by many of the examples quoted here, knowledge of the cation column positions, when combined with crystal-chemistry considerations, often suffices to enable the entire structure of quite complicated unknown materials to be deduced (see, for example, Lundberg *et al* 1989). The examples described in the following paragraphs progress in complexity from simple binary oxides such as MgO and NiO, through ternary oxides such as $BaTiO_3$, to high-temperature superconducting oxides and oxycarbonates. As well as carbides and nitrides, examples of metal-ceramic and ceramic-oxide interfaces are also briefly reviewed. Finally, it should be noted here that special care should be taken to avoid structural modification during preparation of ceramic and oxide samples for electron microscopy because artefactual image detail is otherwise reported as likely to be produced (Carter *et al* 1989).

Structure imaging in the electron microscope originated with large-unit-cell block oxides, although the structural interpretation was initially based on white-spot image contrast corresponding to the location of tunnels in these materials (Iijima 1971, Hutchison and Anderson 1972). On this basis, many structural studies of non-stoichiometric and doped oxides, as well as mixtures of oxides, have been successfully completed (for a

comprehensive review, see Eyring 1988). Subsequent improvements in resolution to better than 0.2 nm led to oxide images in which the black spots visible at optimum defocus were interpretable in terms of atomic column positions. It then became possible, for example, to deduce directly the detailed atomic structure of complicated shear defects and precipitation phenomena observed in doped and slightly reduced tungsten trioxide (Bursill and Smith 1984, Bursill *et al* 1988). Image simulations were used to confirm the defect image interpretability (Evans *et al* 1986), and also demonstrated that, under appropriate imaging conditions (i.e. properly adjusted beam and crystal tilt, correct defocus), the tungsten atom columns could be located with high accuracy ($\sim \frac{1}{10}$ th of an interatomic spacing). For the synthetic ceramic Al_2TiO_5 , cationic disorder was successfully investigated on the basis of detailed comparisons with simulated images over a range of defocus values (Epicier *et al* 1991). For chromia-doped rutile, it was established from direct observation of atomic arrangements that extended 'crystallographic shear' defects were, in fact, quite disordered (Wood *et al* 1983).

4.3.1. Dislocations and grain boundaries. Much recent attention has been directed towards well defined structural defects, such as the types that have already been described for metals and semiconductors. The atomic structures of dislocations in MgO, as caused both by plastic deformation and ion irradiation, were characterized (Ohta *et al* 1994): the atomic positions used in the matching image simulations were calculated according to isotropic elasticity theory and gave reasonable agreements with experimental images for non-dissociated end-on edge dislocations. Symmetric tilt grain boundaries in NiO bicrystals were found to have a multiplicity of distinct core structures or structural units (Merkle and Smith 1987). For example, the two asymmetric structural models deduced from experimental micrographs for the $\Sigma = 5$ (310) GB both differed from the symmetric models derived earlier using theoretical considerations, and the lattice expansion perpendicular to the GB plane was substantially less than calculated theoretically. Model atomic structures have been compared with observations of the $\Sigma = 5$ (210)/[001] symmetric tilt GB in yttrium aluminum garnet (Campbell 1996). As shown in figure 11, structural investigations of a near- $\Sigma = 5$ (210) GB in TiO_2 , rutile, revealed a stepped boundary with well defined lattice dislocations at the steps, and extended, flat terraces that consisted of $\Sigma = 5$ (210) segments with mirror glide symmetry (Dahmen *et al* 1994): structure refinement based on the images indicated a deviation in local O stoichiometry from TiO_2 towards Ti_2O_3 and the rigid shift expansion normal to the boundary was measured as 0.044 ± 0.008 nm (Paciornik *et al* 1996).

Considerable success has been achieved in atomistic studies of grain boundaries even though the oxygen atomic columns have not in general been resolved. Observation of an undoped $\Sigma = 5$ (130) symmetrical tilt GB in SrTiO_3 revealed that it was composed of repeating structural units, and careful analysis enabled the rigid body translation along the boundary plane to be determined (Ravikumar and Dravid 1993). Examination of a 25° [001] tilt boundary in SrTiO_3 enabled an initial structural model for the boundary to be proposed: bond-valence sum calculations based on electron-energy-loss spectroscopy at the boundary were then used to refine the O atom positions (McGibbon *et al* 1994). A high-angle annular-dark-field image of this boundary is shown later and discussed briefly in section 5.8. In a subsequent related study of a 45° asymmetric [001] tilt boundary, the presence of half-occupied Ti–O columns was proposed (McGibbon *et al* 1996). Yet another quantitative structural study of a $\Sigma = 3$ (111) GB in SrTiO_3 showed that shear stresses caused a loss of mirror symmetry across the boundary plane and reduced excess volume relative to unstressed material (Kienzle and Ernst 1997). A combined structural and

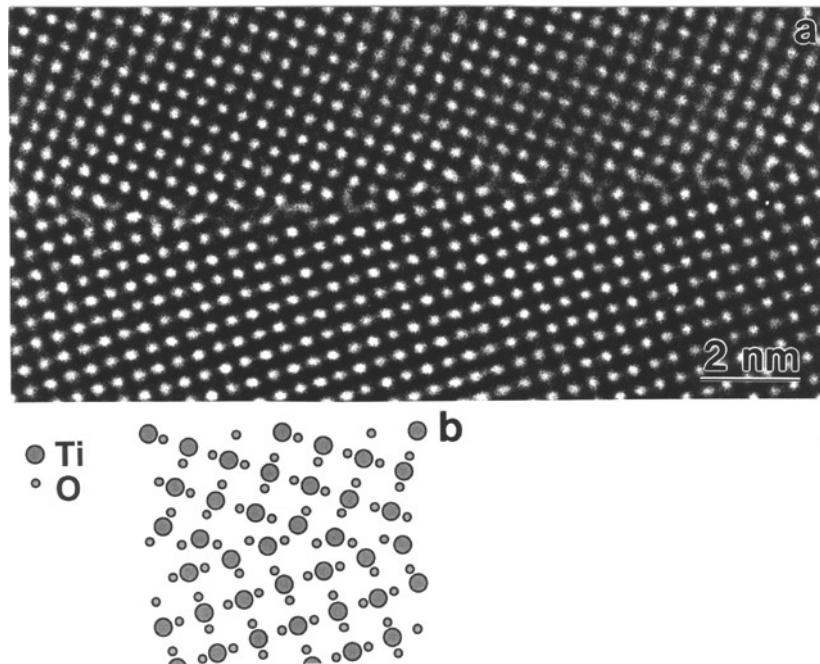


Figure 11. (a) Atomic-resolution electron micrograph of $\Sigma = 5$ (210) grain boundary in TiO_2 (rutile) showing the steps and repeating structural units; (b) corresponding structural model (from Dahmen *et al* 1994).

spectroscopic investigation of coherent (111) twins in BaTiO_3 enabled a modified structural model of the boundary to be proposed (Recnik *et al* 1994). The atomistic structure of 90° domain walls in ferroelectric PbTiO_3 thin films was investigated by using digital processing to determine lattice parameter variations across the walls (Stemmer *et al* 1995). The atomic structure of a $\Sigma = 7$ (01 $\bar{1}$ 2) symmetric tilt GB in $\alpha\text{-Al}_2\text{O}_3$ was found to be based on the coexistence of two distinct interfacial domains that both had oxygen interfacial layers but different structural widths (Chen *et al* 1995).

4.3.2. Superconducting oxides. Electron microscopy, especially imaging at the atomic level, has been pivotal in developing a broad understanding of the influence of structural defects on the superconducting properties of many large-unit-cell perovskite oxides. For example, the atomic structure of planar stacking faults, rotation twins and intergrowths in $\text{YBa}_2\text{Cu}_3\text{O}_{7-\delta}$ ('YBCO') can nowadays be modelled easily and directly from the appearance of the high-resolution electron micrograph (for a review of early work, see Zandbergen and Van Tendeloo 1990). The known structure of the surrounding matrix material proves to be highly advantageous in terms of enabling the objective lens defocus and the local specimen thickness to be determined accurately. Figure 12 shows an atomic-resolution electron micrograph of a 90° twin boundary in YBCO—the image simulation (inset) again confirms the image interpretability in terms of the direct correspondence of the black-spot contrast to the projected metal cation columns (Barry and Anstis 1994). Similar grain boundaries in YBCO have been modelled during studies of thin-film step-edge junctions deposited on LaAlO_3 substrates (Jia and Urban 1993). The atomic structure of interfaces in epitaxial YBCO/PrBCO/YBCO triple-layer films has been investigated (Jia *et al* 1995).

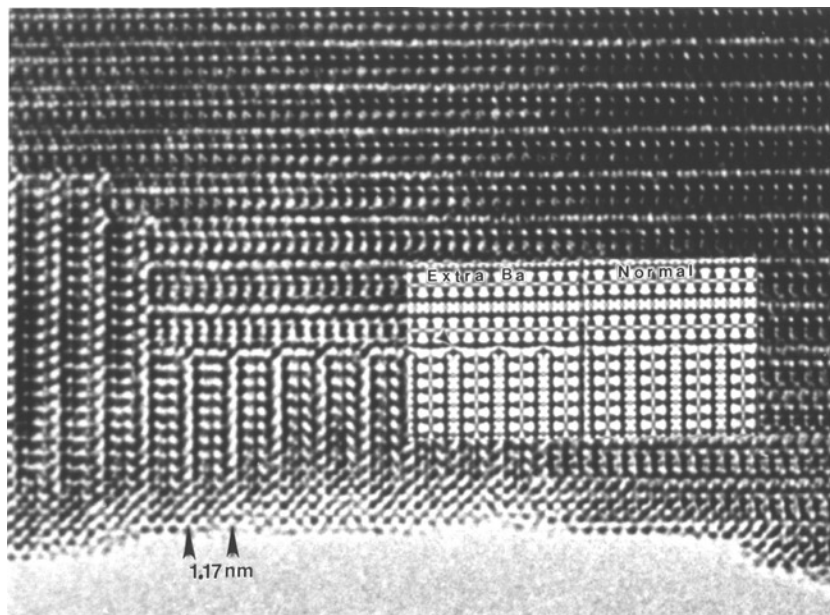


Figure 12. Atomic-resolution electron micrograph of 90° twin in a YBa₂Cu₃O₇ high-temperature superconductor. Image simulations (inset) confirm that black spots correspond to projected metal-atom columns (from Barry and Anstis 1994).

The recent scientific literature contains many further high-resolution studies of Bi-, Hg-, and Tl-based cuprate superconductors, far too many to describe here. In one quantitative study of particular note, the detailed atomic structure of planar defects in an infinite-layer Sr–Ca cuprate was determined with a positional accuracy of close to 0.01 nm (Zhang *et al* 1995). The partial substitution of Cu by aliovalent Co and Ga in YSrCuO led to the development of complex superstructures (Krekels *et al* 1993). Superstructures and intergrowth defects have also been reported to occur in several series of oxycarbonate superconductors prepared under high pressure conditions: further details can be found in the comprehensive review by Matsui and Akimitsu (1995). Figure 13 shows a representative region from the oxycarbonate phase (Cu_{0.5}C_{0.5})Ba₂Ca₂Cu₃O₉, together with the corresponding structural model (Kawashima *et al* 1994).

4.3.3. Interfaces. Recent attention has been directed towards the epitaxial growth of high-quality thin films and multilayers. Epitaxial films of YBCO were deposited on Si(001) using Y₂O₃ and yttria-stabilized zirconia buffer layers: interfaces were found to be atomically sharp and essentially planar with isolated steps (Bardal *et al* 1993). Superlattices of YBCO/PrBCO were deposited on [001] SrTiO₃ substrates, and the resulting interface steps and growth terraces were characterized (Jia *et al* 1993). Growth interfaces and mismatch defects for YBCO deposited on SrTiO₃ and LaAlO₃ have been characterized on the atomic level (Ramesh *et al* 1991) and high-angle GBs for YBCO that was deposited on MgO were carefully examined (McKernan *et al* 1992). The epitaxial growth of Au electrical contacts on (001) YBCO was also investigated, and the formation of the intermetallic alloy phase Au₂Ba was proposed (Jia *et al* 1997). Epitaxial multilayers of SrTiO₃/BaTiO₃ were deposited by pulsed laser ablation using intensity oscillations in reflection high-energy

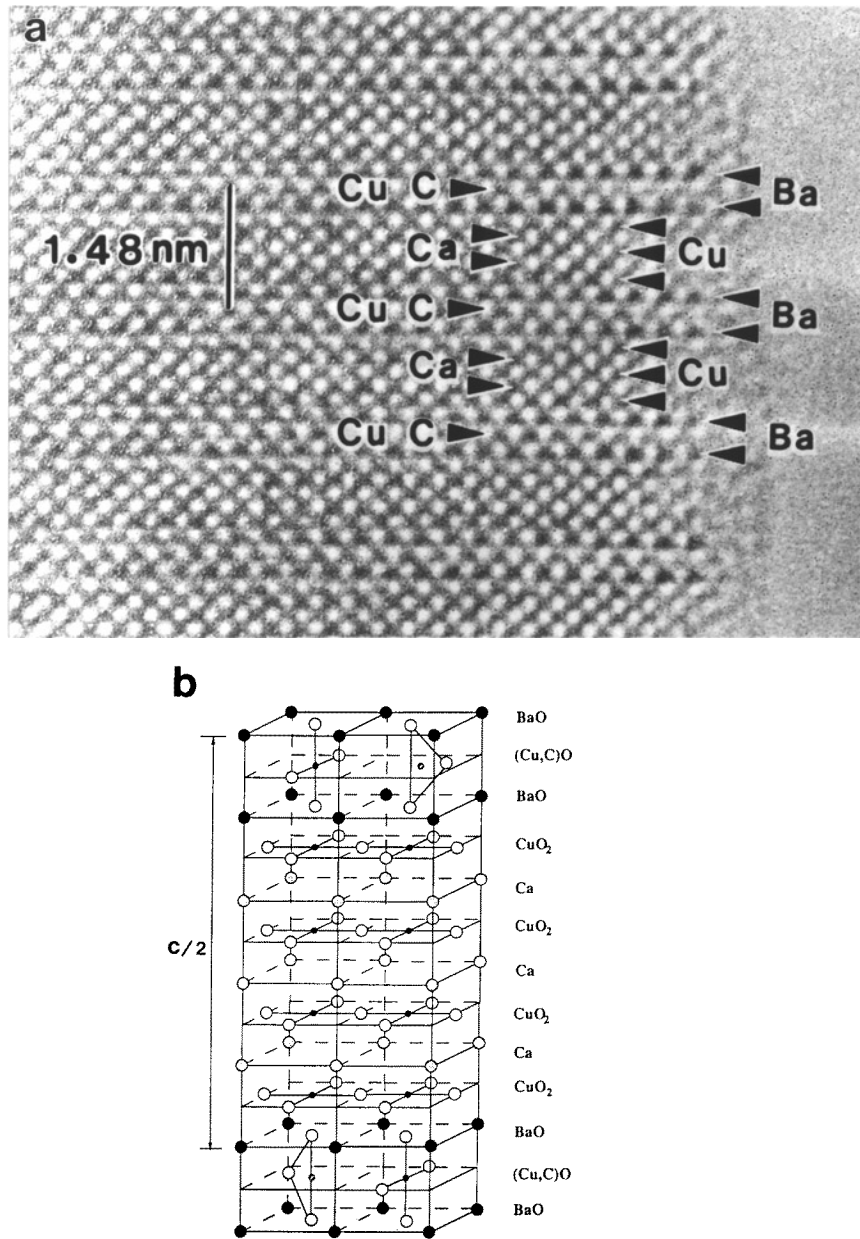


Figure 13. (a) Atomic-resolution electron micrograph from $(\text{Cu}_{0.5}\text{C}_{0.5})\text{Ba}_2\text{Ca}_2\text{Cu}_3\text{O}_{9+\delta}$ oxycarbonate superconductor recorded with H-1500 HREM installed in Tsukuba. Black spots represent metal-atom columns as indicated. (b) Schematic diagram of the corresponding crystal structure (from Kawashima *et al* 1994).

electron diffraction spots to control the layer thicknesses, which were varied from 1 up to 16 unit cells (Shaw *et al* 1994). The lattice mismatch at the interface between ZrO_2 and Al_2O_3 was accommodated by a combination of misfit dislocations and ledges (Heuer *et al* 1985). Epitaxial films of $\text{La}_x\text{Sr}_{1-x}\text{CoO}_3$ grown on $\text{MgO}(001)$ consisted of a domain

structure with numerous stacking faults, in addition to a novel anisotropic perovskite-type structure that was successfully modelled (Wang and Zhang 1995). Modulated structures in the homologous series of layered compounds $\text{In}_2\text{O}_3(\text{ZnO})_m$ ($m = 3, 6, 10, 13, \dots$) were investigated by high-resolution electron microscopy (Li *et al* 1997).

Metal-ceramic interfaces are of much scientific and technological relevance, especially for the development of useful composite materials. Knowledge of the interfacial structure, especially the inevitable dislocations that must accommodate any large lattice mismatch, promotes a better understanding of bulk mechanical properties. In the case of vanadium deposited on the basal plane of sapphire, computer simulations clearly established that the sapphire was aluminum-terminated, although ambiguity over two alternative structural models still remained (Ikuhara and Pirouz 1993). Misfit dislocations and lattice relaxations at diffusion-bonded Nb/sapphire interfaces were characterized (Knauss and Mader 1991). In a comparative study of Nb and Mo deposited on the *R*-plane of sapphire, misfit dislocations were found to be offset from the interface for Nb whereas they were localized very close to the interface for Mo (Tricker and Stobbs 1995). Interactive digital image matching was used in another comprehensive study of the niobium/sapphire interface: translation vectors were determined with a precision of ~ 0.01 nm (Möbus and Rühle 1994). In yet another study of the same interface, the atomic core structure of the dislocations was determined (Gutenkunst *et al* 1994). Atomic-resolution studies of thin copper films grown on sapphire indicated that the atomic structure of the interface was incoherent for films grown at 200°C (Dehm *et al* 1995). Vanadium/magnesium oxide and magnesium oxide/vanadium interfaces (Ikuhara *et al* 1995) changed from being coherent for films below a certain critical thickness to either semicoherent (V-MgO) or with an interfacial spinel compound (MgO-V).

4.3.4. Ceramics. It was noted above that because most ceramics are close-packed materials based on tetrahedral bonding, true atomic resolution is very difficult to obtain. Nevertheless, several studies are worth mentioning. Careful examination of {100} nitrogen platelets in diamond led to the development of a novel 'nitrogen-fretwork' model (Barry 1991), while later observations led to a more refined model (Fallon *et al* 1995). The crystal structures of the α - and β -forms of silicon nitride were observed by high-resolution electron microscopy, and an atomic model for a structural defect in β - Si_3N_4 was proposed (Hiraga *et al* 1983a). Precipitates of TiN in matrices of β - Si_3N_4 had well defined orientation relationships with the matrix (Hiraga *et al* 1983b). Interfacial structures and the defects that occurred during heteroepitaxial growth of β -SiC films on TiC substrates have been characterized (Chien *et al* 1994). The atomic structure of Ti(C,N)- TiB_2 interfaces was investigated using a combined microscopy-simulation study (Dai *et al* 1994a), and TiB_2/NiAl interfaces were also examined (Dai *et al* 1994b).

4.4. Surfaces

There are several possible configurations for eliciting information about surfaces using the electron microscope (see, for example, Smith 1986, Yagi 1987). Reflection electron microscopy utilizes high-order diffracted beams to provide atomic-scale information in the direction normal to the surface, but the lateral resolution is limited by the small size of the objective aperture that must be used for image formation. Surface imaging using standard transmission electron microscopy of bulk samples suffers from the fact that the final image intensity distribution includes strong contributions from the bulk crystal that tend to overwhelm any surface contrast which is usually comparatively weak. Only under very well characterized and highly specific conditions can single atom imaging be achieved: for

example, adsorbed Bi atoms have been identified on reconstructed Si(111) surfaces using an ultrahigh-vacuum (UHV) transmission electron microscope (Haga and Takayanagi 1991), and the overgrowth of Au on ZnTe has been investigated (Shiojiri *et al* 1983). In surface profile imaging (Smith *et al* 1989b), the electron microscope is operated in the normal, high-resolution imaging mode with a large objective aperture. For a thin, properly aligned sample, with a surface that is free of any oxide or contamination overlayer, the optimum defocus image displays the surface profile at the resolution limit of the instrument. The technique was effectively initiated with observations of CdTe surfaces (Sinclair *et al* 1981), and it was first applied at atomic resolution to observations of a 2×1 reconstruction of the gold (110) surface (Marks and Smith 1983). An outward relaxation of $20 \pm 5\%$ for the outermost row of gold atoms on the same surface was later documented using careful analysis of image behaviour as a function of defocus (Marks 1984).

A wide variety of surfaces, including metals, oxides and semiconductors, have since been studied using the profile imaging method: some dynamic experiments using the technique are reported in the following section. Gold initially received much attention, mainly because its surface was relatively inert and electron irradiation readily caused desorption of surface contamination overlayers (Marks 1984). In addition, the large interatomic spacings of gold and the high atomic-column visibility due to its high atomic number, made it easy to characterize the atomic rearrangements that occurred on extended Au (110), (111) and (100) surfaces (Smith and Marks 1985). In later experimental studies involving *in situ* Au evaporation under UHV conditions, the $\times 5$ superperiod associated with the corrugated (5×28) reconstructed Au surface was observed (Hasegawa *et al* 1986), and further Au (110) surface profile images were reported (Ikarashi *et al* 1988). The theoretical contrast of adsorbed or removed atoms on Au(111) surfaces was investigated using image simulations (Isshiki *et al* 1992). An interesting 2×1 surface reconstruction caused by sulphiding Pt particles supported on alumina has been reported (Jefferson and Harris 1988).

Oxide surfaces are generally more straightforward to prepare for observation by profile imaging (Smith *et al* 1986a). However, care must be taken with many maximally valent oxides to avoid the surface modification that is likely to occur under intense electron irradiation because of electron-stimulated desorption of oxygen from near-surface regions (Smith *et al* 1987a, Buckett *et al* 1989). Indeed, pronounced black-line features that developed on (0001) polar surfaces of ruby (α -Al₂O₃) under electron irradiation were shown to consist of a monolayer having the γ -Al₃O₄ (spinel-type) structure (Bursill and Lin 1989). A complex spinel catalyst developed surface rafts, identified as ZnO, following prolonged use as an oxidation catalyst (Hutchison and Briscoe 1985). Surface profile images from MgO cubes were reported to occur as a by-product of hydroxide decomposition reactions (Dahmen *et al* 1987), and surface profile images were central to studies of terbium oxide (Kang *et al* 1986), Eu₂O₃ (Ning and Ye 1990a), and β -PbO₂ (Kang and Eyring 1987). A direct correlation was made between the exposed surface structure of V₂O₅ oxide catalysts and the catalyst selectivity (Andersson *et al* 1986). Multislice image simulations were used to investigate possible surface reconstructions, and the existence of missing or adsorbed atoms, with reference to profile images of UO₂ and TbO₂ (Lu and Smith 1988). The formation of a 60° dislocation on the (111) surface of Tb₄O₇ was reported (Ning and Ye 1990b).

Profile images of semiconductor surfaces are usually only considered to be valid if the surface has been properly cleaned within the microscope. A novel 1×1 dimer reconstruction of a Si (111) surface was reported after the sample had been heated *in situ* to 1000°C (Gibson *et al* 1985), and a 1×1 reconstruction of the CdTe (110) surface was observed once surface material had been removed by intense beam heating (Lu and Smith 1987).

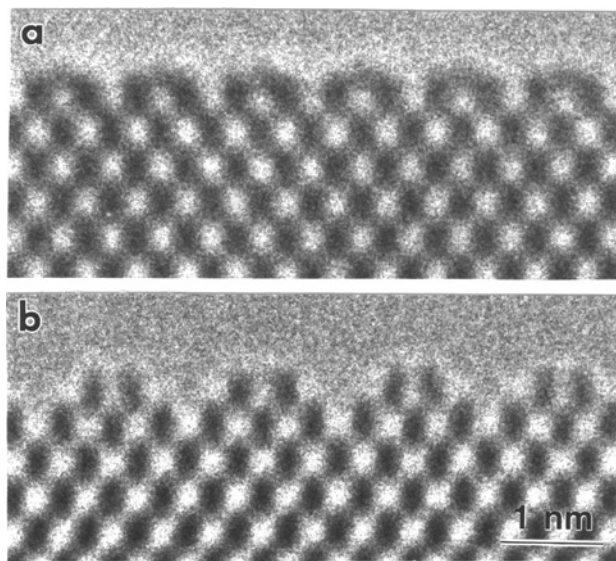


Figure 14. Surface profile images showing changes of reconstructed CdTe (001) surface at different temperatures. Elongated black spots correspond to CdTe dimer pairs: (a) 2×1 at 140°C ; (b) 3×1 at 240°C (from Lu and Smith 1991).

An anomalous reconstruction was reported to be associated with the (111) surface facets of very small ($\sim 2\text{--}10\text{ nm}$) Ge particles (Mitome and Takayanagi 1991). As shown by the representative surface profile images in figure 14, the CdTe (001) surface undergoes a reversible phase transformation from a 2×1 structure at temperatures below about 200°C to a 3×1 structure at higher temperatures (Lu and Smith 1991). Furthermore, using extensive image simulations, the atomic columns at the surface were located to within $\sim 0.01\text{ nm}$, and structural models for the two reconstructions were developed: the 2×1 was determined as being Cd-stabilized whereas the 3×1 was found to be Te-stabilized.

4.5. Dynamic events

There are basically two ways to document dynamic events that occur within the electron microscope. Changes to the specimen morphology can be followed indirectly from a comparison of sequentially recorded micrographs or directly by means of a low-light-level TV camera. It is straightforward to attach an image pick-up system to the base of the microscope lens column and thereby provide a means whereby the dynamic events can either be observed at increased magnification for the operator's convenience or else recorded on videotape for later appraisal and analysis. In principle, there should be no loss of instrumental resolving power due to the camera addition. In practice, the reduced dynamic response of the TV camera, as well as distortions across the field of view, will impair the effectiveness of TV image recording as a vehicle for quantitative image analysis. Nevertheless, this ability to document dynamic events such as phase transitions, defect motion and interface dynamics at the atomic level, greatly enhances the usefulness of the electron microscope in contributing to a better understanding of many materials' properties. Diverse applications for controlled environments (e-cell) have recently been reviewed, and the possibilities for documenting gas–solid reactions at lattice resolution within the electron microscope were also discussed (Boyes *et al* 1996). Additional papers describing dynamic

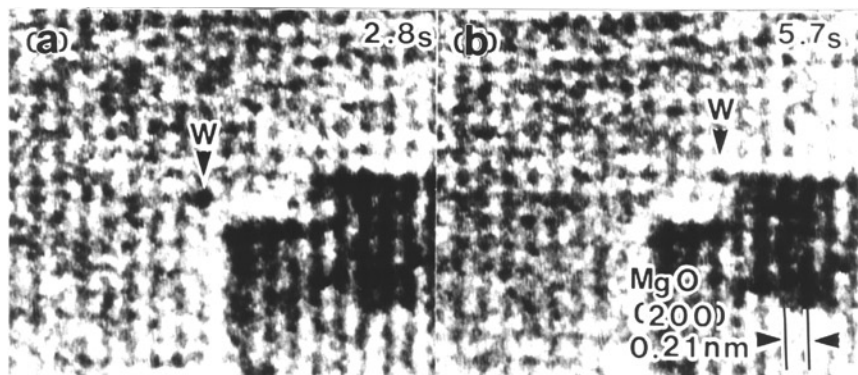


Figure 15. Atomic-resolution electron micrographs of thin [001] MgO crystal at 218°C, taken from individual frames of video recording, that shows movement of individual W atoms (arrowed) during observation (from Tanaka *et al* 1996).

in situ studies can be found in the proceedings of a recent symposium (Sharma *et al* 1996).

4.5.1. Surfaces. The motion of individual atoms or atom clusters in the electron microscope was first documented in successive scanning images recorded with the scanning transmission electron microscope. Diffusion rates and jump frequencies were estimated, for example with Ag atoms (Isaacson *et al* 1976) and U atoms (Isaacson *et al* 1971, Wall *et al* 1977). Surface profile imaging is ideally suited to atomic-resolution studies of surface dynamics (Smith 1985). Using the technique, successive exposures from extended Au (110) surfaces revealed movement of Au atomic columns (Smith and Marks 1985), while rapid structural changes and the existence of atom clouds extending out from Au surfaces were also reported (Bovin *et al* 1985). Hopping of Au columns between surface sites on small Au particles was later recorded at TV rates using the conventional transmission electron microscope (Wallenberg *et al* 1985, Iijima and Ichihashi 1985). Similar hopping of Pt columns was also studied (Wallenberg *et al* 1986). One of the most remarkable studies is illustrated by the time-sequential series of micrographs in figure 15, which shows a *single* W atom diffusing on an MgO(001) film at a temperature of 218°C, with a time resolution of $\frac{1}{60}$ s (Tanaka *et al* 1996). The image quality is not high because each image represents a single video frame. However, from a detailed analysis of individual jump frequencies, the diffusion constant and activation energy for the surface diffusion process were extracted. Electron beam irradiation effects were carefully differentiated from thermal processes by utilizing different beam current densities and substrate temperatures up to 400°C. Electron-beam-induced surface damage and subsequent annealing processes in rutile were investigated as a function of temperature with a 300 keV HREM modified for ultrahigh vacuum and equipped with a specimen heating holder (McCartney and Smith 1991).

4.5.2. Small particles. Under strong electron irradiation, small metal particles (< 8–10 nm) were observed to rapidly change their shape and orientation. For example, structural rearrangements from single crystal twinned to multiply twinned were observed in small Au particles (Smith *et al* 1986b, Iijima and Ichihashi 1986). Structural rearrangements as well as surface hopping were also documented in small particles of Pt (Wallenberg *et al* 1986) and Rh (Petford-Long *et al* 1987). In the case of small Ru particles (~2.5 nm), the

internal stacking changed between cubic-close-packed (ccp) and hexagonal-close-packed (hcp) which is the stable bulk form of Ru (Bovin *et al* 1988). The term 'quasimelting' has been used to describe the structural fluctuations which have been reported for Au clusters supported on pillars of MgO (Ajayan and Marks 1988). Diffusion bonding between ZnO nanocrystallites was recorded at atomic resolution using TV video recording (Kizuka and Tanaka 1994).

4.5.3. Solid state phase transformations. Structural modifications at defects have often resulted from irradiation by the electron beam. Examples of early high-resolution studies include changes in intrinsic/extrinsic stacking faults in CdTe and ZnSe (Sinclair *et al* 1982), the migration of Au grain boundaries (Ichinose and Ishida 1989), and the coalescence of Au nanoparticles (Flueli *et al* 1988). The atomic structure of the (211) solid-liquid interface between crystalline Pd₃Si and amorphous Pd₈₀Si₂₀ has more recently been investigated (Howe 1996), and the migration of a $\Sigma = 5$ [001] GB in MgO was analysed (Kizuka *et al* 1997). It is obviously important to establish whether or not such changes are typical of bulk behaviour. Hence, *in situ* high-resolution studies using custom-designed specimen heating holders will continue to play a valuable role in quantifying interfacial dynamics and solid-state phase transformations (Sinclair *et al* 1988, Howe *et al* 1994, Boyes *et al* 1996).

5. Current and future trends

5.1. Image viewing, recording and processing

The process of image viewing or recording should not in principle impair the ultimate resolution attained by the HREM but in practice there can be a marked negative impact on the overall operating efficiency unless the recording media are properly optimized for the prevailing imaging conditions. Ideally, every incident electron should be detected but readout noise and shot noise may combine to lower the recording efficiency. In the case of beam-sensitive specimens, the total electron dose must be minimized but most electron detectors are typically not very effective at low exposure rates. Despite these and other often conflicting requirements, quantitative measures of performance, briefly described below, are well established (see, for example, Herrmann and Krahel 1984) and figures of merit are readily available for most detection systems.

The phosphor-coated fluorescent screen has historically been the medium of choice for image viewing. With greater electron energy, however, image viewing distances must be increased due to the greater thickness of protective lead-glass viewing windows, and phosphor response also drops markedly. Thin screens of high-atomic-number metals such as platinum can compensate somewhat for decreased visibility by improving the electron backscattering yield and hence the image brightness without significant loss of resolution (Valle *et al* 1977, Smith *et al* 1982). Such measures are insufficient under the demanding illumination conditions required for atomic-resolution viewing and recording, so that most microscopists nowadays only utilize the viewing screen at relatively low magnification (e.g. for rapid area location) or for observation of diffraction patterns (e.g. during sample tilting).

Recently, the capabilities of the low-light-level TV camera have evolved to the level where it has effectively supplanted the fluorescent screen for most image viewing. An image pick-up system can be easily attached beneath the viewing chamber of the microscope without detriment to the overall performance, whilst facilitating several necessary microscope operations as well as permitting real-time image processing (Ponce and Hikashi 1992). Gain adjustment aided by recursive filtering permits high brightness

images to be obtained even under low exposure conditions. The enlarged specimen detail that is easily visible on a TV monitor permits image focusing and rapid astigmatism correction, dynamic events within the sample can be viewed and recorded at TV rates (see section 4.5), and computer control of several key functions becomes possible (Saxton *et al* 1983, Downing *et al* 1992). Nevertheless, high dark current and amplifier noise limit the dynamic range, the linearity of input versus output signals is poor, and in terms of resolvable picture elements the field of view is somewhat restricted. In its present form, the intensified TV camera is thus seriously inadequate for quantitative work. It remains uncertain whether the latest generation of high-definition TV cameras may overcome some of these limitations (Downing *et al* 1992).

In order to provide a useful comparison between the photographic plate, the slow-scan CCD camera and the imaging plate (described further below), meaningful criteria or figures of merit are required. The most important are normally considered (Herrmann and Krah1 1984) to be the detection quantum efficiency (DQE) which measures the efficiency of signal output for each incident electron, the modulation transfer function (MTF) which compares the relative strengths of input to output signal as a function of spatial frequency with the dynamic range R which indicates the maximum number of distinct output signals or 'grey levels'. Other relevant properties of interest include the size of each picture element or 'pixel' (which will pre-determine the minimum practical magnification for particular applications), the total array size (which will determine the dimensions of the recorded field of view), and the linearity (which will influence the ease of comparing intensity levels quantitatively). Further practical considerations include cost, convenience of use, and whether the stored data is readily accessible for image processing. Finally, note the basic requirement that each pixel should be no larger than half the spatial resolution (Nyquist limit), or else the image will be undersampled.

Under typical exposure and development conditions, the photographic plate has a very large number of picture elements (perhaps 5000×5000 or more) and a DQE of about 0.6. The sensitivity can be increased for low doses by using different emulsions and special developing conditions (Kuo and Glaeser 1975) but at the expense of the dynamic range. The grain size is small, of the order of $1 \mu\text{m}$, but several grains are typically exposed by each incident electron so that the effective pixel size is perhaps $10\text{--}30 \mu\text{m}$ (Downing and Grano 1982). The normal drop in DQE observed at higher electron energies can be compensated by using thicker emulsions (Dorignac *et al* 1976) which may, however, adversely affect the MTF. The time required for processing is regarded by some people as a major practical drawback of photographic film, but this should be weighed against its very low cost and immense storage capacity. Finally, its greatest disadvantage for quantitative studies is its notorious lack of linearity for incident intensities over a wide range, which can necessitate an additional time-consuming step in the subsequent image analysis procedure (King and Campbell 1994). At moderate exposure levels, subtraction of the background density should yield a linear relationship between optical density and the electron exposure (Zeitler 1992).

The advent of the slow-scan CCD camera has led to a revolution across the entire field of electron microscopy, with particular impact in the sphere of quantitative image recording. The potential of the CCD camera had long been recognized (Herrmann *et al* 1976, Herrmann and Krah1 1984, Spence and Zuo 1988), in particular its sensitivity, wide dynamic range and efficacy for digital processing. In recent years, much work has been done to characterize these detection properties in quantitative terms (Daberkow *et al* 1991, Kujawa and Krah1 1992, de Ruijter and Weiss 1992, Ishizuka 1993), with a view towards optimizing its usefulness for the electron microscopist (Krivanek and Mooney 1993). The early models used for imaging were based on pixel arrays of 512×512 (Kujawa and

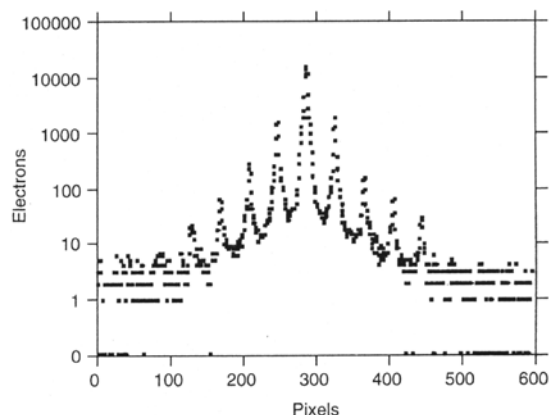


Figure 16. Line scan through an electron diffraction pattern (on a logarithmic scale) from Si[110] crystal, recorded digitally with a slow-scan CCD camera and demonstrating a large dynamic range (from de Ruijter and Weiss 1992).

Krahl 1992) or 1024×1024 (Daberkow *et al* 1991), with the input light signals originating from single-crystal yttrium–alumina–garnet (YAG) or phosphor scintillators with fibre-optic coupling to the CCD detector. Cooling of the detector arrays is necessary to reduce the background noise or dark current level (Daberkow *et al* 1991), while gain variation across the field of view can be effectively eliminated by correction with a gain reference image acquired previously in the absence of the specimen (Ishizuka 1993). With optimal settings and typical incident intensities, a dynamic range in excess of 10^4 and a DQE close to 1 can reasonably be expected (de Ruijter and Weiss 1992). Figure 16 demonstrates the use of a CCD camera for recording a Si [110] electron diffraction pattern. Unfortunately, the image readout speed must be limited in order to reduce readout noise (Kujawa and Krahl 1992) so dynamic viewing at TV rates seems unlikely to be achieved unless image quality is sacrificed. A useful table comparing the major properties of the slow-scan CCD camera with those of the intensified TV camera and the photographic plate can be found in de Ruijter and Weiss (1992), and a comprehensive overview of CCD cameras, detection parameters and characterization methods has recently been published by de Ruijter (1995). Finally, two additional benefits of the CCD camera warrant mention here. In extracting quantitative phase information during off-axis electron holography, the fixed location of the CCD camera enabled geometric distortions of the imaging system to be accurately compensated (de Ruijter and Weiss 1993). Second, online acquisition of a digital signal lends itself to one variant of automated microscope control or ‘autotuning’, as discussed in the following section (Krivanek and Mooney 1993).

Although well established as a recording material in x-ray radiography, the so-called imaging plate (IP) is a relative newcomer to the field of electron microscopy (Mori *et al* 1988). Its principle of operation is as follows. The IP consists of an embedded layer (thickness $\sim 140 \mu\text{m}$) of photo-excitable phosphor grains (typical size $\sim 5 \mu\text{m}$) which have the valuable property that they can store the energy of the incident irradiation (either x-rays or electrons). Photostimulated luminescence is then activated with a scanning laser in a separate processing system, which includes a photomultiplier to convert the output light into an electronic signal suitable for processing and storage. The stored ‘image’ can then be erased and the IP is reusable. Note, however, that the intensity of the stored intensity decays with the time elapsed subsequent to exposure (Isoda *et al* 1992). Careful measurements

(Mori *et al* 1988, Isoda *et al* 1991, Isoda *et al* 1992) have established that the output of the IP provides excellent linearity over a wide dynamic range of about four orders of magnitude, and it has a sensitivity that is voltage dependent but typically about three times greater than that of conventional electron microscope film. The MTF depends most strongly on electron dose, rather than electron energy, and drops sharply at very low dose levels (Isoda *et al* 1992). The IP thus has intrinsically poor resolution in the low-dose regime relative to normal film so that it is not recommended for studies of beam-sensitive specimens (Isoda *et al* 1991). Local experience (Zuo *et al* 1996) suggests that the most fruitful application of the IP is likely to be in the area of quantitative recording of diffraction pattern intensities.

In the era of digital recording and powerful microcomputers, image processing is widespread throughout the field of electron microscopy; for those actively involved in HREM, it is encountered and often utilized on a daily basis (e.g. Coene *et al* 1988, Ponce and Hikashi 1992). The motivation is, of course, to extract the maximum possible useful data from the recorded images. It is thus helpful, though not essential since photonegatives can be digitized using spot microdensitometers or CCDs, that most images are already stored in digital format. The applications of image processing are many and varied, and extend far beyond the focus of this article. Further details can be found elsewhere (Frank 1973b, Saxton 1978, Misell 1978). Some that are more relevant in the present context include: (i) calculations of power spectra (Fourier transform) either to establish the imaging conditions (diffractogram analysis) or to determine lattice spacings (de Ruijter *et al* 1995); (ii) image simulations, especially for comparisons with experimental micrographs to determine correct structural defect models (see section 5.4); (iii) reconstruction of the complex exit-surface wavefunction via off-axis electron holography or through focal-series restoration (see section 5.5); and (iv) pattern recognition algorithms, especially for extracting chemical composition profiles (see section 5.6). Software packages such as SEMPER (Saxton *et al* 1979), SPIDER (Frank *et al* 1981) and CRISP (Hövmöller 1990) are available commercially to handle such routine tasks as Fourier filtering, background correction and cross-correlation averaging. However, for the applications labelled (ii), (iii) and (iv) above, dedicated software is necessary. Computer processing is, of course, central to online microscope control, as described in the following section.

5.2. On-line microscope control—‘autotuning’

As resolution limits improve, it becomes progressively more difficult to select focus, to adjust the objective lens astigmatism and to align the incident beam direction with the objective lens optic axis (coma-free alignment) with the precisions that are necessary to ensure that spurious image detail does not compromise the subsequent image interpretation. Accordingly, since early tests suggested that even skilled microscope operators had difficulty in routinely achieving the desired adjustment tolerances (Saxton *et al* 1983), attention has been directed towards online computer control or ‘autotuning’ of the microscope (Erasmus and Smith 1982, Saxton *et al* 1983, Smith *et al* 1987b, Koster *et al* 1987, Koster and de Ruijter 1992, Ponce and Hikashi 1992, Krivanek and Fan 1992, Krivanek and Mooney 1993). The desired end-result, which is guaranteed, high-quality micrographs on a routine basis, would leave the scientist free to concentrate on solving the particular materials problem at hand.

Before considering the rationale and implementation of the various options for autotuning, it would seem worthwhile to reiterate the sensitivity of the high-resolution image to these important microscope parameters. For example, the Fourier period for a 0.20 nm lattice spacing at 400 keV is 48 nm, and the half-period is 24 nm, so that the

optimum focus probably needs to be chosen to an accuracy of 6 nm or less ($\pi/4$ phase change). This value is close to the level of focus setting and astigmatism adjustment that is achievable by the unaided operator, and, of course, the situation gets progressively much worse at higher resolution due to the squared dependence on the lattice spacing. The importance of coma-free alignment of the incident illumination (Zemlin *et al* 1978, Smith, Saxton *et al* 1983) still remains poorly appreciated by many microscopists. The basic problem is that small misalignments ($\sim 1\text{--}2$ mrad), which are virtually undetectable in optical diffractograms from amorphous materials, cause asymmetrical phase shifts that in turn result in lateral displacements of image information. Figure 17 illustrates the image sensitivity to beam misalignment for a large-unit-cell material, in this case, the inorganic block oxide $\text{Ti}_2\text{Nb}_{10}\text{O}_{29}$. For all three cases shown, artefactual image details starts to appear with a beam tilt of 0.5 mrad, and there is increasing loss of image symmetry relative to the axial case. For comparison, convergence angles of the incident illumination required for high-resolution imaging are typically of this order. Possible approaches to adjusting beam misalignment have been discussed elsewhere (Smith *et al* 1983b).

Several criteria have been proposed as a basis for autotuning (Smith *et al* 1987b). These include: (i) texture recognition; (ii) optical diffractograms (both axial and tilted illumination); (iii) auto-correlation function; (iv) beam-tilt-induced image displacement (BID method); and (v) contrast analysis for amorphous materials. All of these methods rely upon signals which are acquired either from an intensified TV camera or a slow-scan CCD camera, and then fed into a computer, which analyses the data and makes appropriate online adjustments to the microscope controls. The last method, namely contrast analysis, which was the first to be implemented successfully (Saxton *et al* 1983), locates a global minimum of the image variance as the computer successively iterates through the focus, beam tilt (in two orthogonal directions) and two objective lens stigmator controls. Using reproducibility as a criterion for accuracy in the absence of a viable alternative, the rms alignment accuracy was estimated to be 0.126 mrad and the rms astigmatism was 6.3 nm. Comparable values were later obtained using the same basic method at another institution (Smith *et al* 1987b). With the improved data collection, handling and computational facilities nowadays available, significant improvements in terms of expended time and adjustment accuracy should be possible. Meanwhile, as the image variance method is inefficient in terms of dose (typically needing 20 or more images for each parameter adjusted), and inapplicable in the absence of amorphous material, other methods for autotuning have since been explored in more detail.

Beam-tilt-induced displacement was originally proposed (Le Poole 1947) as a means to adjust defocus manually, but subsequent analysis (Koster *et al* 1989) and experimentation (Koster and de Ruijter 1992, Krivanek and Fan 1992) has shown that astigmatism correction and beam-tilt alignment can also be achieved under computer control. Two BID variants for autotuning were initially proposed (Koster *et al* 1989): one using amplitude contrast applicable at low magnification, the other using phase contrast and applicable at high magnification. Both methods are based on calculations of cross-correlation coefficients between pairs or sets of images, and they are thus ultimately limited by the accuracy with which the relative image displacements can be measured. Both methods require that the objective lens defocus should be suitably chosen to avoid low image contrast. Initial experiments with several computer systems in two laboratories led to some differences in the results achieved, primarily in the time taken to complete the autotuning process. The most significant results of relevance here are that, at a magnification of 500 000 times which is in the typical range used for high-resolution imaging, coma-free alignment was reported to be reproducible to 0.1 mrad, and astigmatism correction and focus selection to within 3 nm (Koster and de Ruijter 1992). Although the BID method was found to be very precise

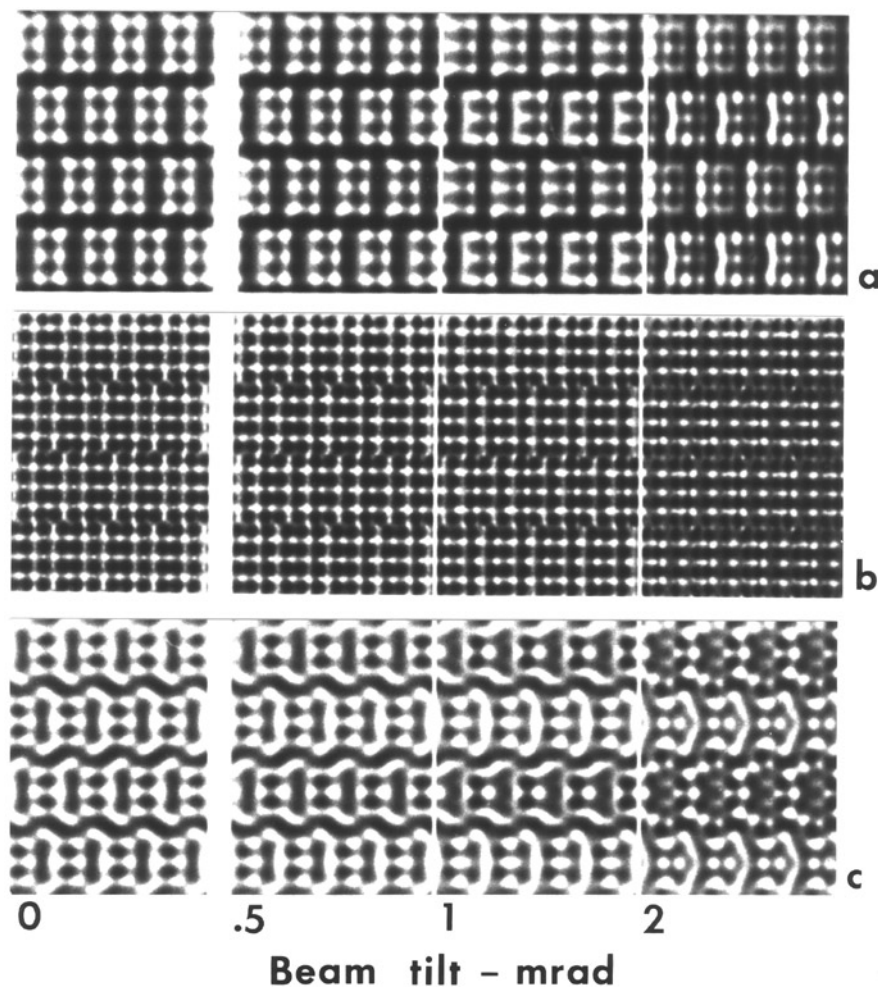


Figure 17. Image simulations for crystal of (010) $\text{Ti}_2\text{Nb}_{10}\text{O}_{29}$ showing the deleterious effect of incident beam misalignment: (a) 100 kV, $C_s = 1.8$ mm, thickness 2.6 nm; (b) 500 kV, $C_s = 3.5$ mm, thickness 2.6 nm; (c) 100 kV, $C_s = 1.8$ mm, thickness 7.6 nm. Beam tilt from left to right of 0, 0.5, 1.0 and 2.0 mrad.

at locating defocus at low magnification (Koster *et al* 1987), it has yet to be established unequivocally whether the method can be successfully implemented at high magnification for crystalline materials. It has been suggested, however, that specimen and defocus drift, as well as considerable changes in image appearance with beam tilt, are then likely to limit its accuracy (Krivanek and Fan 1992).

The latest variant of autotuning to be implemented (Krivanek and Fan 1992, Krivanek and Mooney 1993), and the one that appears most likely to succeed in terms of requiring minimal operator intervention and yet achieving maximal accuracy in parameter adjustment, is based on automated diffractogram analysis (ADA). The ADA method utilizes diffractograms computed from slow-scan CCD images of amorphous material (one is sufficient for autofocus and autostigmatism, three are needed for full coma-free autoalignment). It is a technique that works at high magnification, but it is again inapplicable

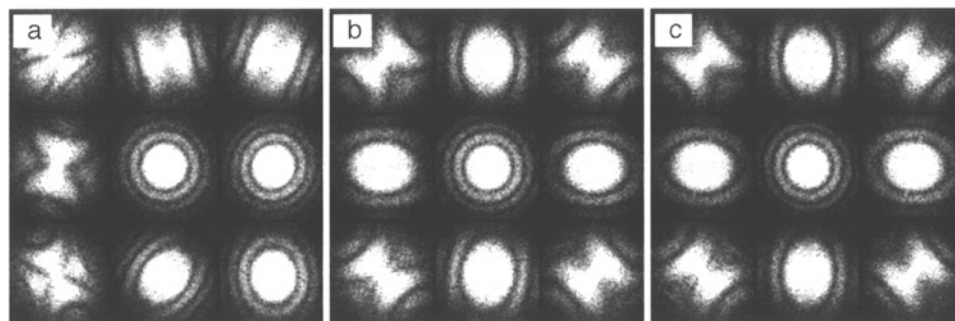


Figure 18. Diffractogram tableau from thin amorphous film recorded (a) before, and (b) after one and (c) two cycles, of autoalignment procedure. Initial mistilt of 4 mrad (a) was reduced to 0.4 mrad (b) and <0.1 mrad (c) (from Krivanek and Mooney 1993).

in the absence of some amorphous specimen region. The diffractograms are first broken up into segments and then the profile of each segment is compared by cross-correlation with a set of theoretical diffractogram profiles (Krivanek and Fan 1992). Finally, the required corrections are applied to the microscope assuming that prior calibration of the computer-controlled parameters has already been done. The set of diffractograms in figure 18 are recorded (a) before, (b) after one and (c) two passes of the autotuning procedure, illustrate the successive improvements obtained with a TEM operating at 120 keV (Krivanek and Mooney 1993). From an initial misalignment of about 4 mrad, the off-axis tilt was reduced successively to 0.4 mrad, and then to less than 0.1 mrad (beyond the adjustment/detection limit of the available instrumentation). Concurrent astigmatism and focus correction to within 1 nm was also achieved. These results are impressive, and they augur well for the impact that autotuning should have in the field of high-resolution electron microscopy.

5.3. Third-order aberrations—detection and correction

All electron lenses suffer from performance-limiting aberrations that should either be corrected during operation whenever possible, or at least quantified and then taken into account during subsequent image interpretation. Two-fold astigmatism and third-order coma were briefly mentioned in the previous section on autotuning: discussion here will concentrate more on progress in detection and correction of spherical and chromatic aberration, as well as three-fold astigmatism which has become increasingly more intrusive as microscope resolution has been extended towards the 0.1 nm level (Krivanek and Leber 1993, Ishizuka 1994, Krivanek 1994, Saxton 1995a, Krivanek and Stadelmann 1995).

The spherical aberration of the objective lens has a pervasive influence on all aspects of electron microscopy. In addition to providing the fundamental resolution limit, as described by equation (5), it also impacts image interpretation due to its effect on the transfer function. Unfortunately, it is well established that spherical (and chromatic) aberration of rotationally symmetric electron lenses remains unavoidable (Scherzer 1936, Rose 1994), although there are, in principle, several possibilities for correction (Scherzer 1947). Since scaling down the dimensions of the objective lens pole-pieces as a means to reduce the C_s value would severely limit the space available for specimen manipulation (and with marginal gain given the $\frac{1}{4}$ power dependence), elimination of C_s (and C_c) by a suitable combination of additional multipole elements has attracted much attention over the years (for a review of early work, see Koops 1978). All previous attempts to correct spherical aberration have met

with failure, due primarily to insufficient electrical stability or lack of alignment precision (Rose 1994), but the latest work (Haider and Zach 1995) appears to be on the brink of success. A C_s -corrector attached to a 200 keV FEG-TEM has enabled the normal 0.23 nm interpretable resolution limit of the instrument to be surpassed, with a level of ~ 0.17 nm recently being achieved (Haider, private communication). It still remains to be established whether extraneous environmental effects or inherent temporal coherence (focal spread) will ultimately prove to be performance-limiting.

A detailed knowledge of the chromatic aberration coefficient of the objective lens, for example its absolute value or its dependence on the current setting, is not usually considered to be important for high-resolution imaging. C_c does not affect the interpretable resolution, and the temporal coherence envelope is determined by an effective focal spread, which is normally estimated empirically from diffractogram analysis (Frank 1976, Saxton 1977) or by detailed comparisons with image simulations (Wilson *et al* 1982). Nevertheless, inasmuch as the magnitude of C_c directly impacts the temporal coherence, which is certainly performance-limiting for an LaB₆ electron source, then reduction or correction of chromatic aberration would be beneficial and should be pursued. Correction of C_c in a low-voltage scanning electron microscope was recently achieved (Haider and Zach 1995) but no success in the voltage range of interest for HREM (upward from about 100 kV) has yet been reported. An alternative solution to reducing chromatic effects would be to locate a monochromator immediately following the electron gun, which could possibly reduce the energy spread to about 0.1 eV (Rose 1990), and also to employ an imaging energy filter as a post-specimen monochromator (Rose 1994).

Meanwhile, in order to utilize any information that is transferred by the objective lens beyond the interpretable resolution limit, it is necessary to deconvolute the oscillatory effect of the transfer function, which implies that an accurate knowledge of the actual C_s value needed (Koster and de Jong 1991). Simple calculations based on pole-piece dimensions are inadequate once the material goes into saturation. Programs are available that take saturation into account (e.g. Munro 1988) but, because of the sensitivity to specimen height, it is usually preferable (Budinger and Glaeser 1976, Smith 1989b) to measure the C_s value experimentally at the desired objective lens current. Measurements of optical diffractograms (Krivanek 1976), or the displacement of small-particle reflex images (Heinemann 1971, Budinger and Glaeser 1976), typically yield measurement errors of 3–5%, which has been sufficient for most purposes until quite recently. Statistical analysis of diffractogram rings (Coene and Denteneer 1991) and cross-correlation analysis of beam-tilt-induced image displacement (Koster and de Jong 1991) have been reported to give measurement precisions of better than 1%, but the real accuracy was limited by systematic errors, including calibration of image magnification and beam-tilt controls. The specimen should always be kept as thin as possible since the positions of the maxima of the diffractogram are likely to be shifted, leading to an error in the C_s estimation (Gibson 1994). In order to achieve $\pi/3$ error in reconstruction of the TF at the 0.10 nm level for typical 200–300 keV HREMs, which some people might consider insufficient, the accuracies required are calculated to be in the range of 0.2–0.7% (de Jong and Koster 1992). For holographic reconstruction to achieve a resolution limit of 0.10 nm, an even smaller error in C_s approaching 0.1% is required (Lichte 1991): deterministic parameter fitting during the reconstruction process seems to be the only option currently available to achieve this level of accuracy.

Three-fold astigmatism was observed and quantified during the first serious study of coma-free alignment (Zemlin *et al* 1978). However, it was only during the implementation of the ADA method for autotuning that the disturbing implications of three-fold astigmatism for high-resolution imaging at the 0.10 nm level first came to be appreciated

(Krivanek and Lieber 1993, Krivanek 1994). Like coma, three-fold astigmatism is effectively invisible in an axial bright-field image or the corresponding diffractogram since its basic effect is an asymmetrical shift of phase information. Nevertheless, as shown by recent image simulations (Krivanek and Stadelmann 1995, Saxton 1995a), the effects on very-high-resolution images of crystalline materials can be more or less pronounced, being especially dependent on the relative orientations of the three-fold astigmatism and any crystal symmetry directions. The effects of three-fold astigmatism continue to be actively explored in several laboratories so that its full ramifications have yet to be established. The following represents a brief summary: (1) the effect of three-fold astigmatism is greatest for pole-pieces with small C_s and large values for the three-fold astigmatism coefficient (Krivanek and Stadelmann 1995); (2) the magnitude of three-fold astigmatism can be reasonably estimated using diffractograms from a minimum of four images recorded with mutually orthogonal beam-tilt directions (Krivanek 1994, Saxton 1995a); (3) three-fold astigmatism values typically lie in the range of 0.4–2.0 μm , and seem to be relatively constant over a period of months for a given microscope (Krivanek and Stadelmann 1995, Overwijk *et al* 1997); (4) correction of three-fold astigmatism is, in principle, possible using a pair of sextupole stigmator coils located near the back focal plane of the objective lens: reasonable adjustment can apparently be made by applying fixed correction currents to the existing objective stigmator coils provided that they are energized separately rather than being wired in pairs which is normally the case (Overwijk *et al* 1997); (5) coma-free alignment is still possible even in the presence of substantial three-fold astigmatism (Ishizuka 1994, Krivanek 1994). The interested reader is referred to the cited references for more detailed information.

5.4. Progress towards quantitative structure analysis

One of the major attractions of the high-resolution electron microscopy technique is the possibility, as demonstrated by many of the examples already described in section 4, that the atomic arrangements at local irregularities such as dislocations and interfaces can be determined to a very high degree of accuracy, in some cases approaching 0.01 nm. Useful feedback for atomistic defect modelling calculations, for example, can then be obtained. Nevertheless, it should be recognized that the refinement process has invariably been heavily demanding of the microscopist and the instrument, as well as being computing-intensive and often extremely time consuming. Commitment of adequate resources is required to remove much of the trial-and-error parameter fitting and to move closer towards the ultimate goal of real-time, interactive structure refinement. This section on quantitative structure analysis is restricted to aperiodic structural features for which the results of recent work (Möbus and Rühle 1994) imply that this goal is unlikely to be attained because some parameters can only be optimized iteratively (although it may be possible to automate the iteration process considerably (Möbus and Necker 1997)): approaches applicable to periodic structures are considered in section 5.8.

Prior knowledge (or elimination) of essential experimental parameters would clearly facilitate the process of approaching the goal of interactive structure refinement. For example, it should be possible with many materials to generate a thickness-focus tableau of perfect crystal images in advance of the microscopy session to enable rapid fitting of defocus and specimen thickness using cross correlation (Thust and Urban 1992). The operating magnification is somewhat immaterial since it should be straightforward to map an experimental image onto the results of any simulations with reasonable accuracy. (It is assumed, of course, that the user has separately established an objective method for determining the best agreement between the two.) Likely errors in wavelength calibration

using, for example, convergent beam electron diffraction are below the threshold level for having a detectable effect on high-resolution images. Correction of the three-fold astigmatism, possibly at the time of microscope installation, should reduce its effect to the level where it too has negligible influence on the image. Routine application of autotuning would undoubtedly also be of great assistance since two-fold astigmatism (two parameters) and coma/beam tilt (two more parameters) would be removed from consideration. Autotuning implies, of course, the availability of an online CCD camera as well as computer access to the coil currents. Contrast evaluation based on photographic negatives undoubtedly permits highly accurate structure refinement (Möbus and Rühle 1994) but direct digital CCD recording should still greatly expedite the process of data extraction and quantitative analysis.

Historically, the determination of defect structures relied upon qualitative comparisons between experimental micrographs and image simulations that were based on various alternative structural models. A sizeable but non-exhaustive list of examples has been tabulated in Smith *et al* (1993) and further examples were noted earlier in section 4. The acceptability of a specific structural model was generally considered as being enhanced when an image 'match' was achieved for multiple members of a focal series (see, for example, Cherns *et al* 1982, Barry 1991, Campbell *et al* 1993a). Two such micrographs of an inversion domain boundary in aluminium nitride are shown in figure 19, with corresponding image simulations inset (McCartney *et al* 1992). In several structural studies (see, for example, Bourret *et al* 1988b, Buckett *et al* 1993), an alternative approach has been to overlay projected atomic column positions on the experimental and/or simulated images, demonstrating in some cases that serious positioning errors could easily have arisen from direct visual image interpretation (i.e. the positions of intensity maxima or minima in the electron micrographs did not necessarily correspond to the atomic column locations). Other studies have utilized superposition (e.g. Penisson *et al* 1988) or subtraction (e.g. Hoche *et al* 1993) of matching pairs of simulated and experimental images during the refinement process. In one case, iteration between simulated and experimental images using a least-squares refinement method led to improved accuracy in the structure refinement (Banfield *et al* 1991). A nonlinear least-squares optimization approach that compared experimental and simulated grain boundary images (King and Lamver 1991) was successfully used to refine atomic positions at Nb GBs.

Recently much more attention has been paid to the issue of quantifying the 'goodness of fit' between the experimental micrographs and the corresponding simulated images derived from postulated structural model(s). Unlike the case for x-ray or neutron diffraction studies where reliability or *R*-factors refer to the contents of the entire unit cell, for the structure determination of defects such as grain boundaries or dislocation cores such well defined entities do not generally exist. Several parameters originally proposed for consideration (Smith and Eyring 1982) proved to be defocus-dependent and were thus unsatisfactory for practical use. The so-called 'normalized Euclidean distance' (NED) has recently been utilized (Hofmann and Ernst 1994b) as an alternative criterion for quantifying the residual discrepancies between simulated and experimental defect images. Because it is normalized and defined in terms of intensity differences, the NED has the practical advantage of being independent of size and intensity scaling of the images. However, it refers to image rather than structural discrepancies and some additional analysis is required in order to arrive at estimates for the mean error in column positions and errors in the individual column positions. Moreover, it was also pointed out that other discrepancies could arise as a result of a non-structural difference, such as approximations made in the image simulation programs. Further image agreement factors (IAFs) have been proposed and utilized at various times:

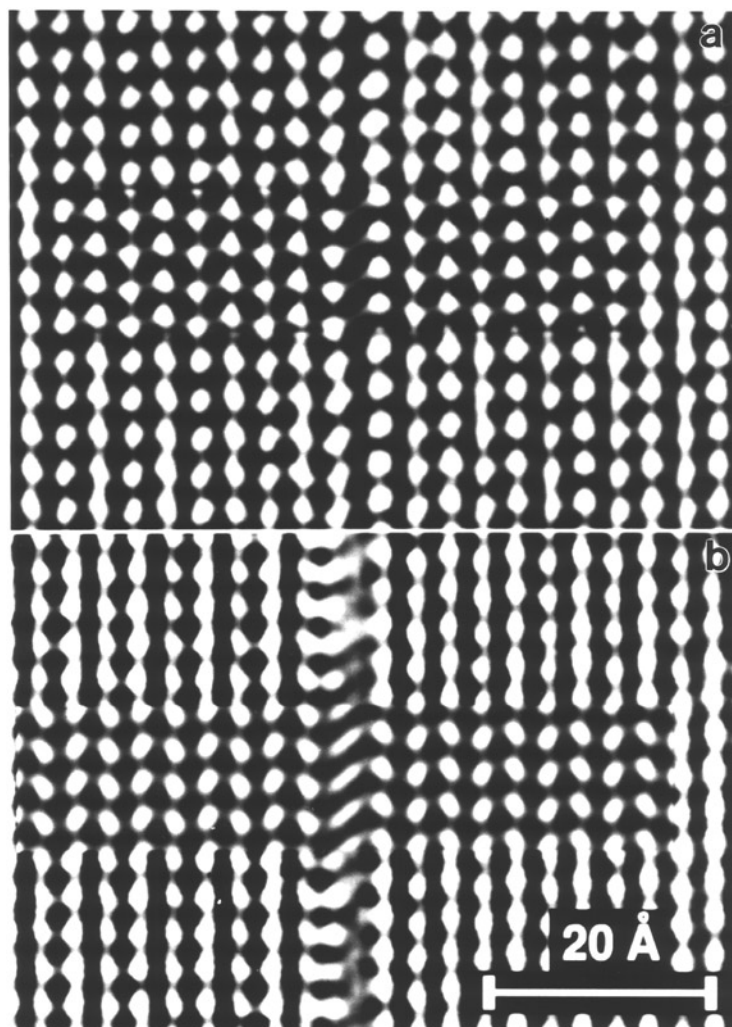


Figure 19. Experimental high-resolution electron micrographs of an oxygen-containing inversion domain boundary in AlN, recorded at 400 keV with JEM-4000EX: (a) inset simulated for 3.1 nm thickness and -45 nm defocus; (b) inset simulated for 5.3 nm thickness and -72 nm defocus (from McCartney *et al* 1992).

a useful summary of those most commonly used can be found as an appendix in Möbus and Rühle (1994). In the same study, it was disturbing that the atomic coordinates for an Nb/sapphire GB differed by as much as 0.04 nm depending on which IAF was used: the suggested cause for the discrepancy was that different IAFs weighted bright and dark image areas differently. Nevertheless, these differences raise again the fundamental issues of quantifying the reliability and accuracy of any structure refinement. In our opinion (Smith *et al* 1993), it would be helpful to remove defocus and other microscope parameters from the actual refinement process by using the complex exit-surface wavefunction of the specimen as the reference plane for comparison between simulation and experiment. At that stage, a χ^2 goodness-of-fit criterion (King and Campbell 1994) would be an appropriate test of overall convergence, while error bars could be placed on the locations of individual atomic columns using a criterion such as NED to minimize residual discrepancy.

As more attention has been given to quantitative structure analysis, it has become increasingly obvious that there are substantial, seemingly inexplicable, disagreements between experimental and simulated image contrast levels as well as diffracted beam intensities (Hýtch and Stobbs 1994, Walther *et al* 1995). For example, in a recent detailed analysis of images of GaAs/Al_xGa_{1-x}As quantum wells, it was found (Hýtch and Stobbs 1994) that the image contrast, defined as the standard deviation of intensity across an individual image, typically showed factors of 6–8 difference between simulated and experimental images. In comparison, it appears to be significant that the mean image intensity typically only fell by about 10% over the same thickness range. Consideration of possible sources of error, such as beam misalignment or surface contamination, failed to account for the differences in contrast, while unrealistically thin specimen thicknesses could be dismissed because the thickness had been determined by an independent method. A subsequent study, again of GaAs/Al_xGa_{1-x}As, found (Walther *et al* 1995) that experimental diffracted beam intensities were factors of 2–6 smaller than the calculated values. An unpublished study of cleaved InP wedges, of known cleavage angle and therefore well defined thickness profile, also showed (Phillipp, private communication) serious discrepancies that could not be accounted for by such obvious factors as crystal tilt, surface roughness or contamination overlayers. Given the above behaviour of the mean image intensity reported by Hýtch and Stobbs (1994), it could be a revealing exercise to repeat the above experiments with an imaging energy filter to remove most of the inelastically scattered electrons, while observations with the sample cooled to liquid nitrogen temperatures, or even close to liquid helium temperature, could establish whether atomic vibrations are having a greater than expected effect.

Finally, it is remarked that comparatively little attention has been given to quantitative structure analysis of aperiodic features using multiple projections. The work considered in this section has concentrated almost entirely on two-dimensional projections where it has been presumed that the images of atoms at different heights are not overlapping. This assumption is probably not unreasonable for one-dimensional line defects such as dislocations cores unless they are decorated by impurities but it may not always be justified for two-dimensional heterogeneous interfaces. Moreover, structural rearrangements along other crystal axes may be overlooked, as demonstrated, for example, by the detailed studies of the {211}Σ = 3 GB in Ge where it was discovered that a 2 × 1 two-dimensional GB reconstruction had occurred (Bourret and Bacmann 1985). One reason for the concentration on two-dimensional structures is that intermediate-voltage HREMs do not usually have specimen holders with a sufficient range to permit tilting from one major low-index zone to another. This limitation does not hold for the high-voltage HREMs where larger pole-piece dimensions allow greater flexibility (Gronsky and Thomas 1983). In one significant HVHREM study (Hull *et al* 1986), the interface between GaAs islands nucleated on an Si(001) substrate was imaged in projections ranging from (110) through (010) all the way to ($\bar{1}10$). The structure of ‘point’ defects or small defect clusters should be amenable to study using multiple projections. The problems of image registration have been addressed in three-dimensional tomography studies of biological entities (Dierksen *et al* 1992) and thus should not be a serious problem for materials systems.

5.5. Restoration of the complex exit-surface wavefunction

The primary motivation for wavefunction restoration methods is to deconvolute the oscillatory effects of the TF, thereby extending image interpretability out to the microscope

information limit. However, the final recorded image intensity is lacking in phase information. Thus, an additional benefit of restoration techniques is that, by providing the complex exit-surface wavefunction, phase and amplitude information about scattering by the sample also become available. The removal of the microscope parameters in the restoration process should enhance the possibilities for the determination of unknown defect structures since the wavefunction is now solely a direct representation of scattering by the object, although this advantage does not yet appear to have been utilized by any of the techniques currently being explored. Our attention here is concentrated on three of these methods, namely focus variation (Coene *et al* 1992, 1993), off-axis electron holography (Ishizuka *et al* 1994, Orchowski *et al* 1995), and tilt-series reconstruction (Kirkland *et al* 1993, 1995). These methods have all been used to achieve significant gains in information beyond the interpretable resolution, in some cases approaching close to 0.10 nm, thus demonstrating their viability for atomic-resolution studies and justifying their consideration here.

Focus variation methods for wavefunction reconstruction have attracted the most attention over the years. As originally proposed (Schiske 1968), the object wavefunction would be restored by summing an image set suitably filtered and phase-shifted by the wave-aberration function to account for defocus variation. More sophisticated series-restoration filters were later developed, first with a Wiener filter to account for indeterminate solutions due to a zero denominator (Schiske 1973), and later incorporating coherence envelopes to account for focus spread and illumination divergence (see, for example, Saxton 1978, 1988). Methods suitable for handling dynamical, nonlinear effects have also received attention (Kirkland 1984, Saxton 1988). In the latest version of the method (van Dyck *et al* 1993), it was proposed that a closely and equally spaced focal series of images should be recorded, and then combined after each respective image had been phase-shifted to the same image plane. This method has been called the paraboloid method (PM) because, in its simplest form, it only selects linear imaging contributions which are located on a reflected paraboloid in reciprocal space. In a subsequent development, known as the maximum likelihood method (MAL), nonlinear imaging contributions are taken into account, thus extending the thickness validity range for the reconstruction (Coene *et al* 1996). The lack of novelty and directness of the PM and MAL methods have been strongly questioned (Saxton 1995b). Nevertheless, aided by online computer control of focus, digital recording, and a suitable recursive algorithm, the 0.24 nm point resolution of a 200 keV HREM was extended to better than 0.15 nm. As shown in figure 20, individual oxygen atomic columns in a high-temperature superconductor could then be resolved in projection (Coene *et al* 1992). Successful deconvolution extending to 0.11 nm has since been achieved with a 300 keV instrument (Coene *et al* 1993). Earlier reconstruction methods might equally well have attained comparable success but no significant resolution gains were previously demonstrated, primarily because the microscopes available at the time had inadequate illumination coherence to justify the time and effort.

Recent work has concentrated on measures that enhance the speed and rate of convergence of the PM-MAL calculations, such as steepest gradient analysis and approximations for envelope functions, using a normalized cross-covariance figure of merit for comparison because the experimental amplitudes and phases were considerably weaker than the simulated values (Coene *et al* 1996). The significance of the three-fold astigmatism also became apparent during this work, forcing the development and application of a phase plate or 'fingerprint' of the objective lens aberrations before fully reliable restoration could be achieved out to the available information limit. An example of the phase plate that was measured for a 300 keV FEG-TEM during focal-series reconstruction is shown in figure 21 (Thust *et al* 1996). Approaches to full nonlinear reconstruction of the exit

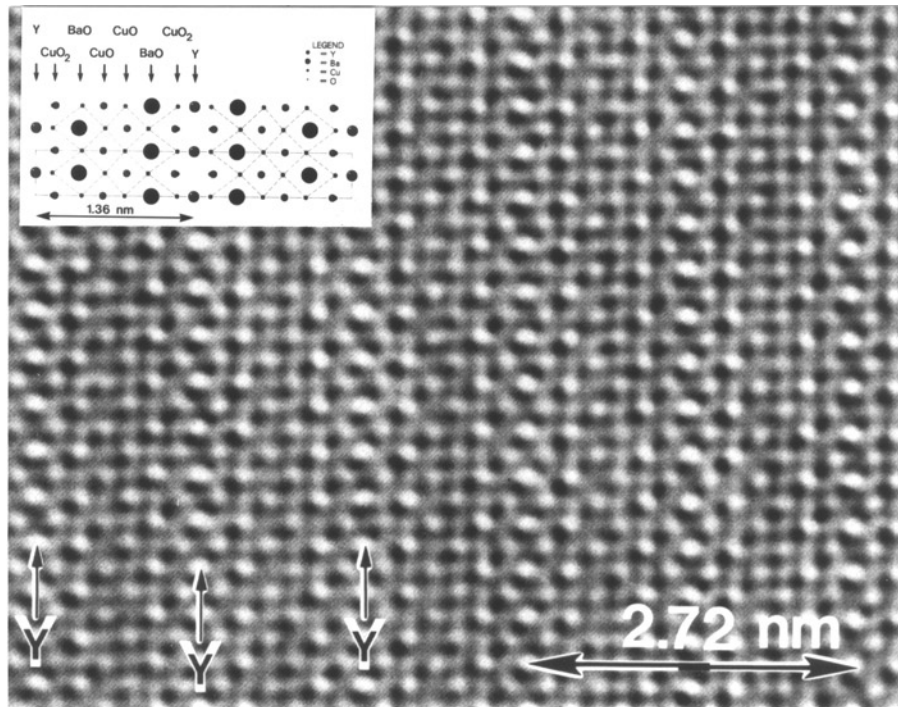


Figure 20. Focal-series reconstruction of [100]-oriented $\text{YBa}_2\text{Cu}_4\text{O}_8$ high-temperature superconductor: the comparison of phase image with structural model (inset) confirms the visibility of individual oxygen atomic columns (from Coene *et al* 1993).

surface wavefunction, based upon simulated annealing and genetic algorithms, appear to be promising alternatives for periodic objects provided that adequate experimental data is acquired (Thust *et al* 1994).

In off-axis electron holography, a positively charged wire, usually located in the selected area aperture plane beneath the sample, causes overlap of the image wave with a reference vacuum wave, leading to the hologram which is a cosinusoidal fringe pattern in the final image plane that has amplitude and phase modulations which reflect the local object structure (Tonomura 1993, Lichte 1991). A high-resolution off-axis electron hologram of a thin Si[110] crystal is shown in figure 22, together with the corresponding Fourier spectrum (Orchowski *et al* 1995). By first applying a Fourier transform to the hologram and then inverse fourier transforming using one of the sidebands (rather than the central autocorrelation peak which represents the normal power spectrum of the high-resolution image), a reconstructed complex image wave containing phase and amplitude information is obtained but modulated by the TF prevailing at the time of recording. An inverse phase plate can then be applied numerically in Fourier space to restore the complex object wavefunction, in principle with a resolution extending to the information limit of the microscope. In practice, in common with the focal-series restoration methods, the integrity of the reconstruction process will be limited by the accuracy with which the inverse phase plate, which must incorporate two- and three-fold astigmatism and axial coma, as well as defocus and spherical aberration, can be determined and thus compensated. Assessment of the required accuracy of these parameters has been carried out using the strong criterion of a $\pi/6$ deviation in the aberration function (Lichte 1992): in practice, a trial-and-error process

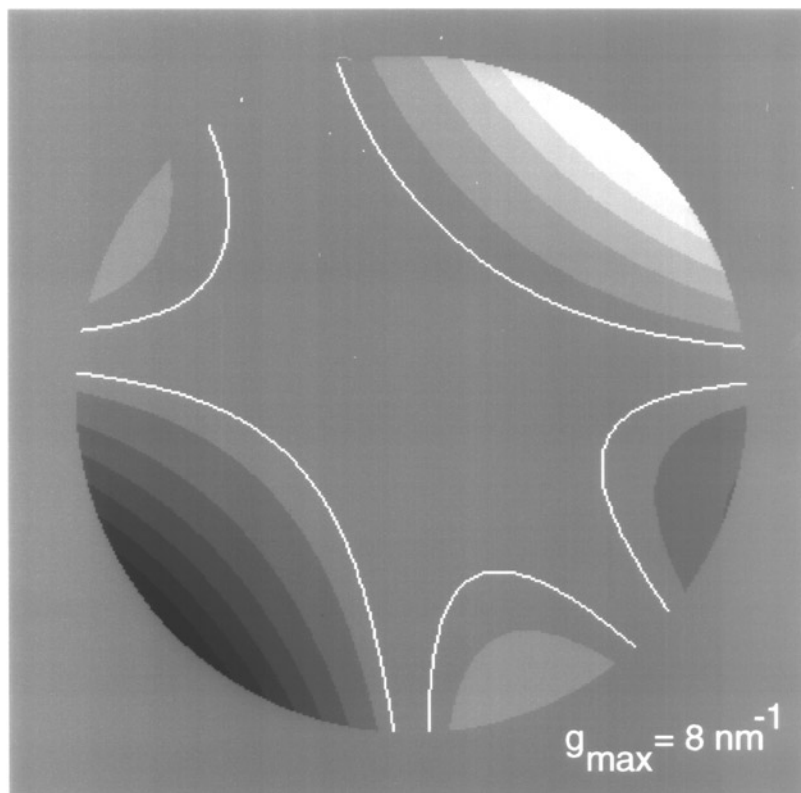


Figure 21. Two-dimensional phase plate or 'fingerprint' showing residual aberrations of 300 kV FEG-TEM as a function of the scattering angle before focal-series reconstruction. Grey levels show $\pi/2$ changes in the aberration function, while white lines mark phase shifts of $\pi/4$ (from Thust *et al* 1996).

is apparently preferred for parameter estimation. Artefacts such as vignetting due to the biprism, Fresnel diffraction at the biprism and asymmetry of the MTF of the CCD camera also need to be recognized (Lichte *et al* 1996). Despite these experimental difficulties, the realization of object wavefunctions well beyond the respective interpretable limits has been recently been reported for 100-, 200- and 300 keV FEG-TEMs (see Harscher *et al* 1995, Ishizuka *et al* 1994, Orchowski *et al* 1995, respectively). Figure 23 shows the amplitude and phase of the reconstructed exit-surface wavefunction for the hologram shown in figure 22: the individual Si atomic dumbbell structure is clearly resolved (Orchowski *et al* 1995). Further consideration of recording requirements, including the pixel size and adequate sampling of the holographic fringes (4 pixels/fringe) suggest that 0.10 nm detail in the restored complex object wavefunction should be attainable with a 300 keV FEG-TEM by using a $2k \times 2k$ CCD array (Lichte 1993).

Reconstruction from a tilt-azimuth series represents an alternative route to improved resolution and image interpretability (Kirkland *et al* 1993, 1995), using an imaging geometry for each member of the series that is effectively identical to that previously used for achromatic recording of lattice fringes (Komoda 1966a). The combination of an image set with rotated tilt azimuths (usually four images rotated by $\pi/2$) permits a larger cross section of spatial frequencies to be sampled without the need for the extra coherence

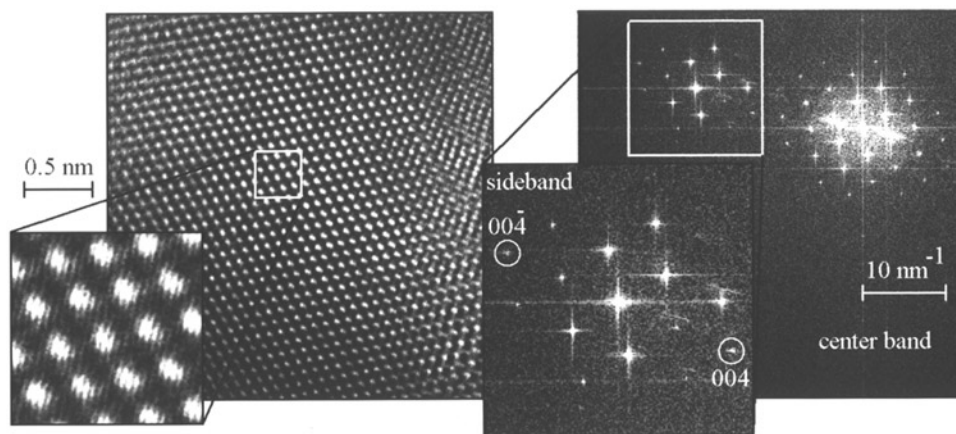


Figure 22. (a) High-resolution off-axis electron hologram plus enlargement from thin Si [110] crystal recorded at 300 keV. Holographic fringe spacing of 0.05 nm. (b) Fourier spectrum from hologram highlighting the sideband used for holographic reconstruction including {004} reflections that correspond to a spacing of 0.136 nm (from Orchowski *et al* 1995).

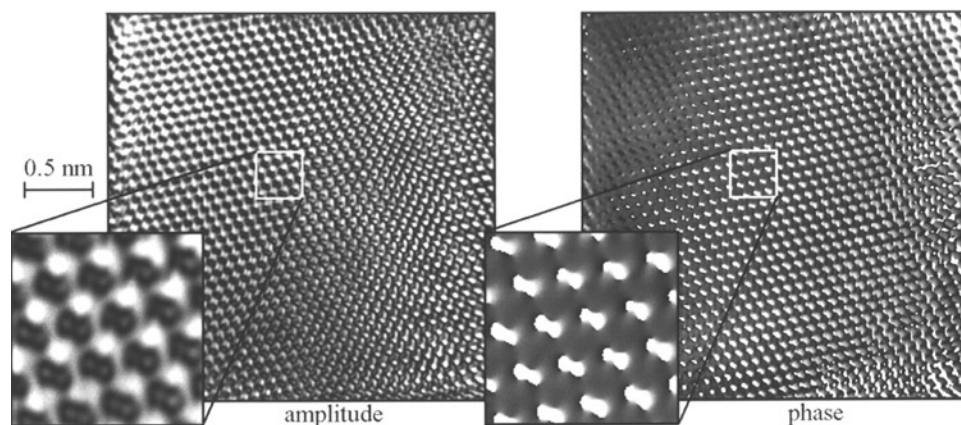


Figure 23. Amplitude (left) and phase (right) of aberration-corrected reconstructed off-axis electron hologram from thin Si [110] crystal. The characteristic Si dumbbell structure is clearly visible in the enlargements of amplitude and phase (from Orchowski *et al* 1995).

afforded by a FEG source. After establishing the imaging conditions for each image, they must be accurately aligned before being combined using a suitable restoring filter (Saxton 1988, 1994). The initial trials of the method used photonegatives, thus prolonging overall beam exposure which caused specimen modification, and accurate alignment of the tilted illumination images was also not as straightforward as for an axial set. Nevertheless, the modulus and phase of a supported gold particle test sample were restored to a resolution limit of better than 0.14 nm compared with an axial point resolution limit of 0.25 nm. The reliability and integrity of the method have since been evaluated using a thin crystal of $\text{H-Nb}_2\text{O}_5$, which has a known structure: the limit of continuous transfer was extended from ~ 0.20 nm in the conventional axial image to ~ 0.13 nm (Kirkland *et al* 1997).

The restoration methods described here all have drawbacks and advantages. Whilst lending themselves to computer control, they are all highly sensitive to the microscope

adjustment (residual beam tilt, two-fold astigmatism and defocus) and other essential parameters (three-fold astigmatism and C_s) must be known with high accuracy. Electron holography requires extremely coherent illumination and the field of view must include the vacuum reference wave but, unlike the PM-MAL or tilt-azimuth series methods, only one exposure is necessary so that image drift and possible beam damage is not such an issue. Conversely, multiple exposures mean less susceptibility to signal-to-noise fluctuations. All three approaches must be considered as indirect methods, given that substantial computation is required before the exit-surface wavefunction is finally restored. PM-MAL (Coene *et al* 1993) and electron holography (Orchowski *et al* 1995) have been used to successfully restore the Si{110} projected atomic structure, the so-called 'dumbbells'; none of the three have yet been applied to solving the structure of an aperiodic defect, although the possibilities have been evaluated using image simulations for PM-MAL (Coene *et al* 1996).

5.6. Chemical imaging

One shortcoming of most atomic-resolution imaging is a lack of compositional sensitivity. In some systems, however, compositional variations, sometimes associated with structural irregularities, can be determined on the basis of variations in the local image contrast. The term 'chemical imaging' was initially applied specifically to lattice-matched structures possessing chemically sensitive reflections: by utilizing appropriate choices of defocus and thickness, and suitable pattern recognition techniques, chemical composition can be determined at near-atomic resolution (Ourmazd *et al* 1989a). Given the right combination of conditions, chemical identification of individual atomic columns can also be achieved for metallic alloys (e.g. Amelinckx *et al* 1985, Penisson *et al* 1991b) and transition metal carbides (Epicier 1990) and oxides (Evans *et al* 1986). A more sophisticated approach has since been developed that allows the variation in projected potential in crystalline solids to be measured with atomic-level precision, again under certain, well defined conditions (Schwander *et al* 1993, Kisielowski *et al* 1995).

The best known and classic example of chemical imaging are the GaAs/ $\text{Al}_x\text{Ga}_{1-x}\text{As}$ heterostructures observed in the [001] direction (Hetherington *et al* 1985, Ourmazd *et al* 1990). The (200) reflection in GaAs is a structure-factor difference reflection with an amplitude that remains very low even for crystal thicknesses in excess of 20 nm, whereas this reflection is comparatively strong, though oscillatory, over a wide range of thicknesses in AlAs (Tanaka *et al* 1987). As shown by the example in figure 24, a highly characteristic contrast motif for {001}-oriented samples enables easy differentiation between the two materials, and regions of interface steps can also be identified. Similar layer recognition is possible using {011}-oriented samples (Ikarashi *et al* 1989) but, because there are only two chemically sensitive (200) reflections in this projection, and nonlinearity with composition in the (111) beam (Thoma and Cerva 1994), local compositional information is unlikely to be extracted without precise knowledge of the imaging conditions (Walther and Gerthsen 1993). Step structures at AlAs/GaAs interfaces have, however, been observed, and an ordered interfacial structure at the Si/Ge interface has been investigated (Ishida 1995).

A vector pattern recognition algorithm has been developed for the [001] projection that enables the local composition to be quantified on the unit-cell scale: single- and double-atom substitution in individual atomic columns at AlAs/GaAs hetero-interfaces can be recognized with confidence levels of 60% and 90% respectively (Ourmazd *et al* 1989b). A similar pattern recognition technique was also applied to interfacial ordering in Ni_3Al intermetallic alloys (Penisson *et al* 1991b) and subsequently to detect the preferential location of substitutional impurity atoms in related material (Penisson 1993). A novel,

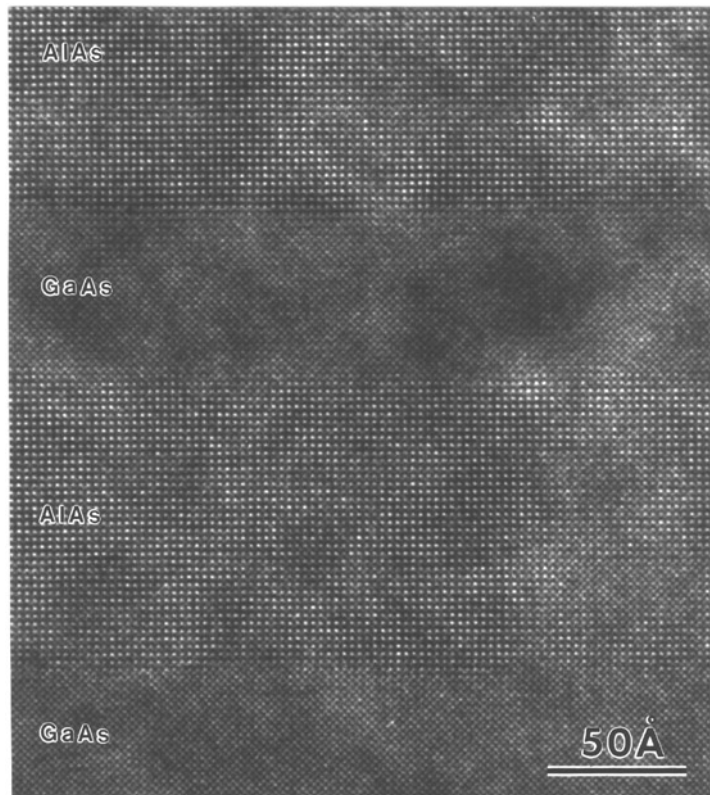


Figure 24. High-resolution electron micrograph of [001]-oriented GaAs/AlAs heterostructure. Note the different contrast motifs of crossed 0.20 nm {220} lattice fringes in GaAs and crossed 0.28 nm 200 lattice fringes in AlAs.

three-step algorithm was developed to study strained Si_mGe_n heterostructures in both [110] and [100] crystal projections (Stenkamp and Jäger 1993). ‘Chemical imaging’ in the sense of structure-factor-difference reflections is no longer applicable but, as demonstrated by the example in figure 25, layer compositions could be established to within $\pm 10\%$ with unit-cell resolution using carefully chosen operating conditions, and sharp hetero-interfaces could be located with monolayer accuracy. Finally, a novel technique has been developed for direct measurement of lattice distortions in strained layer structures in terms of a local displacement vector: it has been proposed that the method could also be an effective way to accomplish chemical mapping (Bierwolf *et al* 1993).

Many binary alloy systems of the general form A_{1-x}B_x make excellent candidates for chemical imaging. They form an intriguing variety of superlattice structures (see, for example, Watanabe and Terasaki 1984), often with ordered linear and planar defects such as antiphase boundaries. Experimental observations and image simulations have again established (Amelinckx *et al* 1985, Terasaki *et al* 1986, Milat *et al* 1992) that the different atomic columns in typical mixed alloys can be distinguished for suitable values of specimen thickness and objective lens defocus, although the sensitivity to partial occupancy does not appear to have been examined. Similar considerations apply to sublattice imaging in a range of transition metal carbides which form planar defects as a result of departures from stoichiometry (Epicier 1990). The structure of the defects can often be deduced

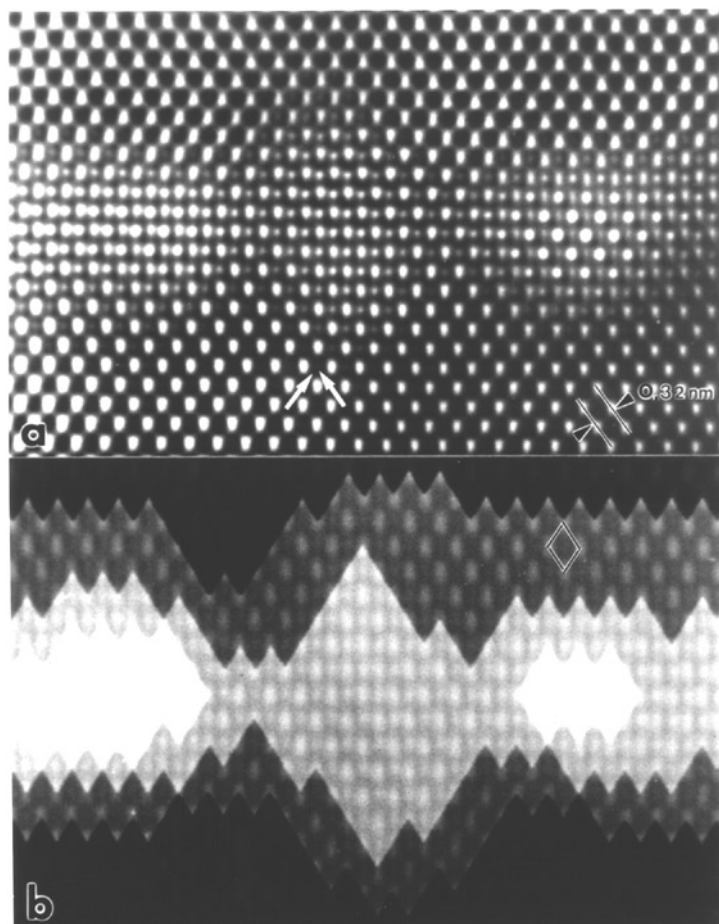


Figure 25. (a) Cross section lattice image of Si_mGe_n strained-layer superlattice; (b) corresponding two-dimensional compositional map using a grey-scale representation (from Stenkamp and Jäger 1993).

simply by reference to the appropriate high-resolution image. Extensive image simulations are, however, highly recommended since the defocus-thickness combinations suitable for chemical imaging are liable to be material specific.

Finally, one should be aware that, because of crystal symmetries, dynamical interactions may sometimes give rise to interference effects which can be misinterpreted in terms of sublattice imaging. Simulated examples for BaTiO_3 (Smith *et al* 1985b) and mullite (Epicier 1990) stress this point.

5.7. Incoherent STEM imaging

According to the reciprocity principle (Cowley 1969), image formation in the scanning and conventional TEMs can be considered as equivalent, at least for thin specimens with elastic scattering, except for reversal of the electron's path through the objective lens. In practice, the serial imaging mode of the STEM allows greater flexibility because it enables several signals to be collected simultaneously, and micro-analysis and nanodiffraction from very

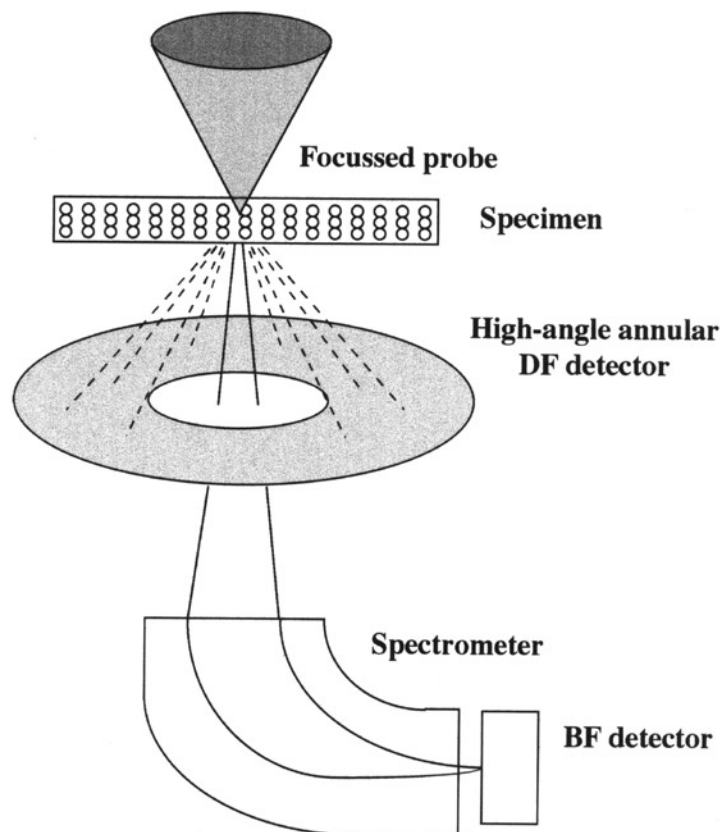


Figure 26. Schematic diagram of high-angle annular-dark-field incoherent STEM imaging with the possibility of concurrent electron-energy-loss spectroscopy and bright-field imaging.

small areas can be achieved simply by stopping the scanned probe. Real-time observations of dynamic events over a wide field of view is not possible although scan speeds of up to ~ 10 periods s^{-1} can be reached for very limited fields. Because of the strong atomic-number dependence of large-angle scattering, dark-field imaging with an annular detector provides high contrast images emphasizing the positions of heavy atoms with 'Z-contrast' (Crewe *et al* 1975). The image resolution for annular DF imaging is in principle improved by a factor of ~ 1.4 relative to BF imaging with the same objective lens (Cowley 1976). By increasing the inner collection angle of the annular dark-field (ADF) detector, image contrast is further enhanced because of the Z^2 -dependence of the large-angle thermal diffuse scattering, despite a significant fall-off in overall intensity and associated poor signal-to-noise ratio (Crewe *et al* 1975). The schematic illustration in figure 26 portrays the formation of the high-angle ADF image in the STEM, with the simultaneous possibility for electron-energy-loss spectroscopy (EELS) and energy-dispersive x-ray spectroscopy. STEM observations (see, for example, Pennycook 1992) and image simulations (e.g. Loane *et al* 1992) indicate that the image contrast for high-angle ADF imaging does not reverse either with objective lens defocus or specimen thickness, and images of oriented crystalline materials can be interpreted intuitively on the basis of simple incoherent imaging (Pennycook and Jesson 1990). Careful analysis shows, however, that ADF image intensity should not be interpreted literally to extract quantitative information about composition or thickness because of

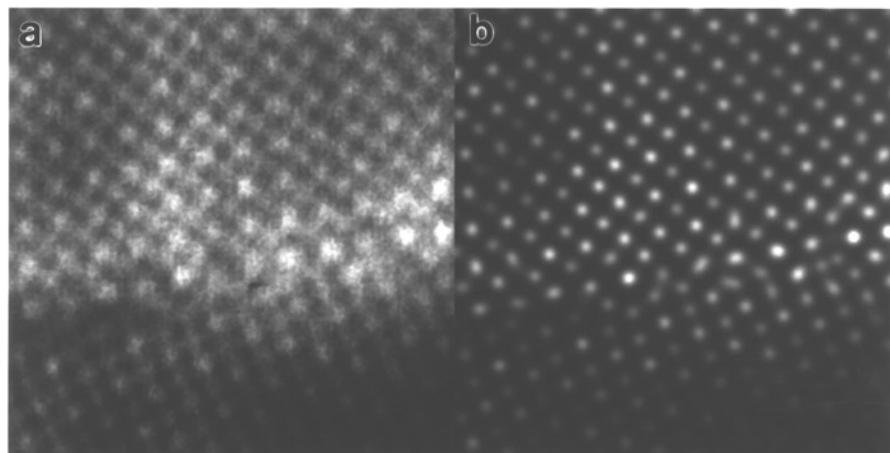


Figure 27. Asymmetric 25° [001] tilt boundary in SrTiO_3 : (a) as acquired HAADF Z-contrast STEM image; (b) maximum entropy image calculated from (a). White spots correspond to positions of metal-atom columns (from McGibbon *et al* 1996).

possible complications arising from multiple incoherent scattering in thick crystals (Treacy and Gibson 1993).

What does all this mean? High-angle ADF incoherent STEM imaging can provide high-resolution images of crystalline materials, somewhat insensitive to defocus and thickness, that can be rapidly and intuitively interpreted in terms of atomic arrangements. Furthermore, by taking advantage of the localized nature of the scattering from high-energy (> 100 eV) core-loss electrons, chemical discrimination at close to the atomic level can sometimes be achieved by using EELS with the stationary probe (Browning *et al* 1993, Muller *et al* 1995). Thus, in combination with its micro-analytical capabilities, the FEG-STEM represents a powerful instrument for microstructural investigations. Novel features of semiconductor interfaces and high- T_c superconductors are particularly noteworthy examples (Pennycook *et al* 1993), and an example of an asymmetric 25° [001] tilt boundary in SrTiO_3 is shown in figure 27 (McGibbon *et al* 1996). One serious limitation of the ADF imaging mode is the very low signal intensity which results in highly restricted grey-scale images. Marked enhancement of image quality has, however, been demonstrated, as apparent in figure 27(b), using maximum entropy image processing methods (Pennycook *et al* 1995). A second practical problem could be the lengthy computational time that might be required for simulating multiple images of alternate defect structures. Two- and three-fold astigmatism and coma must have some influence on the probe size and intensity distribution but, because of the sequential imaging process, the distortions present in CTEM images are less likely to be observed.

5.8. Structural information beyond the conventional resolution limits

Many non-microscopists are initially perplexed to learn that the positions of atomic columns can sometimes be located to within a few hundredths of a nanometre with an electron microscope that has a resolution limit of perhaps 10 or 20 times worse. What they do not appreciate is that this statement actually refers to the *relative* locations of well separated atomic column projections. Provided that the image signal is not seriously degraded by noise (Marks 1984), and that the image magnification is reasonably calibrated, then the positions

of image intensity maxima (or minima) can be determined with high precision and thus their separations can also be determined accurately. Examples of aperiodic defects have been documented in which these image extrema do not correspond to the atomic column positions (e.g. Bourret *et al* 1988a). Nevertheless, in a simulated study of an intergrowth defect in a complex perovskite (Saxton and Smith 1985), it was determined that the positions of metal-atom columns at the defect could generally be located to within ± 0.03 nm using many of the members of a through-focal series, while restoration of the series improved this uncertainty to ± 0.01 nm. However, at the same time, the oxygen atom columns were still invisible. In experimental studies of reconstructed Au(110) surface relaxations (Marks 1984), a similar uncertainty figure of ± 0.01 nm for Au atomic column locations was also obtained after careful comparisons of experimental and simulated images. Several other situations can be identified in which useful structural information beyond the conventional resolution limits can be extracted: these are described in the following paragraphs.

The combination of image plane and diffraction pattern information has recently received increased attention, especially since it offers the possibility of improved structural information for perfect crystals with dimensions in the range of 5 nm to ~ 1 μ m which are totally inaccessible to x-ray crystallography. Electron diffraction alone is insufficient to determine the structures because only the amplitudes, but not the phases, of the diffracted beams are available. Moreover, dynamical scattering must be avoided by using very thin crystals because otherwise the diffracted beams may not be easily related to the scattering factors. Using this technique of combining images and diffraction patterns, the positions of heavy-atom columns can be determined with great accuracy and light-atom columns may become visible depending on their projected location relative to the heavier metal atoms. Specimen drift is not such a problem as it is for imaging at the same resolution level, alignment and adjustment of the microscope are not so critical, and accurate knowledge of imaging parameters such as C_s is not required. But the crystal must be periodic over the region illuminated by the electron beam. In an early application (Hövmøller *et al* 1984), the projected potential of a transition metal oxide was determined, with metal atom coordinates accurate to within ± 0.01 nm, after correcting for optical distortions and imposing known crystallographic symmetry. In a recent study of $\text{Ti}_{11}\text{Se}_4$, the atomic structure was refined to an accuracy of ± 0.002 nm (Weirich *et al* 1996). Out-of-focus and astigmatic images can be restored by applying an appropriate filter to the Fourier transform of the digitized high-resolution image (Zou *et al* 1996). In a very recent development (Zandbergen *et al* 1997), the illuminated area for recording the electron diffraction pattern was typically restricted to a diameter of 5–20 nm. By recording images and/or diffraction patterns in multiple orientations, the technique becomes suitable for determining the atomic structure of small particles or inclusions. As shown in figure 28, it has already been used to characterize Mg_5Si_6 β'' precipitates in Al–Mg–Si alloys (Zandbergen *et al* 1997).

A closely related approach has been proposed (Hu and Li 1991) that is based on maximum entropy and phase extension. The procedure is initiated from a high-resolution electron micrograph that is usually recorded close to optimum defocus, and maximum entropy is first utilized to deconvolute the effect of the transfer function. The deconvoluted image is then Fourier transformed to obtain phases for the structure factors, while structure moduli are derived from the corresponding electron diffraction pattern after taking care to ensure recording linearity. Phase extension based on the Sayre equation is then applied to enhance the resolution (Sayre 1952). As shown in figure 29, application of the method to a mixed potassium–niobium oxide (Hu *et al* 1992) enabled all the projected columns of oxygen atoms to be resolved whereas only the cation columns could be resolved in any of

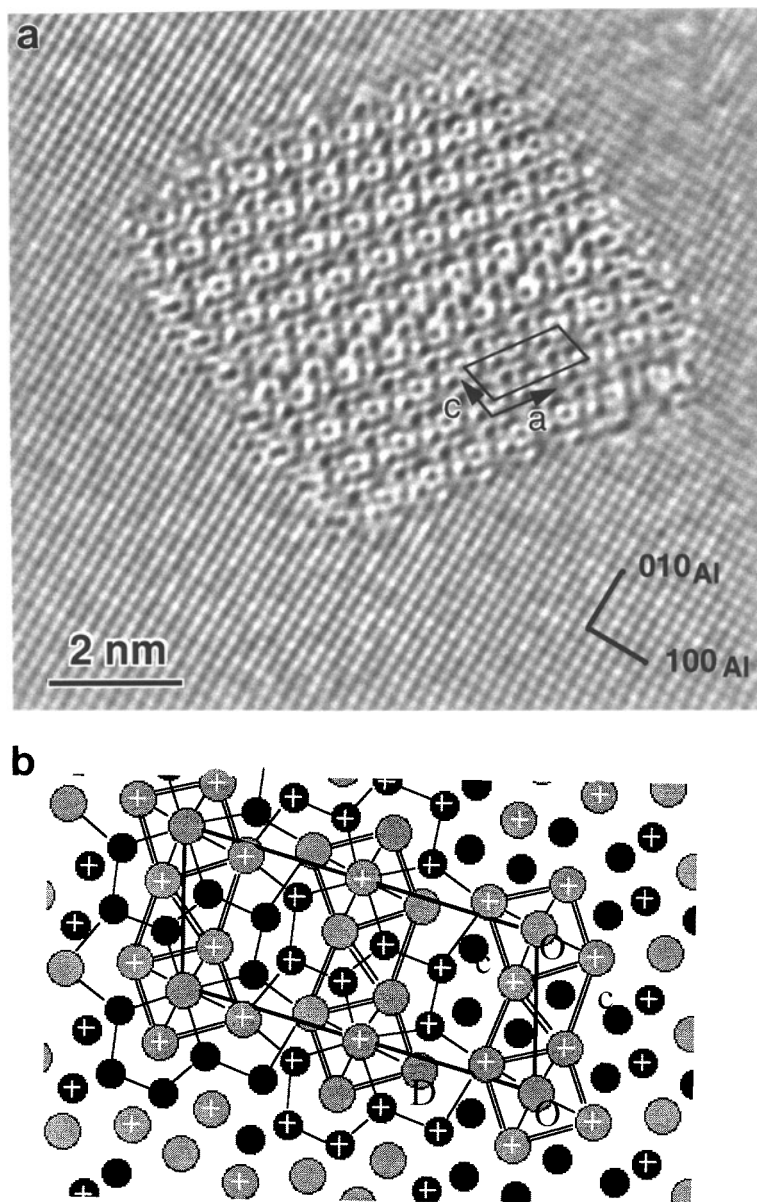


Figure 28. (a) Reconstructed phase of exit surface wavefunction showing small Mg_5Si_6 β'' -phase precipitate in Al-Mg-Si alloy, (b) Refined structural model derived from (a) after combining information from multiple small-area electron diffraction patterns (from Zandbergen *et al* 1997).

the original high-resolution images of the material. A later paper (Fu *et al* 1994) described application of the phase-extension method to an incommensurate modulation in a high- T_c superconductor. Strictly speaking, the technique is really only applicable in the absence of dynamical scattering (Dorset 1995), and it cannot be applied to aperiodic structural defects. On the other hand, no prior knowledge of the basic crystal structure is required for its

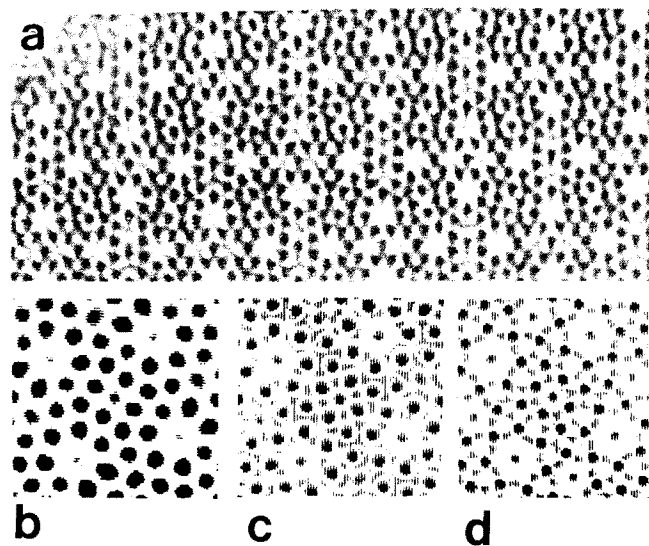


Figure 29. Application of maximum entropy and phase extension to crystal of $\text{K}_2\text{O} \cdot 7\text{Nb}_2\text{O}_5$: (a) original high-resolution image before processing. Black spots represent metal-atom positions. (b) Structure image of unit cell after image deconvolution; (c) image after first application of phase extension; (d) final high-resolution structure after three cycles of Fourier calculations. All projected atomic columns including oxygen are clearly visible (from Hu *et al* 1992).

successful application. One final problem is that multiple solutions are likely to result from applying the technique to simple crystal structures (Huang *et al* 1996), and analytical procedures must be adopted in order to determine the correct solution.

Another image-diffraction pattern approach (Dong *et al* 1992) used maximum entropy to progressively extend the image resolution for a beam-sensitive hydrocarbon from the original 0.32 nm as far as the 0.10 nm resolution of the electron diffraction pattern, which must be kinematical for the method to be applicable. The method starts with phases available from the transformed image and successively assigns phases of 0 or π to additional reflections, with the 'correct' choice being determined by a maximum likelihood criterion (Bricogne 1984). In this particular study, the perchlorocoronene structure was already known from x-ray diffraction so that a check of the reliability of the method was available. The maximum entropy method should be applicable to other materials to the resolution limit of the kinematical diffraction pattern provided that some low-resolution phase information is initially available.

The possible extension of these various approaches to three-dimensional structure refinement was implied by a recent study (Downing *et al* 1990) in which high-resolution images of the staurolite mineral were recorded in five major projections, as illustrated in figure 30 (O'Keefe *et al* 1994). Focal series were recorded in each projection, followed by Fourier transformation to yield the structure factors which were then corrected to compensate for the fall-off of the intensity spectrum amplitudes due to partial coherence envelopes. From the full three-dimensional data set, the inverse Fourier transform yielded the three-dimensional crystal structure, including the positions of some lighter atoms which were invisible in some projections due to their proximity to the other heavier atoms. This particular restoration of the staurolite structure was limited in resolution to about 0.14 nm but incorporation of electron diffraction pattern information as described above could have

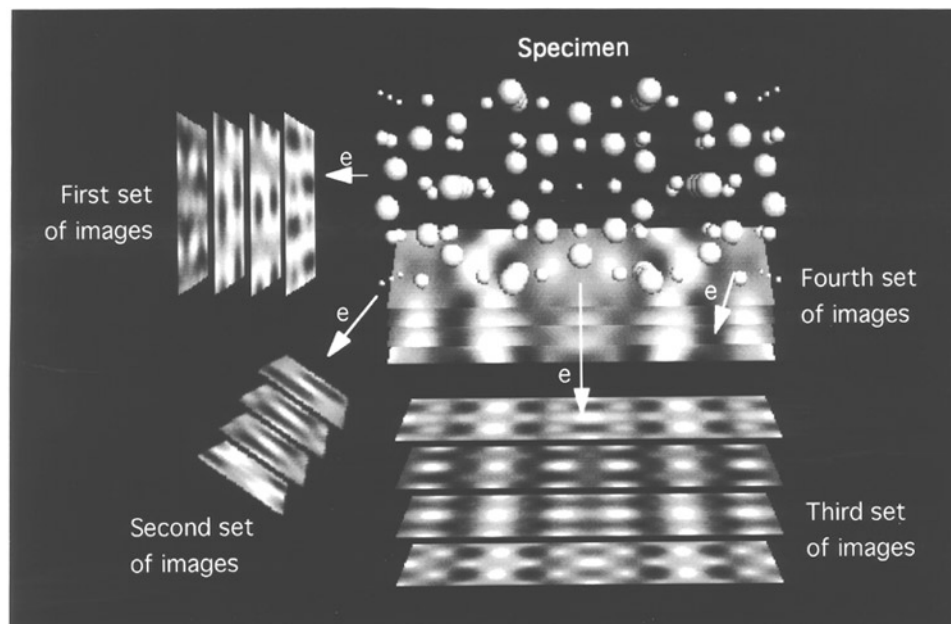


Figure 30. Illustration of the method used for the compilation of the three-dimensional data set using a series of two-dimensional projections of crystalline staurolite mineral (from O'Keefe *et al* 1994).

permitted some improvement to be achieved.

Procedures for determining atomic positions from multiple diffraction patterns recorded with the nanoprobe of a STEM have also received attention. One approach utilized electron nanodiffraction patterns from overlapping regions of Si(110) crystals (Konnert *et al* 1989). Another novel approach to 'super-resolution' has been proposed that relies entirely on coherent microdiffraction (Rodenburg *et al* 1993). Its basis is a phase-retrieval algorithm that processes a four-dimensional data set. In this technique, the focused probe is moved stepwise along a line across a thin part of the sample. At each position of the probe, the coherent microdiffraction pattern after energy-filtering is recorded with a TV-rate CCD camera (Nellist and Rodenburg 1994). By taking a Fourier transformation with respect to the probe position, amplitude and phase information becomes available that can be directly related to the projected sample structure. As an example, figure 31(a) shows the typical interference fringes visible in a coherent microdiffraction pattern from a thin Si111 crystal, and figure 31(b) shows the reconstructed phase of the exit-surface wavefunction based on processing of the entire data set (Nellist *et al* 1995). The pairs of Si atomic columns separated by 0.136 nm in this projection are clearly resolved, yet the STEM used in the data acquisition had a point resolution for bright-field imaging of only 0.42 nm. The extreme magnitude of the data set required would appear to limit the application of the technique to very special cases for the near future. The basic problem is that, for each probe position, representing a single pixel in the final image, a full two-dimensional diffraction pattern must be recorded. For large-unit-cell or defective materials, Fourier space will need to be sampled more finely which, with present data handling and storage capabilities, will require much, much longer than the 40 min apparently needed to acquire the data set used for generating figure 31(b).

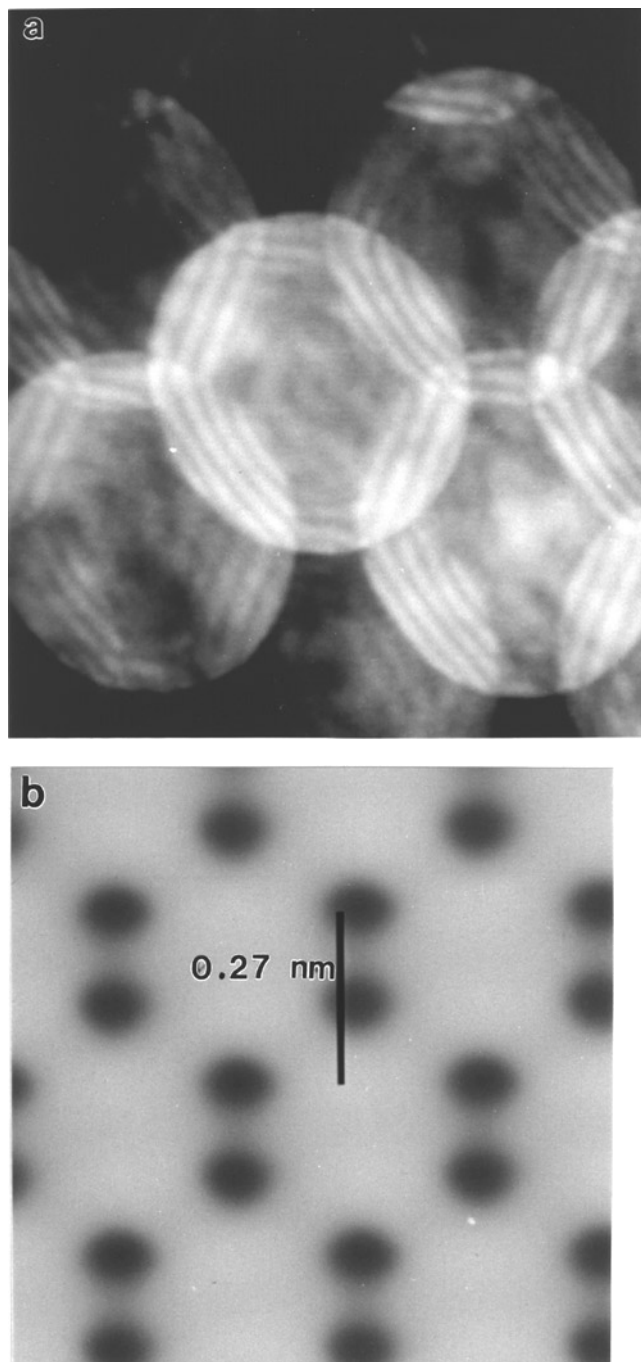


Figure 31. (a) Interference fringes in the region of disk overlap in the coherent microdiffraction pattern from Si crystal in [110] projection; (b) phase of exit-surface wavefunction for Si crystal in [110] orientation after calculation of Fourier transformation from real-space scan of probe (from Nellist *et al* 1995)

6. Problems

In common with all advanced experimental techniques, atomic-resolution electron microscopy has its own underlying and characteristic problem areas: several of these are identified and briefly discussed in the following sections.

6.1. Noise

Quantitative electron microscopy depends on the integrity of the entire imaging process: statistical noise originating from the imaging-detection process or noise from the sample itself can have a serious detrimental influence on the reliability of the final result. Signal averaging will clearly enhance image quality. Indeed, it is indispensable to macromolecular crystallography where the sensitivity of biological crystals to electron irradiation damage severely restricts the total electron exposure (Glaeser 1985). However, averaging is obviously inapplicable to any material with aperiodic features, although low-pass smoothing filters can always be used to improve the local image appearance. Pattern recognition techniques have been developed that allow repetitive structural units at interfaces to be detected and thus permit the influence of noise to be reduced (Paciornik *et al* 1996, Rosenauer *et al* 1996). An adaptive Fourier filtering technique has also been proposed and shown to remove noise from interface images without having any detrimental effects on the spatial resolution of the micrograph (Möbus *et al* 1993). The proposed use of Wiener filters rather than Fourier filters to restore noisy HREM images may prove to be highly effective in many situations (Marks 1996).

The impact of instrumental noise can be reduced by increasing the total electron signal (signal-to-noise ratio) but physical limits on the dynamic range of available detectors usually necessitates that higher magnification settings must then be selected, and radiation damage could become a serious issue even for non-biological materials (see section 6.2). However, almost without exception, amorphous overlayers on the sample have a greater contribution to the degradation of the recorded image quality. No matter what thinning method is used, and no matter how much care is taken with sample preparation, most materials will have a surface oxide or 'contamination' layer. Since the final image is formed by electrons that have traversed through the entire thickness of the sample, some effect of this layer on the image is inevitable.

Several papers have addressed this specific issue of specimen-borne noise. A quantitative method for assessment of noise has been developed based on the rms deviation of intensity peaks from an average lattice (Paciornik *et al* 1993). The simulations of noise superimposed on images of a simple $\Sigma = 3$ Si twin boundary shown in figure 32 (Kilaas and Gronsby 1993) are a good example demonstrating the trend that considerable shifts and even disappearance of intensity extrema occur, and the visibility of the defect itself gets progressively worse as the thickness of the amorphous layer becomes comparable with that of the crystalline material. In a quantitative study of alternative thinning methods for Si, the experimental SNR for {111} lattice fringes relative to vacuum was used as the comparison measure (Gibson and McDonald 1987).

In conclusion, the electron microscopist should always take steps wherever possible to eliminate, or at least reduce, the surface-generated noise. For example, the commonly used method of crushing oxide specimens with a mortar and pestle does not usually lead to any surface contamination layer when a purified solvent is used (Smith *et al* 1986a). A final reduction in ion-milling voltage to about 1 kV or perhaps a light chemical etch will remove much of the amorphized surface layer that results from standard ion-milling conditions

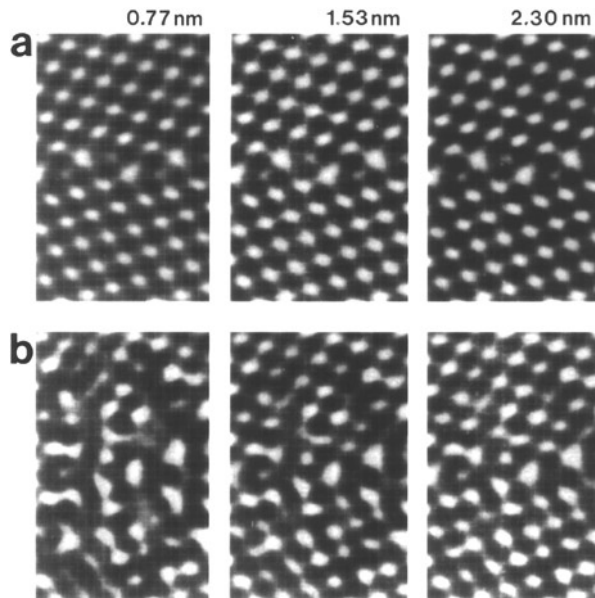


Figure 32. (a) Simulated images for $\Sigma = 9$ Si twin boundary of increasing thickness from left to right as shown; (b) Effect of superimposed noise originating from native surface oxide overlayers of thickness 3.14 nm (from Kilaas and Gronsky 1985).

(4–5 keV). Conversely, complete removal of the amorphous layer means that an alternative autotuning method for alignment of the microscope will be needed (see section 5.2).

6.2. Radiation damage

Any particle–solid interaction is liable to result in permanent structural modification and the highly energetic electron beam striking the sample within the electron microscope is no exception. Electron microscopists must continually be alert of the possibility that the morphology of their sample is being altered, probably irreversibly, during the process of imaging (or when recording micro-analytical data). A cautious microscopist will monitor the sample appearance during the period of observation and thus be in a position to discount results obtained once changes start to become apparent (Hofmann and Ernst 1994b). Indeed, quantitative comparison of electron micrographs of a $\Sigma = 3$ (111) twin boundary in NiAl were recorded at regular intervals with a slow-scan CCD camera in a high-voltage HREM as a means of establishing the maximum useful length to the viewing period (Nadarzinski and Ernst 1996). Higher viewing magnifications as a means to improve signal statistics must imply increased beam current density, which in turn will normally mean greater rates of damage since the current density increases with the square of the magnification if the screen brightness is to be maintained at a constant level. For quantitative work, it is always advisable to limit the image magnification and restrict the beam current density whenever possible, and the region of sample studied should be periodically checked for signs of structural change. Of course, the microscope should be pre-aligned and the specimen pre-oriented using a nearby region to limit the total dose sustained by the area of interest.

There are two basic avenues for electron beam damage (Hobbs 1984): radiolytic processes (sometimes known as ‘ionization damage’) which involve electron–electron

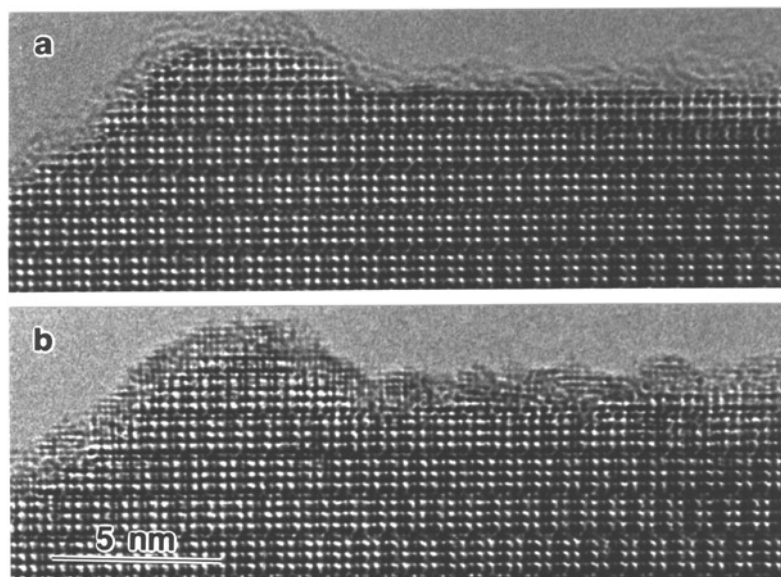


Figure 33. Profile images of titanium niobate, $\text{Ti}_2\text{Nb}_{10}\text{O}_{29}$, recorded at 400 keV; (b) was recorded 20 min after (a) following continuous electron irradiation of $\sim 15 \text{ A cm}^{-2}$. The appearance of reduced oxide is due to the electron-stimulated desorption of oxygen (from Smith *et al* 1987a).

interactions and affect most covalent and ionic solids; and direct atomic ‘knock-on’ displacements which occur above characteristic energy thresholds. For example, an electron energy of 400 keV is sufficient to cause bulk displacements in elements as heavy as copper ($Z = 29$). Because of reduced binding energy, the energy needed for the activation of surface sputtering or for diffusion at defects is likely to be considerably less than the bulk values. The pair of images of titanium niobate shown in figure 33 illustrate this latter point. As a result of continuous electron irradiation over a time interval of 20 min, using a beam current density at the specimen of $\sim 15 \text{ A cm}^{-2}$ (which is only about 3–5 times greater than that typically used for atomic-resolution viewing and recording), depletion of oxygen from the near-surface region occurred as a result of electron-stimulated desorption, leaving a reduced oxide covering the surface (Smith *et al* 1987a). In a quantitative comparison of difference images from a Cu/sapphire interface (Dehm *et al* 1996), preferential damage was documented to occur at the interface, limiting the total viewing time to ~ 10 min (1250 keV, magnification of $600\,000\times$, specimen current density of $\sim 1.6 \text{ A cm}^{-2}$). Structural change is even more likely to occur when using the intense, focused probe of the STEM to carry out micro-analysis: rapid loss of oxygen from precipitates in Si was reported even at 100 keV (Bourret and Colliex 1982). On the other hand, for beam-sensitive crystalline specimens, the advantages of signal averaging over many unit cells as a means of prolonging the structural integrity is well known (see, for example, Kuo and Glaeser 1975, Glaeser 1985).

6.3. Inversion of crystal scattering

Inversion of crystal scattering to retrieve the crystal potential in the presence of dynamical scattering is unquestionably the major unresolved problem confronting the field of atomic-resolution electron microscopy. As described earlier (see section 5.5), a multitude of

methods exist for retrieving the exit-surface wavefunction, and for very thin samples when the kinematical or weak phase object approximations are valid, Fourier inversion can be used to extract the crystal potential, in some cases to extremely high resolution (see section 5.8). Excellent agreement between experimental micrographs and simulated images, at least after intensity normalization, has been documented in many cases. However, *ab initio* inversion of crystal scattering to retrieve the crystal potential has received comparatively scant attention. An iterative method based on inversion of the multislice algorithm was proposed (Beeching and Spargo 1993), and its validity domain for the known rutile (001) structure was later investigated by reference to Bloch wave analysis and found to be closely coupled to the onset of strong dynamical scattering (Spargo *et al* 1994). Further work is needed to explore the applicability of the method, in particular its usefulness for extending the thickness limits for crystal structure determination in the case of non-periodic wavefields (Beeching and Spargo 1997). Meanwhile, an alternative approach based on a simulated annealing algorithm has been explored using the known GaAs [110] structure (Lentzen and Urban 1996). Successful reconstruction was achieved for a thickness of 5.6 nm but the search algorithm converged towards a totally different, but equally valid, structure at a thickness of 11.2 nm. This result thus highlights the problem of multiple solutions to the inverse scattering problem. Much more work needs to be done before the uniqueness of the inversion process for an unknown structure can be established. Direct inversion of dynamical electron diffraction patterns to retrieve crystal structure factors may offer a viable alternative for deriving unknown crystal structures (Spence 1997).

7. Concluding remarks

Our objective has been to provide an overview of atomic-resolution studies with the electron microscope, to highlight some of its achievements, and to identify areas of active research and development. Many of the topics surveyed here are in a state of flux, and further developments in quantification and many novel applications can safely be predicted to occur over a short time interval. Enhancement of digital recording and image processing, increased use of computers for online microscope control and real-time interactive structure refinement, and *in situ* specimen treatment facilities are identified as areas of particular activity. For the experts in the field many challenges remain. How to account for the differences in absolute contrast levels between theory and experiment? How best to optimize the structure refinement procedure? How to minimize statistical and systematic errors and reduce the influence of noise? How to invert crystal scattering? How to cope with inelastic scattering? Despite these open-ended questions, it is inescapable that the atomic-resolution microscope enables the atomic structure of interfaces and defects, for example, to be determined routinely, reliably and with very high positional accuracy, with the potential to provide better insights into the physical behaviour of many materials systems. Experts in the field of atomic-resolution microscopy have a collective responsibility to ensure that their colleagues who have a primary interest in materials properties are given the opportunity and assistance needed to capitalize on these benefits.

Acknowledgments

I am grateful to Dr Knut Urban and the Forschungszentrum Jülich for generous support of sabbatical leave during which period this review article was substantially written, and I thank many microscopy colleagues for kindly providing examples of their work for inclusion.

Finally, I acknowledge my indebtedness to my late friend and colleague Mike Stobbs for his valuable advice and cheerful encouragement generously given over many years.

References

- Ajayan P M and Marks L D 1988 *Phys. Rev. Lett.* **60** 585
 Ajika N, Endoh H, Hashimoto H and Tomita M 1985 *Phil. Mag. A* **51** 729
 Allpress J G, Hewat E A, Moodie A F and Sanders J V 1972 *Acta Crystallogr. A* **28** 528
 Allpress J G and Sanders J V 1969 *J. Appl. Crystallogr.* **6** 165
 Amelinckx S, Milat O and van Tendeloo G 1993 *Ultramicroscopy* **51** 90
 Amelinckx S, van Tendeloo G and van Landuyt J 1985 *Ultramicroscopy* **18** 395
 Andersson A, Borin J-O and Walter P 1986 *J. Catal.* **98** 204
 Angelo J E and Mills M J 1995 *Phil. Mag. A* **72** 635
 Banfield J F, Veblen D R and Smith D J 1991 *Am. Mineral.* **76** 343
 Bardal A, Eibl O, Mathee Th, Friedl G and Wecker J 1993 *J. Mater. Res.* **8** 2112
 Barry J C 1991 *Phil. Mag. A* **64** 111
 Barry J C and Anstis G R 1994 *Mater. Forum* **18** 31
 Batstone J L, Phillips J M and Hunke E C 1988 *Phys. Rev. Lett.* **60** 1394
 Bayle P, Deutsch T, Gilles B, Lançon F, Marty A and Thibault J 1994 *Ultramicroscopy* **56** 94
 Beeching M J and Spargo A E C 1993 *Ultramicroscopy* **52** 243
 ——— 1997 *J. Microsc.* in press
 Biegelsen D, Smith D J and Tong S-Y (eds) 1993 *Atomic Scale Imaging of Surfaces and Interfaces, MRS Symp. Proc.* 295 (Pittsburgh, PA: Materials Research Society)
 Bierwolf R, Hohenstein M, Philipp F, Brandt O, Crook G E and Ploog K 1993 *Ultramicroscopy* **49** 273
 Bourret A and Bacmann J J 1985 *Surf. Sci.* **162** 495
 Bourret A and Colliex C 1982 *Ultramicroscopy* **9** 183
 Bourret A, Desseaux J and Renault A 1982 *Phil. Mag. A* **45** 1
 Bourret A, Fuoss P, Feuillet G and Tatarenko S 1993 *Phys. Rev. Lett.* **70** 311
 Bourret A and Penisson J-M 1987 *JEOL News E* **25** 2
 Bourret A, Rouviere J L and Penisson J M 1988b *Acta Crystallogr. A* **44** 838
 Bourret A, Rouviere J L and Spendeler J 1988a *Phys. Status Solidi a* **107** 481
 Bourret A, Thibault-Desseaux J, D'Anterrosches C, Penisson J M and DeCrecy A 1983 *J. Microsc.* **129** 337
 Bovin J-O, Malm J-O, Petford-Long A K, Smith D J and Schmid G 1988 *Z. Angew. Chem.* **27** 555
 Bovin J-O, Wallenberg L R and Smith D J 1985 *Nature* **317** 47
 Boyes E D, Gai P L and Hanna L G 1996 *Mater. Res. Soc. Symp. Proc.* **404** 53
 Bricogne G 1984 *Acta Crystallogr. A* **40** 410
 Browning N D, Chisholm M F and Pennycook S J 1993 *Nature* **366** 143
 Buckett M I, Shaffer J P and Merkle K L 1993 *Mater. Res. Soc. Symp. Proc.* **295** 109
 Buckett M I, Strane J, Luzzi D E, Zhang J P, Wessels B W and Marks L D 1989 *Ultramicroscopy* **29** 217
 Budinger T F and Glaeser R M 1976 *Ultramicroscopy* **2** 31
 Bulle-Lieuwma C W T, de Jong A F, van Ommen A H, van der Veen J F and Vrijmoeth J 1989 *Appl. Phys. Lett.* **55** 648
 Bursill L A and Lin P J 1989 *Phil. Mag. A* **60** 307
 Bursill L A and Smith D J 1984 *Nature* **309** 319
 Bursill L A, Smith D J and Evans R G 1988 *Proc. R. Soc. A* **415** 227
 Campbell G H 1996 *J. Am. Ceram. Soc.* **79** 2883
 Campbell G H, Chan D K, Medlin D L, Angelo J E and Carter C B 1996 *Scripta Mater.* **35** 837
 Campbell G H, Foiles S M, Gumbsch P, Rühle M and King W E 1993b *Phys. Rev. Lett.* **70** 449
 Campbell G H, Wien W L, King W E, Foiles S M and Rühle M 1993a *Ultramicroscopy* **51** 247
 Carter C B, McKernan S, Rasmussen D R, Simpson Y K, Summerfelt S R, Susnitsky D W and Tietz L A 1989 *Mater. Res. Soc. Symp. Proc.* **139** 189
 Catana A, Heintze M, Schmid P E, Stadelmann P and Levy Y 1989 *Mater. Res. Soc. Symp. Proc.* **139** 369
 Catana A, Schmid P E, Lu P and Smith D J 1992 *Phil. Mag. A* **66** 933
 Cerva H, Krost A, Schnabel R F and Bimberg D 1995 *Phil. Mag. A* **71** 1145
 Chang Y C and Howe J M 1993 *Ultramicroscopy* **51** 46
 Chen W-J and Chen F-R 1993 *Ultramicroscopy* **51** 316
 Chen F-R, Chu C-C, Wang J-Y and Chang L 1995 *Phil. Mag. A* **72** 529

- Chien F R, Nutt S R, Carulli J M, Buchan N, Beetz C P and Yoo W S 1994 *J. Mater. Res.* **9** 2086
- Cherns D, Anstis G R, Hutchison J L and Spence J C H 1982 *Phil. Mag. A* **46** 849
- Coene W, de Jong A F, van Dyck D, van Tendeloo G and van Landuyt J 1988 *Phys. Status Solidi a* **107** 521
- Coene W M J and Denteneer T J J 1991 *Ultramicroscopy* **38** 235
- Coene W, Janssen G, Op de Beeck M and van Dyck D 1992 *Phys. Rev. Lett.* **69** 3743
- 1993 *Inst. Phys. Conf. Ser.* **138** 225
- Coene W M J, Thust A, Op de Beeck M and van Dyck D 1996 *Ultramicroscopy* **64** 109
- Cosslett V E *et al* 1979 *Nature* **281** 49
- Cowley J M 1969 *Appl. Phys. Lett.* **15** 58
- 1976 *Ultramicroscopy* **2** 3
- 1981 *Diffraction Physics* 2nd edn (Amsterdam: North-Holland)
- Cowley J M and Moodie A F 1957a *Acta Crystallogr.* **10** 609
- 1957b *Proc. Phys. Soc.* **70** 486
- Cowley J M and Smith D J 1987 *Acta Crystallogr. A* **41** 739
- Crewe A V, Langmore J P and Isaacson M S 1975 *Physical Aspects of Electron Microscopy and Microbeam Analysis* (New York: Wiley) p 47
- Crewe A V, Wall J S and Langmore J P 1970 *Science* **168** 1338
- Crewe A V, Wall J B and Welter L M 1968 *J. Appl. Phys.* **39** 5861
- Daberkow, I, Herrmann K-H, Liu L B and Rau W D 1991 *Ultramicroscopy* **38** 215
- Dahmen U, Hetherington C J D, O'Keefe M A, Westmacott K H, Mills M J, Daw M S and Vitek V 1990 *Phil. Mag. Lett.* **62** 327
- Dahmen U, Kim M G and Searcy A W 1987 *Ultramicroscopy* **23** 365
- Dahmen U, Paciornik S, Solorzano I G and Vandersande J 1994 *Interface Sci.* **2** 125
- Dai J Y, Xing Z P, Wang Y G, Li D X, Guo J T, He L L and Ye H Q 1994b *Mater. Lett.* **20** 23
- Dai J Y, Wang Y G, Li D X and Ye H Q 1994a *Phil. Mag. A* **70** 905
- D'Anterrosches C and Bourret A 1984 *Phil. Mag. A* **49** 783
- Daw M S and Baskes M I 1983 *Phys. Rev. Lett.* **50** 1285
- de Crecy A, Bourret A, Naka S and Lasalmonie A 1983 *Phil. Mag. A* **47** 245
- Dehm G, Nadarzynski K, Ernst F and Rühle M 1996 *Ultramicroscopy* **63** 49
- Dehm G, Rühle M, Ding G and Raj R 1995 *Phil. Mag. B* **71** 1111
- de Jong A F, Coene W and Bender H 1987 *Inst. Phys. Conf. Ser.* **87** 9
- de Jong A F and Koster A J 1992 *Scanning Microscopy* suppl. 6, ed P W Hawkes (Chicago, IL: Scanning International) p 95
- de Jong A F and van Dyck D 1993 *Ultramicroscopy* **49** 66
- de Ruijter W J 1995 *Micron* **26** 247
- de Ruijter W J, Sharma R, McCartney M R and Smith D J 1995 *Ultramicroscopy* **57** 409
- de Ruijter W J and Weiss J K 1992 *Rev. Sci. Instrum.* **63** 4314
- 1993 *Ultramicroscopy* **50** 269
- Dierksen K, Typke D, Hegerl R, Koster A J and Baumeister W 1992 *Ultramicroscopy* **40** 71
- Dong W, Baird T, Fryer J R, Gilmore C J, MacNicol D D, Bricogne G, Smith D J, O'Keefe M A and Hovmöller S 1992 *Nature* **355** 605
- Dorignac D, Casanove M J, Jagut R and Jouffrey B 1980 *Electron microscopy 7th Eur. Congress on Electron Microscopy Foundation (Leiden)* vol 4, ed P Brederoo and J van Landuyt p 174
- Dorignac D, MacLachlan M E C and Jouffrey B 1976 *Ultramicroscopy* **2** 49
- Dorset D L 1995 *Structural Electron Crystallography* (New York: Plenum) p 145–6
- Dowell W C T 1963 *Optik* **20** 535
- Downing K and Grano D A 1982 *Ultramicroscopy* **7** 381
- Downing K, Meisheng H, Wenk H-R and O'Keefe M A 1990 *Nature* **348** 525
- Downing K H, Koster A J and Typke D 1992 *Ultramicroscopy* **46** 189
- Epicier T 1990 *Mater. Res. Soc. Symp. Proc.* **183** 255
- Epicier T, Thomas G, Wohlfromm H and Moya J S 1991 *J. Mater. Res.* **6** 138
- Erasmus S J and Smith K C A 1982 *J. Microsc.* **127** 185
- Ernst F, Finnis M W, Hofmann D, Muschik T, Schönberger U, Wolf U and Methfessel M 1992 *Phys. Rev. Lett.* **69** 620
- Evans R G, Bursill L A and Smith D J 1986 *Optik* **72** 137
- Eyring L 1988 *High-Resolution Transmission Electron Microscopy and Related Techniques* (Oxford: Oxford University Press) ch 10
- Fallon P J, Brown L M, Barry J C and Bruley J 1995 *Phil. Mag. A* **72** 21

- Flueli M, Buffat P A and Borel J-P 1988 *Surf. Sci.* **202** 343
- Fonda R W and Luzzi D E 1993 *Phil. Mag. A* **68** 1151
- Frank J 1973a *Optik* **38** 519
- 1973b *Advanced Techniques in Biological Electron Microscopy* (Heidelberg: Springer) p 214
- 1976 *Optik* **44** 379
- Frank J, Shimkin B and Dowse H 1981 *Ultramicroscopy* **6** 343
- Fu Z Q, Huang D X, Li F H, Li J Q, Zhao Z X, Cheng T Z and Fan H F 1994 *Ultramicroscopy* **54** 229
- Fukuhara A, Komoda T and Tadano B 1966/1967 *Optik* **24** 513
- Gao Y and Merkle K L 1990 *J. Mater. Res.* **5** 1995
- Gerthsen D 1993 *Phil. Mag. A* **67** 1365
- Gibson J M 1994 *Ultramicroscopy* **56** 26
- Gibson J M and McDonald M L 1987 *Mater. Res. Soc. Symp. Proc.* **82** 109
- Gibson J M, McDonald M L and Unterwald F C 1985 *Phys. Rev. Lett.* **55** 1765
- Glaeser R M 1985 *Ann. Rev. Phys. Chem.* **36** 548
- Glaisher R M, Spargo A E C and Smith D J 1989a *Ultramicroscopy* **27** 131
- 1989b *Ultramicroscopy* **27** 19
- Glanvill A R, Moodie A F, Whitfield H J and Wilson I J 1985 *Aust. J. Phys.* **39** 71
- Goodman P and Moodie A F 1974 *Acta Crystallogr. A* **30** 280
- Gronsky R and Thomas G 1983 *Proc. 41st Ann. Meet. of the Electron Microscopy Society of America*, ed G W Baile (San Francisco, CA: San Francisco Press) p 310
- Gubbens A J and Krivanek O L 1993 *Ultramicroscopy* **51** 146
- Gutenkunst G, Mayer J and Rühle M 1994 *Scripta Metall. Mater.* **31** 1097
- Haider M and Zach J 1995 *Proc. Microscopy and Microanalysis* ed G W Bailey *et al* (New York: Jones and Begall) p 596
- Haine M E and Mulvey T 1954 *J. Sci. Instr.* **35** 466
- Hanszen K-H 1971 *Adv. Opt. Electron Microsc.* **4** 1
- Harscher A, Lang G and Lichte H 1995 *Ultramicroscopy* **58** 79
- Hasegawa T, Kobayashi K, Ikarashi N, Takayanagi K and Yagi K 1986 *Japan. J. Appl. Phys.* **25** L333
- Heinemann K 1971 *Optik* **34** 117
- Hemker K J, Viguier B and Mills M J 1993 *Mats. Sci. Eng. A* **164** 391
- Herrmann K-H 1978 *J. Phys. E: Sci. Instrum.* **11** 1076
- 1983 *J. Microsc.* **131** 67
- Herrmann K-H and Krahel D 1984 *Adv. Opt. Electron Microsc.* **4** 1
- Herrmann K-H, Krahel D, Rust H-P and Ulrichs O 1976 *Optik* **44** 393
- Hetherington C J D, Barry J C, Bi J M, Humphreys C J, Grange J and Wood C 1985 *Mater. Res. Soc. Symp. Proc.* **137** 41
- Hetherington C J D, Dahmen U, O'Keefe M A, Kilaas R, Turner J, Mills M J and Vitek V 1990 *Mater. Res. Soc. Symp. Proc.* **183** 45
- Heuer A, Kraus-Lanteri S, Labun P A, Lanteri and Mitchell T E 1985 *Ultramicroscopy* **18** 355
- Hirabayashi M, Hiraga K and Shindo D 1982 *Ultramicroscopy* **9** 197
- Hiraga K, Hirabayashi M, Hayashi S and Hirai T 1983a *J. Am. Ceram. Soc.* **66** 539
- Hiraga K, Lincoln F J and Sun W 1991 *Mater. Trans. JIM* **32** 308
- Hiraga K and Sun W 1993 *Phil. Mag. A* **67** 117
- Hiraga K, Tsuno K, Shindo D, Hirabayashi M, Hayashi S and Hirai T 1983b *Phil Mag. A* **47** 483
- Hobbs L W 1984 *Quantitative Electron Microscopy* ed J N Chapman and A J Craven (Edinburgh: Scottish Universities Summer School in Physics) p 399
- Hoche T, Kenway P R, Kleebe H-J and Rühle M 1993 *Atomic Scale Imaging of Surfaces and Interfaces (MRS Symp. Proc. 295)* ed D Biegelsen, D J Smith and S-Y Tong (Pittsburgh, PA: Materials Research Society) p 115
- Hofmann D and Ernst F 1994a *Interface Sci.* **2** 201
- 1994b *Ultramicroscopy* **53** 205
- Honda T, Tomita T, Kaneyama T and Ishida Y 1994 *Ultramicroscopy* **54** 132
- Horiuchi S 1994 *Fundamentals of High Resolution Transmission Electron Microscopy* (Amsterdam: North-Holland)
- Horiuchi S, Matsui Y, Kitami Y, Yokoyama M, Suehara S, Wu X J, Matsui I and Katsuta T 1991 *Ultramicroscopy* **39** 231
- Hovmöller S 1990 *Ultramicroscopy* **41** 121
- Hovmöller S, Sjögröm A, Farrants G, Sundberg M and Marinder B-O 1984 *Nature* **311** 238
- Howe J M 1996 *Phil. Mag. A* **74** 761

- Howe J W, Benson W E, Garg A and Chang Y-C 1994 *Mater. Res. Soc. Symp. Proc.* **332** 65
- Hu J J and Li F H 1991 *Ultramicroscopy* **35** 339
- Hu J J, Li F H and Fan H F 1992 *Ultramicroscopy* **41** 387
- Huang D X, He W Z and Li F-H 1996 *Ultramicroscopy* **62** 141
- Hull R, Hsieh Y F, Short K T, White A E and Cherns D 1990 *Mater. Res. Soc. Symp. Proc.* **183** 91
- Hull R, Rosner S J, Koch S N and Haris J S 1986 *Appl. Phys. Lett.* **49** 1714
- Humphreys C J and Spence J C H 1978 *Optik* **58** 125
- Hutchison J L and Anderson J S 1972 *Phys. Status Solidi* **a** **9** 207
- Hutchison J L and Briscoe N A 1985 *Ultramicroscopy* **18** 435
- Hutchison J L, Honda T and Boyes E D 1986 *JEOL News* **E** **24** 9
- Hýtch M J and Stobbs W M 1994 *Ultramicroscopy* **53** 191
- Ichinose H 1994 *Int. Workshop on High-Voltage and High-Resolution Electron Microscopy (Stuttgart, 1994)* unpublished work
- Ichinose H and Ishida Y 1981 *Phil. Mag. A* **43** 1253
- 1989 *Phil. Mag. A* **60** 555
- Ichinose H, Ishida Y, Baba N and Kanaya K 1985 *Phil. Mag. A* **52** 51
- Iijima S 1971 *J. Appl. Phys.* **42** 5891
- Iijima S and Ichihashi T 1985 *Japan. J. Appl. Phys.* **24** 1125
- 1986 *Phys. Rev. Lett.* **56** 616
- Iijima S and O'Keefe M A 1979 *J. Microsc.* **117** 347
- Ikarashi N, Kobayashi K, Koike H, Hasegawa T and Yagi K 1988 *Ultramicroscopy* **26** 195
- Ikarashi N, Sakai A, Baba T and Ishida K 1989 *Appl. Phys. Lett.* **55** 2509
- Ikuhara Y and Pirouz P 1993 *Ultramicroscopy* **52** 421
- Ikuhara Y, Pirouz P, Yadavalli and Flynn C P 1995 *Phil. Mag. A* **72** 179
- Isaacson M, Langmore J, Parker N W, Kopf D and Utlaut K 1976 *Ultramicroscopy* **1** 359
- Isaacson M, Kopf D, Utlaut M, Parker N W and Crewe A V 1971 *Proc. Natl. Acad. Sci. USA* **74** 1802
- Ishida K 1995 *Inst. Phys. Conf. Ser.* **146** 1
- Ishida Y, Ichinose H, Mori M and Hashimoto M 1983 *Trans. Japan. Inst. Metals* **24** 349
- Ishizuka K 1993 *Ultramicroscopy* **52** 7
- 1994 *Ultramicroscopy* **55** 407
- Ishizuka K, Tanji T, Tonomura A, Ohno T and Murayama Y 1994 *Ultramicroscopy* **55** 197
- Isoda S, Saitoh K, Moriguchi S and Kobayashi T 1991 *Ultramicroscopy* **35** 329
- Isoda S, Saitoh K, Ogawa T, Moriguchi S and Kobayashi T 1992 *Ultramicroscopy* **41** 99
- Isshiki T, Toyoshima M, Tsujikura M, Saijo H and Shiojiri M 1992 *Ultramicroscopy* **41** 201
- Jefferson D A and Harris P J F 1988 *Nature* **332** 617
- Jia C J, Faley M I, Poppe U and Urban K 1995 *Appl. Phys. Lett.* **67** 3635
- Jia C J, Grove M, Dittmann R and Urban K 1996 *Phil. Mag. Lett.* **74** 25
- Jia C J, Soltner H, Jakob G, Hahn T, Adrian H and Urban K 1993 *Physica C* **210** 1
- Jia C J and Urban K 1993 *Interface Sci.* **1** 21
- Jouffrey B and Marlik M 1993 *Microsc. Microanal. Microstruct.* **3** 243
- Kang Z C and Eyring L 1987 *Ultramicroscopy* **23** 275
- Kang Z C, Smith D J and Eyring L 1986 *Surf. Sci.* **175** 684
- Kawashima T, Matsui Y and Takayama-Muromuchi E 1994 *Physica C* **224** 69
- Kienzle O and Ernst F 1997 *J. Am. Ceram. Soc.* **80** 1639
- Kilaas R and Gronsky R 1985 *Ultramicroscopy* **16** 193
- Kim M, Carpenter R W, Chen Y L and Schwuttke G H 1992 *Ultramicroscopy* **40** 258
- King W E and Campbell G H 1993 *Ultramicroscopy* **51** 128
- 1994 *Ultramicroscopy* **56** 46
- King W E and Lamver B S 1991 *Microbeam Analysis* ed D G Howitt (San Francisco: San Francisco Press) p 217
- Kirkland E J 1984 *Ultramicroscopy* **15** 151
- Kirkland A I, Rodenburg J, Saxton W O, Tsuno K and Kawasaki M 1993 *Inst. Phys. Conf. Ser.* **138** 247
- Kirkland A I, Saxton W O and Chand G 1997 *J. Electron Microsc.* **1** 11
- Kirkland A I, Saxton W O, Chau K-L, Tsuno K and Kawasaki M 1995 *Ultramicroscopy* **57** 355
- Kisielowski C, Schwander P, Baumann F H, Seibt M, Kim M and Ourmazd A 1995 *Ultramicroscopy* **58** 131
- Kizuka T, Iijima M and Tanaka N 1997 *Trans. JIM* **40** 135
- Kizuka T and Tanaka N 1994 *Phil. Mag. Lett.* **69** 135
- Knauss D and Mader W 1991 *Ultramicroscopy* **37** 247
- Komoda T 1966a *Japan. J. Appl. Phys.* **5** 603

- Komoda T 1966b *Hitachi Review* **15** 345
- Konnert J, D'Antonio P, Cowley J M, Higgs A and Ou H-J 1989 *Ultramicroscopy* **30** 371
- Koops H 1978 *Electron Microscopy* vol 3, ed J M Sturgess (Toronto: Microscopical Society of Canada) p 185
- Koster A J and de Jong A F 1991 *Ultramicroscopy* **38** 235
- Koster A J and de Ruijter W J 1992 *Ultramicroscopy* **40** 89
- Koster A J, de Ruijter W J, van der Bos A and van der Mast K-H 1989 *Ultramicroscopy* **29** 251
- Koster A J, van der Bos A and van der Mast K-H 1987 *Ultramicroscopy* **21** 209
- Krakow W 1990 *J. Mater. Res.* **5** 2658
- Krakow W, DiVicenzo D P, Bancel P A, Cockayne E and Elser V 1993 *J. Mater. Res.* **8** 24
- Krakow W, Ponce F A and Smith D J (eds) 1989 *High Resolution Microscopy of Materials (MRS Symp. Proc. 139)* (Pittsburgh, PA: Materials Research Society)
- Krakow W and Smith D A 1987 *Ultramicroscopy* **22** 47
- Krekels T, Milat O, van Tendeloo G, Amelinckx S, Babu T G N, Wright A J and Greaves C 1993 *J. Solid State Chem.* **105** 313
- Krivanek O L 1976 *Optik* **45** 97
- 1994 *Ultramicroscopy* **55** 419
- Krivanek O L and Fan G 1992 *Scanning Microscopy suppl. 6* ed P W Hawkes P W (Chicago, IL: Scanning Microscopy International) p 105
- Krivanek O L, Isoda S and Kobayashi K 1977 *Phil. Mag.* **36** 931
- Krivanek O L and Leber M L 1993 *Proc. 51st. Ann. Meet. Microscope Society of America* ed G W Bailey and C L Rieder (San Francisco: San Francisco Press) p 972
- Krivanek O L and Mooney P E 1993 *Ultramicroscopy* **49** 95
- Krivanek O L and Rez P 1980 *Proc. 38th. Ann. Meet. Electron Microscopy Society of America* ed G W Bailey (Baton Rouge, LA: Claitor's) p 170
- Krivanek O L and Stadelmann P A 1995 *Ultramicroscopy* **60** 103
- Kujawa S and Krahel D 1992 *Ultramicroscopy* **46** 395
- Kuo I A M and Glaeser R M 1975 *Ultramicroscopy* **1** 53
- Legoues F K, Krakow W and Ho P S 1986 *Phil. Mag. A* **53** 833
- Lentzen M and Urban K 1996 *Ultramicroscopy* **62** 89
- Le Poole 1947 *Philips Tech. Rev.* **2** 33
- Li C, Bando Y, Nakamura M and Kimizuka N 1997 *J. Electron Microsc.* **46** 119
- Lichte H 1991 *Adv. Opt. Electr. Microsc.* **12** 25
- 1992 *Ultramicroscopy* **47** 223
- 1993 *Ultramicroscopy* **51** 15
- Lichte H, Geiger D, Harscher A, Heindl E, Lehmann M, Malamidis D, Orchowski A and Rau W-D 1996 *Ultramicroscopy* **64** 67
- Lichte H, Kessler P, Lenz F and Rau W D 1993 *Ultramicroscopy* **52** 575
- Loane R F, Xu P and Silcox J 1992 *Ultramicroscopy* **40** 121
- Loubradou M, Bonnet R and Penisson J M 1995 *Phil. Mag. A* **72** 1381
- Loubradou M, Penisson J M and Bonnet R 1993 *Ultramicroscopy* **51** 270
- Lu P and Smith D J 1987 *Phys. Rev. Lett.* **59** 2177
- 1988 *Ultramicroscopy* **25** 265
- 1990 *Phil. Mag. B* **62** 435
- 1991 *Surf. Sci.* **254** 119
- Lundberg M L, Hutchison J L and Smith D J 1989 *J. Solid State Chem.* **80** 178
- Luzzi D E 1991 *Ultramicroscopy* **37** 180
- Luzzi D E, Yan M, Sob M and Vitek V 1991 *Phys. Rev. Lett.* **67** 1894
- Marks L D 1984 *Surf. Sci.* **139** 281
- 1996 *Ultramicroscopy* **62** 43
- Marks L D and Smith D J 1983 *Nature* **303** 316
- Matsui Y and Akimitsu J 1995 *Microsc. Res. Tech.* **30** 155
- Matsuta A, Tonomura A and Komoda T 1978 *Japan. J. Appl. Phys.* **17** 2073
- McCartney M R and Smith D J 1991 *Surf. Sci.* **250** 169
- McCartney M R, Youngman R A and Teller R G 1992 *Ultramicroscopy* **40** 291
- McGibbon M M, Browning N D, Chisholm M F, McGibbon A J, Pennycook S J, Ravikumar V and Dravid V P 1994 *Science* **266** 102
- McGibbon M M, Browning N D, McGibbon A J and Pennycook S J 1996 *Phil. Mag. A* **73** 625
- McGibbon A J and Pennycook S J 1995 *Inst. Phys. Conf. Ser.* **146** 79

- McKernan S, Norton M G and Carter C B 1992 *J. Mater. Res.* **7** 1052
- Medlin D L, Carter C B, Angelo J E and Mills M J 1997 *Phil. Mag.* A **75** 733
- Medlin D L, Mills M J, Stobbs W M, Daw M S and Cosandey F 1993 *Mater. Res. Soc. Symp. Proc.* **295** 91
- Menter J W 1956 *Proc. R. Soc. A* **236** 119
- Merkle K L and Smith D J 1987 *Phys. Rev. Lett.* **59** 2887
- Milat O, Van Tendeloo G and Amelinckx S 1992 *Ultramicroscopy* **41** 65
- Mills M J and Daw M S 1990 *Mater. Res. Soc. Symp. Proc.* **183** 15
- Mills, M J, Daw M S and Foiles S M 1994 *Ultramicroscopy* **56** 79
- Mills M J, Daw M S, Thomas G J and Cosandey F 1992 *Ultramicroscopy* **40** 247
- Mills M J and Miracle D B 1993 *Acta Metall. Mater.* **41** 85
- Mills M J and Stadelmann P 1989 *Phil. Mag.* A **60** 355
- Misell D L 1978 *Practical Methods in Electron Microscopy* vol 7, ed A M Glauert (Amsterdam: North-Holland) ch 3
- Mitome M and Takayanagi K 1991 *Ultramicroscopy* **39** 382
- Möbus G and Necker G 1997 *J. Microsc.* in press
- Möbus G, Necker G and Rühle M 1993 *Ultramicroscopy* **49** 46
- Möbus G and Rühle M 1994 *Ultramicroscopy* **56** 54
- Mori N, Oikawa T, Katoh T, Miyahara J and Harada Y 1988 *Ultramicroscopy* **25** 195
- Muller D A, Subraman S, Batson P E, Sass S L and Silcox J 1995 *Phys. Rev. Lett.* **75** 4744
- Munro E 1988 *J. Vac. Sci. Technol.* B **6** 941
- Murakoshi H, Ichihashi M and Kakibayashi H 1992 *Proc. 50th. Anniv. Meet. Electron Microscopy Society of America* ed G W Bailey, J Bentley and J A Small (San Francisco: San Francisco Press) p 936
- Nadarzinski K and Ernst F 1996 *Phil. Mag.* A **74** 641
- Nellist P D, McCallum B C and Rodenburg J M 1995 *Nature* **374** 630
- Nellist P D and Rodenburg J 1994 *Inst. Phys. Conf. Ser.* **138** 239
- Ning X G and Ye H Q 1990a *Phil. Mag.* A **62** 431
- 1990b *Phil. Mag. Lett.* A **61** 269
- Ohta J, Suzuki K and Suzuki T 1994 *J. Mater. Res.* **9** 2953
- O'Keefe M A 1984 *Electron-Optical Systems for Microscopy, Microanalysis and Microlithography* ed J J Hren, F A Lenz, E Munro and P Sewell (Chicago, IL: Scanning Microscopy International) p 209
- 1992 *Ultramicroscopy* **47** 282
- O'Keefe M A, Downing K H, Wenk H-R and Hu M 1994 *Mater. Res. Soc. Symp. Proc.* **332** 563
- Olsen A and Spoenche J C H 1981 *Phil. Mag.* A **43** 945
- Orchowski A, Rau W D and Lichte H 1995 *Phys. Rev. Lett.* **74** 399
- Otten M T and Coene W M J 1993 *Ultramicroscopy* **48** 77
- Ourmazd A, Baumann F H, Bode M and Kim Y 1990 *Ultramicroscopy* **34** 237
- Ourmazd A, Rentschler J R and Taylor D W 1986 *Phys. Rev. Lett.* **57** 3073
- Ourmazd A, Taylor D W, Bode and Kim Y 1989b *Science* **246** 1571
- Ourmazd A, Taylor D W, Cunningham J and Tu C W 1989a *Phys. Rev. Lett.* **62** 933
- Ourmazd A, Tsang W T, Rentschler J A and Taylor D W 1987 *Appl. Phys. Lett.* **50** 1417
- Overwijk M H F, Bleeker A J and Thust A 1997 *Ultramicroscopy* **67** 163
- Paciornik S, Kilaas R and Dahmen U 1993 *Ultramicroscopy* **50** 255
- Paciornik S, Kilaas R, Turner J and Dahmen U 1996 *Ultramicroscopy* **62** 15
- Penisson J M 1993 *Ultramicroscopy* **51** 264
- Penisson J M, Bacia M and Biscondi M 1994 *Electron Microscopy* vol 2A, ed B Jouffrey and C Colliex p 185
- Penisson J M, Baumann F H, Bode M and Ourmazd A 1991b *Phil. Mag. Lett.* **64** 239
- Penisson J M and Bourret A 1979 *Phil. Mag.* A **40** 811
- Penisson J M, Gronsky R and Brosse J 1982 *Scripta Met.* **16** 1239
- Penisson J M, Mills M J and Dahmen U 1991a *Phil. Mag. Lett.* **64** 327
- Penisson J M, Nowicki T and Biscondi M 1988 *Phil. Mag.* A **58** 947
- Pennycook S J 1992 *Ann. Rev. Mater. Sci.* **22** 171
- Pennycook S J, Browning N D, Jesson D E, Chisholm M F and McGibbon A J 1993 *Appl. Phys.* A **57** 385
- Pennycook S J and Jesson D E 1990 *Phys. Rev. Lett.* **64** 938
- Pennycook S J, Jesson D E, Chisholm M F, Browning N D, McGibbon A J and McGibbon M M 1995 *J. Microsc. Soc. Am.* **1** 231
- Petford-Long A K, Long N J, Smith D J, Wallenberg L R and Bovin J-O 1987 *Physics and Chemistry of Small Clusters* ed P Jena, B K Rao and S N Khanna (New York: Plenum) p 127
- Phillipp F 1996 *Adv. Solid State Physics* **35** 257

- Phillipp F, Höschen R, Osaki, Möbus G and Rühle M 1994 *Ultramicroscopy* **56** 1
- Ponce F A and Hikashi H 1992 *Scanning Microscopy suppl.* 6 ed P W Hawkes (Chicago, IL: Scanning Microscopy International) p 339
- Portier X, Rizk R, Nouet G and Allais G 1995 *Phil. Mag. A* **71** 1109
- Ramesh R, Inam A, Huang D M, Ravi T S, Sands T, Xi X X, Wu X D, Li Q, Venkatesan T and Kilaas R 1991 *J. Mater. Res.* **6** 2264
- Ravikumar V and Dravid V P 1993 *Ultramicroscopy* **52** 557
- Recnik A, Bruley J, Mader W, Kolar D and Rühle M 1994 *Phil. Mag. B* **70** 1021
- Rodenburg J M, McCallum B C and Nellist P D 1993 *Ultramicroscopy* **48** 304
- Rose H 1990 *Optik* **85** 95
- 1994 *Ultramicroscopy* **56** 11
- Rosenauer A, Kaiser S, Reisinger T, Zweck J, Gebhardt W and Gerthsen D 1996 *Optik* **102** 63
- Rühle M, Phillipp F, Seeger A and Heydenreich J (eds) 1994 High-voltage and high-resolution electron microscopy *Ultramicroscopy* **56** 1–3
- Ruska E 1934 *Zeit. f. Physik* **85** 580
- 1980 *The Early Development of Electron Lenses and Electron Microscopy* trans. Mulvey T Engl. Transl. (Stuttgart: Hirzel)
- Sarikaya M 1992 *Ultramicroscopy* **47** 1
- Sarikaya M, Wickramasinghe H K and Isaacson M (ed) 1995 *Determining Nanoscale Physical Properties of Materials by Microscopy and Spectroscopy*, (MRS Symp. Proc. 332) (Pittsburgh, PA: Materials Research Society)
- Saxton W O 1977 *Optik* **49** 51
- 1978 *Computer Techniques for Image Processing in Electron Microscopy* (New York: Academic)
- 1988 *Image and Signal Processing in Electron Microscopy*, *Scanning Microscopy suppl.* 2 ed P W Hawkes, F P Ottensmeyer, W O Saxton and A Rosenfeld A (Chicago, IL: Scanning Microscopy International) p 213
- 1994 *J. Microsc.*
- 1995a *Ultramicroscopy* **58** 239
- 1995b *Ultramicroscopy* **55** 171
- Saxton W O, Pitt T J and Horner M 1979 *Ultramicroscopy* **4** 343
- Saxton W O and Smith D J 1985 *Ultramicroscopy* **18** 39
- Saxton W O, Smith D J and Erasmus S J 1983 *J. Microsc.* **130** 187
- Sayre D 1952 *Acta Crystallogr.* **5** 60
- Scherzer O 1936 *Zeit. f. Physik* **101** 593
- 1947 *Optik* **2** 114
- 1949 *J. Appl. Phys.* **20** 20
- Schiske P 1968 *Electron Microsc.* 145
- 1973 *Image Processing and Computer-Aided Design in Electron Optics* ed P W Hawkes (London: Academic) p 32
- Schmidt C, Ernst F, Finnis M W and Vitek V 1995 *Phys. Rev. Lett.* **75** 2160
- Schwander P, Kisielowski C, Seibt M, Baumann F H, Kim Y and Ourmazd A 1993 *Phys. Rev. Lett.* **71** 4150
- Self P G and O'Keefe M A 1988 *High Resolution Transmission Electron Microscopy and Associated Techniques* ed P R Buseck, J M Cowley and L Eyring (Oxford, New York: Oxford University Press) ch 8
- Self P G, O'Keefe M A, Buseck P R and Spargo A E 1983 *Ultramicroscopy* **11** 35
- Shamsuzzoha M, Smith D J and Deymier P 1990 *Scripta Met. Mater.* **24** 1611
- 1991 *Phil. Mag. A* **64** 719
- Sharma R, Gai P L, Gajdardziska -Josifovska M, Sinclair R and Whitman L J (eds) 1996 *In Situ Electron and Tunneling Microscopy of Dynamic Processes*, (MRS Symp. Proc. 404) (Pittsburgh, PA: Materials Research Society)
- Shaw T M, Gupta A, Chern M Y, Batson P E, Leibowitz R B and Scott B A 1994 *J. Mater. Res.* **9** 2566
- Shiojiri M, Nakamura N, Kaito C and Miyano T 1983 *Surf. Sci.* **126** 719
- Sinclair R, Ponce F A, Yamashita T, Smith D J, Camps R A, Freeman L A, Erasmus S J, Nixon W C, Smith K C A and Catto C J D 1982 *Nature* **298** 127
- Sinclair R, Smith D J and Dahmen U (eds) 1990 *High Resolution Electron Microscopy of Defects in Materials*, (MRS Symp. Proc. 183) (Pittsburgh, PA: Materials Research Society)
- Sinclair R, Yamashita T, Parker M A, Kim K B, Holloway K and Schwartzmann A F 1988 *Acta Crystallogr. A* **44** 965
- Sinclair R, Yamashita T and Ponce F A 1981 *Nature* **290** 386
- Smith A R and Eyring L 1982 *Ultramicroscopy* **8** 65

- Smith D J 1985 *J. Vac. Sci. Technol. B* **3** 1563
—1986 *Chemistry and Physics of Solid Surfaces VI* ed R Vanselow and R Howe (Berlin: Springer) ch 15
—1989a *J. Electron Microsc. Tech.* **12** 11
—1989b *Adv. Opt. Electron Microsc.* **11** 1
Smith D J, Barry J C, Petford A K and Wheatley J C 1985a *JEOL News E* **22** 2
Smith D J, Bursill L A and Jefferson D A 1986a *Surf. Sci.* **175** 673
Smith D J, Bursill L A and McCartney M R 1987a *Ultramicroscopy* **23** 299
Smith D J, Bursill L A and Wood G J 1983a *J. Solid State Chem.* **50** 51
Smith D J, Camps R A, Cosslett V E, Freeman L A, Saxton W O, Nixon W C, Catto C J D, Cleaver J R A, Smith K C A and Timbs A E 1982 *Ultramicroscopy* **9** 203
Smith D J, Camps R A, Freeman L A, O'Keefe M A, Saxton W O and Wood G J 1985b *Ultramicroscopy* **18** 63
Smith D J, de Ruijter W J, McCartney M R and Weiss J K 1993 *Ultramicroscopy* **52** 591
Smith D J, Glaisher R W and Lu P 1989a *Phil. Mag. Lett.* **59** 69
Smith D J, Glaisher R W, Lu P and McCartney M R 1989b *Ultramicroscopy* **29** 123
Smith D J, Higgs A and Perkes P R 1987b *Proc. 45th. Ann. Meet. Electron Microscopy Society of America* ed G W Bailey (San Francisco: San Francisco Press) p 62
Smith D J and Lu P 1991 *Inst. Phys. Conf. Ser.* **117** 1
Smith D J and Marks L D 1985 *Ultramicroscopy* **16** 101
Smith D J and O'Keefe M A 1983 *Acta Crystallogr. A* **39** 838
Smith D J, Petford-Long A K, Wallenberg L R and Bovin J-O 1986b *Science* **233** 872
Smith D J, Saxton W O, O'Keefe M A, Wood G J and Stobbs W M 1983b *Ultramicroscopy* **11** 263
Smith D J and Spence J C H (eds) 1993 Aspects of electron microscopy, diffraction, crystallography and spectroscopy *Ultramicroscopy* **52** 3–4
Spargo A E C, Beeching M J and Allen L J 1994 *Ultramicroscopy* **55** 329
Spence J C H 1988 *Experimental High Resolution Electron Microscopy* (Oxford: Clarendon)
—1997 *Acta Crystallogr. A* in press
Spence J C H and Zuo J M 1988 *Rev. Sci. Instrum.* **59** 2102
Stadelmann P A 1987 *Ultramicroscopy* **21** 13
Stemmer S, Streiffer S K, Ernst F and Rühle M 1995 *Phil. Mag. A* **71** 713
Stenkamp D and Jäger W 1993 *Ultramicroscopy* **50** 269
Stobbs W M and Saxton W O 1988 *J. Microsc.* **151** 88
Takeda M and Hashimoto H 1985 *Phys. Status Solidi a* **87** 141
Takeda M, Yoshida H, Endoh H and Hashimoto H 1988 *J. Microsc.* **151** 147
Takeda M, Yoshida H and Hashimoto H 1985 *Phys. Status Solidi a* **87** 473
Tanaka M, Ichinose H, Furuta T, Ishida Y and Sakaki H 1987 *J. Physique Coll.* **5** 101
Tanaka N, Kimata H and Kizuka T 1996 *J. Electron Microsc.* **45** 113
Terasaki O, Smith D J and Wood G J 1986 *Acta Crystallogr. B* **42** 39
Thoma S and Cerva H 1994 *Ultramicroscopy* **53** 37
Thust A, Lentzen M and Urban K 1994 *Ultramicroscopy* **53** 101
Thust A, Overwijk M H F, Coene W M J and Lentzen M 1996 *Ultramicroscopy* **64** 249
Thust A and Urban K 1992 *Ultramicroscopy* **45** 23
Tonomura A 1993 *Electron Holography* (Heidelberg: Springer)
Treacy M M J and Gibson J M 1993 *Ultramicroscopy* **52** 31
Tricker D M and Stobbs W M 1995 *Phil. Mag. A* **71** 1037
Valle R, Genty B, Marraud A and Pardo B 1977 *Proc. 5th. Int. Conf. HVEM*, ed T Imura and H Hashimoto (Kyoto, Japan Society for Electron Microscopy) p 163
van Dyck D 1980 *J. Microsc.* **119** 141
van Dyck D and de Jong A F 1992 *Ultramicroscopy* **47** 266
van Dyck D, Lichte H and vander Mast K D 1997 *Ultramicroscopy* **64** 1
van Dyck D, Op de Beeck M and Coene W 1993 *Optik* **93** 103
Vila A, Cornet A, Morante J R, Ruterana J R, Loubradou M, Bonnet R, Gonzalez Y and Gonzalez L 1995 *Phil. Mag. A* **71** 85
Vitek V and Srolowitz D J (eds) 1989 *Atomistic Simulation of Materials* (New York: Plenum)
von Harrach H S 1995 *Ultramicroscopy* **58** 1
Wall J S, Hainfield J F and Bitter J W 1977 *Ultramicroscopy* **3** 81
Wallenberg L R, Bovin, J-O, Petford-Long A K and Smith D J 1986 *Ultramicroscopy* **20** 71
Wallenberg R, Bovin J-O and Smith D J 1985 *Naturwiss.* **72** 539
Walther T and Gerthsen D 1993 *Appl. Phys. A* **57** 393

- Walther T, Hetherington C J D and Humphreys C J 1995 *Inst. Phys. Conf. Ser.* **146** 53
- Wang Z L and Zhang J 1995 *Phil. Mag. A* **72** 1513
- Watanabe D and Terasaki O 1984 *Mater. Res. Soc. Symp. Proc.* **21** 231
- Weirich T E, Ramlau R, Simon A, Hovmöller S and Zou X 1996 *Nature* **382** 144
- Werner P, Jäger W and Schüppen A 1993 *J. Appl. Phys.* **74** 3846
- Wilson A R, Spargo A E and Smith D J 1982 *Optik* **61** 63
- Wood G J, Bursill L A and Smith D J 1983 *J. Microsc.* **129** 263
- Yagi K 1987 *J. Appl. Crystallogr.* **20** 147
- Yagi K, Takayanagi K, Kobayashi K and Nagakura S 1983 *Proc. 7th Int. Conf. on High Voltage Electron Microscopy* ed R M Fisher, R Gronsky and K H Westmacott (Berkeley, CA: Lawrence Berkeley Laboratory) p 11
- Zandbergen H, Andersen S and Jansen J 1997 *Science* **277** 1221
- Zandbergen H W and Van Tendeloo G 1990 *Mater. Res. Soc. Symp. Proc.* **183** 337
- Zeitler E 1992 *Ultramicroscopy* **46** 405
- Zemlin F, Weiss K, Schiske P, Kunath W and Herrmann K-H 1978 *Ultramicroscopy* **3** 49
- Zhang H, Marks L D, Wang Y Y, Zhang H, Dravid V P, Han P and Payne D A 1995 *Ultramicroscopy* **57** 103
- Zheng J G, Liu Z G, Li Q, Zhu J M, Feng D and Frommeyer G 1994 *Phil. Mag. A* **70** 917
- Zou X, Sundberg M, Larine M and Hovmöller S 1996 *Ultramicroscopy* **62** 103
- Zuo J-M, McCartney M R and Spence J C H 1996 *Ultramicroscopy* **66** 35